©Copyright 2019

Seong Beom Lee

Integrating Energy Storage Systems into Renewable Grid Applications: A Model-based Approach

Seong Beom Lee

A dissertation

submitted in partial fulfillment of the

requirements for the degree of

Doctor of Philosophy

University of Washington

2019

Reading Committee:

Venkat R. Subramanian, Chair

Daniel T. Schwartz

Elizabeth Nance

Baosen Zhang

David Gao

Program Authorized to Offer Degree:

Chemical Engineering

University of Washington

Abstract

Integrating Energy Storage Systems into Renewable Grid Applications: A Model-based Approach

Seong Beom Lee

Chair of the Supervisory Committee:
Professor Venkat R. Subramanian
Department of Chemical Engineering

Accurate and economical sizing of stand-alone power system components, including batteries, has been an active area of research in renewable grid applications, but current approaches to integrating batteries into the entire renewable grid components do not make them economically feasible. Typically, batteries are treated as a black box that does not account for their internal states in current renewable grid simulations. This might lead to under-utilization and over-stacking of batteries. In contrast, detailed physics-based battery models, accounting for internal states, can save a significant amount of energy and cost, utilizing batteries with maximized life and usability. Therefore, it is important to identify how efficient physics-based models of batteries can be included and addressed in grid control strategies.

In this dissertation, an efficient battery/grid integration framework will be studied and analyzed. Simple examples for microgrids and the direct simulation of the same including physics-based battery models will be presented. A representative microgrid example, which integrates stand-alone PV arrays, a maximum power point tracking controller, lithium-ion batteries, and power electronics, is illustrated. The results of the proposed approach are

compared with the conventional approaches and improvements in performance and speed are reported. Also, Vanadium redox flow batteries are promising energy storage systems for renewable grid applications. Open source codes, batch-cell models, and experimental data are provided to enable people’s access to robust and accurate models and optimizers for an efficient battery/grid integration framework.

TABLE OF CONTENTS

List of Figures iii

List of Tables vii

Chapter 1. Introduction 1

Chapter 2. Direct, efficient, and Real-time simulations of Physics-based battery Models for PV-Battery Microgrid structure 4

- 2.1 Significant and impact 5
- 2.2 Modeling and simulation of PV arrays & MPPT controller 7
  - 2.2.1 Mathematical modeling for PV arrays 7
  - 2.2.2 P&O MPPT algorithm 10
  - 2.2.3 DAE-based MPPT algorithm 11
  - 2.2.4 Results 13
- 2.3 Modeling of PV arrays with MPPT controller & power electronics components 14
  - 2.3.1 Power electronics components 15
  - 2.3.2 Results 16
- 2.4 Modeling of PV arrays with MPPT controller, battery & power electronics components 18
  - 2.4.1 Conventional and proposed control algorithm 19
  - 2.4.2 Reformulated P2D battery model 20
  - 2.4.3 Simulation of Battery operation 26
  - 2.4.4 Results 28
- 2.5 Practical impact and implementation into a microcontroller 30
- 2.6 Perspectives 31

Chapter 3. Vanadium redox batch cell systems 32

- 3.1 Significant and impact 33
- 3.2 Experimental 39
  - 3.2.1 Materials 39
  - 3.2.2 Instrument 39
  - 3.2.3 The batch cell system 40
  - 3.2.4 Preparation of electrolytes 40
  - 3.2.5 Cell operation 41
- 3.3 Model formulation 42
  - 3.3.1 Model 1: Diffusion model 45
  - 3.3.2 Model 2: Diffusion model + Uni-directional migration and convection 54
  - 3.3.3 Model 3: Diffusion model + Full directional migration and convection 57
  - 3.3.4 Model 4: Diffusion model + Full directional ion flux+ Proton transport 61

3.4 Model validation with different membranes 69
  3.4.1 Assumption and equations 69
  3.4.2 Parameter estimation 70
3.5 Uniqueness issue with a system approach 73
  3.5.1 Different C-rates 75
  3.5.2 Confidence interval 75
3.6 Open source platform 76
  3.6.1 Target users 77
  3.6.2 Solver and optimization 78
  3.6.3 Converged parameters 78

Chapter 4. Direct numerical method of lines techniques for potential and current distributions: primary and secondatry approximations 79

4.1 Background 80
4.2 Method 83
  4.2.1 Rectangular cell 85
  4.2.2 Hull cell 96
  4.2.3 Thin-layer galvanic cell 107

Chapter 5. Future work 114

5.1 Flow battery 114
  5.1.1 Single-cell and multiple-cell models 114
5.2 Battery/grid integration 115

Bibliography 116

Appendix A 123

LIST OF FIGURES

Figure 1.1. Model-based integration for renewable grid applications. 2

Figure 2.1. Single-diode equivalent circuit-based model of a practical PV cell and MPPT controller 8

Figure 2.2. The flow chart of P&O MPPT algorithm. 10

Figure 2.3. The flow chart of DAE-based MPPT algorithm. 12

Figure 2.4. Simple case study with different irradiance values. (a) Solar irradiance at 800, 400, 1000, 50, 600, and 200 W/m2 for 10 seconds, respectively. (b) Solar power outputs over voltage from the single-diode equivalent circuit-based model. (c) Voltage outputs (d) Current outputs, from DAE-based (wine color and empty circle) and P&O (dark green color and filled square) MPPT algorithms. 14

Figure 2.5. System configuration of a stand-alone PV microgrids, consisting of PV systems, a bidirectional DC/DC converter, a bidirectional DC/AC inverter. 15

Figure 3.1. Schematic of a vanadium redox flow battery showing membrane, electrolytes, electrodes, and reservoirs. 32

Figure 3.2. Schematic of the laboratory-scale VRBC system. (a) An actual image of the system for a discharge state. The blue electrolyte represents VO^{2+} (positive) and the green electroltye represents V^{3+} (negative). (b) Specification of the system.. 36

Figure 3.3. Parameter estimation of the batch cell system with charging/ discharging curves at different C-rates. 37

Figure 3.4. Open source platfrom and user benefit. 38

Figure 3.5. Side reactions caused by crossover of vanadium ions through the membrane durging charging. 44

Figure 3.6. Crossover of vanadium ions through the membrane in the uni-direction model during (a) charging and (b) discharging. PE and NE represent positive and negative electrodes, respectively. A blue-colored dotted arrow indicates VO^{2+}/VO_2^+ diffusion (see the first arrow from the top in (a) Charge and (b) Discharge), a wine-colored dotted arrow represents VO^{2+}/VO_2^+ migration and electro-osmotic convection (see the second arrow from the top in

(a) Charging), a sky-blue colored solid arrow shows V^{2+} / V^{3+} diffusion (see the third arrow from the top in (a) Charging and the second arrow from the top in (b) Discharging), and a red-colored solid arrow represents V^{2+}/V^{3+} migration and electro-osmotic convection (see the third arrow from the top in (b) Discharging)... 53

Figure 3.7. Crossover of vanadium ions through the membrane by diffusion, migration, and electro-osmotic convection during (a) charging and (b) discharging. A blue-colored dotted arrow indicates VO^{2+}/VO_2^+ diffusion (see the first arrow from the top in (a) Charge and (b) Discharge), a wine-colored dotted arrow represents VO^{2+}/VO_2^+ migration and electro-osmotic convection (see the second arrow from the top in (a) Charging and (b) Discharging), a sky-blue colored solid arrow shows V^{2+} / V^{3+} diffusion (see the third arrow from the top in (a) Charging and (b) Discharging), and a red-colored solid arrow represents V^{2+}/V^{3+} migration and electro-osmotic convection (see the fourth arrow from the top in (a) Charging and (b) Discharging).. 58

Figure 3.8. Model formulation process and comparison of voltage profiles between different model outputs and experimental data from the batch cell system including the Nafion® 115 membrane. Voltage profiles at C/30 (Experimental data: charge (wine color and filled square dots), discharge (wine color and filled circle), the model (blue-color straight line). (a) Diffusion model (b) Uni-direction model (c) Full-direction model. 60

Figure 3.9. Comparison of voltage and predicted concentration profiles between the full-direction model including the proton transport and the simple model for the batch cell system equipped with the Nafion® 115 membrane at C/30. (Experimental data: charge (wine color and filled square dots), discharge (wine color and filled circle), the full-direction model: blue-color straight line, and the simple model: green-color straight line). (a) Full-direction model including the proton transport vs. experimental data, (b) Simple model vs. experimental data, (c) V^{2+} (purple color) and V^{3+} (green color) concentration profiles from the VRBC model at C/30, (d) V^{2+} (light purple color) and V^{3+} (light green color) concentration profiles from the simple model at C/30, (e) VO^{2+} (blue color) and VO_2^+ (orange color) concentration profiles from the VRBC model at C/30, and (f) VO^{2+} (light blue color) and VO_2^+ (light orange color) concentration profiles from the simple model at C/30. 67

Figure 3.10. Comparison of voltage profiles between model outputs and experimental data, and predicted vanadium ion concentrations vs. capacity, for the batch cell system including the Nafion® XL membrane at the first cycle. The batch cell system is charged first and then discharged. (a) Voltage profiles from experiment data (charge: wine color and filled square, discharge: wine color and filled circle) and model outputs (blue-color straight line) at C/30 (b) V^{2+} (purple color) and V^{3+} (green color) concentration profiles at C/30. (c) VO^{2+} (blue color) and VO_2^+ (orange color) concentration profiles at C/30. 72

Figure 3.11. Comparison of voltage profiles between model outputs and experimental data from the batch cell system at C/20. Voltage profiles of (a) the Nafion® 115 system and (b) the Nafion® XL system (Experimental data: wine color and filled square dots, VRBC model outputs: blue color and straight plot). 74

Figure 4.1. Fast and accurate approach to identifying current and potential distributions of electrochemical cell systems. 83

Figure 4.2. The rectangular cell system. 85

Figure 4.3. The comparison of the 1-D coordinate between finite difference and finite volume methods. 91

Figure 4.4. The comparison of potential and current distributions between the Finite Volume Method (FDM), the Finite Volume Method (FVM), and the Finite Element Method (FEM) obtained by COMSOL in the rectangular system. (a) Potential distribution of primary, secondary linear, and secondary non-linear approximations along y-axis (height) of the cell system and Potential and current distributions with (b) primary current approximations (c) secondary linear approximations, and (d) non-linear current approximations. 94

Figure 4.5.The original Hull cell system 96

Figure 4.6. The reformulated Hull cell system. 99

Figure 4.7. Comparison of potential distribution with constant nodes. When x=0.05, x=0.5, and x=0.95, (a) Primary current distribution (c) Secondary linear current distribution (e) Secondary non-linear current distribution along with y-axis. When y=0.5, (b) Primary current distribution (d) Secondary linear current distribution, and (d) Secondary non-linear current distribution. 101

Figure 4.8. Comparison of potential distribution with constant nodes with quadratic profiles. When x=0.05, x=0.5, and x=0.95, (a) Primary current distribution (c) Secondary linear current distribution (e) Secondary non-linear current distribution along with y-axis. When y=0.5, (b) Primary current distribution (d) Secondary linear current distribution, and (d) Secondary non-linear current distribution. 105
Figure 4.9. The original coplanar thin-layer galvanic cell system................................ 108
Figure 4.10. The reformulated coplanar thin-layer galvanic cell system...................... 108

LIST OF TABLES

Table 1.1. Comparison of battery performance between different chemistries and types .. 3

Table 2.1. Equations for PV systems 9

Table 2.2. Variables for PV systems 9

Table 2.3. Parameters for PV systems 9

Table 2.4. Calibration of P&O algorithm by adjusting voltage and time step 18

Table 2.5. Governing equations for Li-ion P2D model 22

Table 2.6. Additional equations for Li-ion P2D model 23

Table 2.7. List of variables for Li-ion P2D model 24

Table 2.8. Parameters for Li-ion P2D model 25

Table 3.1. Selected physics-based electrochemical engineering models of Vanadium redox flow batteries 35

Table 3.2. Governing equations (charging process) 47

Table 3.3. Governing equations (discharging process) 48

Table 3.4. Other equations of all-Vanadium redox batch batteries 49

Table 3.5. Variables of all-Vanadium redox batch cell systems 50

Table 3.6. Parameters of all-Vanadium redox batch cell system used in Simulations 51

Table 3.7. Governing equations for proton transport 65

Table 3.8. Estimated parameters of all-Vanadium redox batch cell systems (full-direction model) 66

Table 3.9. Sensitivity Analysis for Initial Guesses 68

Table 4.1. Various types/geometries of electrochemical cells 81

Table 4.2. Comparison of computational time in rectangular cell 95

Table 4.3. Comparison of computational time in the Hull cell with constant node and constant node with quadratic profiles 106

Table 4.4. Comparison of Computational Time in Coplanar thin-layer galvanic cell with constant node and variable node spacing 113

ACKNOWLEDGEMENTS

I give my most sincere acknowledgment to My Ph.D. advisor Professor Venkat R. Subramanian. His utmost guidance and support helped me think creatively and expand my research scopes. Also, I have learned his way of managing the research group. Professor Venkat R. Subramanian is an extraordinary role model for my future career development.

I would like to thank Professor Kyung Byung Yoon. Professor Kyung Byung Yoon is an extraordinary role model for my future career development as well. I was fortunate to have Professor Kyung Byung Yoon as my masters' advisor. I would like to express my best wishes to him.

I would like to express my appreciation and gratitude to Professor Dan T. Schwartz. During my Ph.D., I was lucky to see your big picture of clean energies, and why the US is the first leading country in the world.

I would like to express my appreciation and gratitude to Professor Elizabeth Nance. This quarter (Spring 2019), I took her class regarding communication and writing skills. I sincerely appreciate your advice and support.

I would like to express my appreciation and gratitude to Professor Baosen Zang. He has been supported me from my qualifying exam with helpful advice. His advice in a different viewpoint has been really helpful to my research.

I would like to express my appreciation and gratitude to Professor David Gao. He helped me a lot with my research topics and documentation work for academic positions.

I would like to thank Doctor Babu Chalamala, Professor Jim Pfaentner, Professor François Baneyx, and Professor Victor Zavala. Doctor Babu Chalamala has supported redox flow battery work, and Professor Jim Pfaentner has given good advice to me. Professor Francois helped me publish a paper in the biotechnology field. Professor Victor Zavala helped me publish a paper in the electricity market field

I would like to thank Professor Kishalay Mitra, Professor Venkat Ramadesigan, and Professor Dayaram Sonawane for their advice and support for my research.

Also, thanks to all MAPLE group members (past and current members). I was happy to work with you guys: Manan, Yanbo, Neal, Caitlin, Akshay, Linnette, Taejin, Surya, Maitri, Chintan, Thiagu, Mayandi, Jerry, Mengdi, Matt, Bharat, and Derek.

Last, my family, Myungsook Moon, Dongwoo Lee, Bokyoung Kim, and Emma Lee. I would like to express my appreciation for their unwavering support. Without my parents' support, I cannot accomplish my achievement. Time is flying. When I first came to the US, Emma was not in the world but now she is a five-year-old kid. I appreciate Bokyoung Kim for her support.

DEDICATION

to Bokyoung Kim, Myungsook Moon, Dongwoo Lee, and adorable Emma R. Lee

Chapter 1. INTRODUCTION

In this dissertation, the overarching objective is to provide an optimal battery/grid integration framework for physics-based battery models. This framework can have a significant impact on the grid society since it can be extended to many applications, including optimal sizing of energy storage, model predictive control, and cost analysis (*see Figure 1.1*).

The optimal framework will maximize the utilization of the entire renewable grid for each application. There are two key benefits of adopting physics-based models: i) minimizing over-stacking and under-utilization of individual systems by predicting the cell performance accurately and ii) maximizing the system life by controlling the internal state of individual components. For example, the total cost of the current grid system and the battery is \$583-1166/kWh and \$350-700/kWh (60% of the entire grid system), respectively. If the battery size can be reduced by 20% by implementing physics-based models, the total cost of the entire grid system and battery will be decreased by \$513-1026/kWh and \$280-560/kWh, respectively. Physics-based models can also be utilized to control the internal state of the battery to extend its life. Because grid applications typically range in size from kilowatts to megawatts, the optimal integration of individual systems can help save a tremendous amount of energy and cost for grid applications. Components of renewable grids, which account for a significant portion (>60%) of Capital Expenditure (CapEx) in the entire system, are battery systems.

Several physics-based models for the same that can maximize usability and performance of the individual electrochemical components have been developed. However, when modeling and simulation are extended to the entire grid simulation, a discrepancy arises between the developed physics-based models and the models implemented in the grid system.

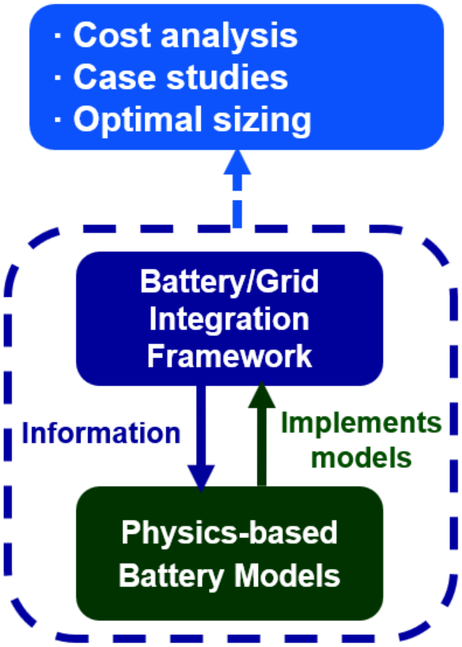

Figure 1.1. Model-based integration for renewable grid applications. One of the best possible ways of an efficient integration between Energy Storage Systems and other grid components might be to address integration and model development at the same time. The optimal integration can be achieved through a deep understanding of physics-based models.

The conventional approach to operating the renewable grid does not include the physics-based models but rather adopt empirical/electrical equivalent circuit-based models that do not account for internal states of the system with lower accuracy. This leads to underutilization of the entire renewable grid systems. There exists a delay between the development of the physics-based models and the integration of the models into the renewable grid system. For example, detailed physics-based models of lithium-ion batteries were developed in the late 1990s [1]. However, to date, most battery models used in renewable grid. simulations and controls in both industry and academia are based on empirical/electrical equivalent circuit-based models. Acceleration of the development of the models and the integration of the same into the renewable grid system can play a major role in the spread of renewable grids, minimizing overall CapEx of the entire system. To successfully achieve aforementioned research tasks, two different scale approaches will be attempted simultaneously: (a) Model development/formulation for battery systems (e.g., vanadium redox flow batteries) and (b) Integration framework with models for other devices.

Table 1.1. Comparison of battery performance between different chemistries and types

Battery	Cathode	Anode	Specific Energy (Wh/kg)	Average voltage (V)	Cycle life	Comments
Li-ion Batteries	LCO	Graphite	150-250	3.8	500-1000	High specific energy, but limited power and short life
	LFP	Graphite	90-120	3.4	1000-2000	Flat discharge curve, but low specific energy
	NMC	Graphite	150-220	3.7	1000-2000	High capacity and high power, but relatively low specific energy compared to LCO
VRFBs	Graphite	Graphite	10-20	1.15-1.55	>10000	Long life, but lower power and energy

Optimal integration requires a deeper understanding of individual electrochemical systems, and this is one of the reasons why two different scale approaches will be attempted at the same time. For example, renewable grid systems require energy storage/generation systems’ outputs above a certain voltage [2]. However, because the physics-based battery model was developed at the level of a single cell, multiple-cell models in a parallel and series combination are necessary to meet the required voltage in renewable grid systems. In this case, one might visualize a situation in which Li-ion batteries with different chemistries being used simultaneously, or flow batteries in combination with Li-ion batteries (*see Table 1.1*) [3]. Physics-based models will be helpful in particular when you transition from small coin cells to large format cell configurations. For example, if one cell becomes bad, the entire battery pack may not work properly. All cells in the entire pack will be completely out of balance at different charge/discharge rates, resulting in a pack that is virtually useless to the end user due to the failure of just one cell.

Empirical models are not capable of capturing the different performances of the different chemistries or types of batteries [2]. For this reason, current batteries are being conservatively operated to avoid this unwanted situation. Different chemistries/types of batteries have different benefits. It requires combinations of different chemistries and types of batteries to enhance their different advantages. The physics-based models will include many physical phenomena such as ions diffusion, migration, and convection, kinetics, and side reactions. For the validation, a laboratory-scale single cells will be used initially. This can be extended to a large stack in parallel and series. In this dissertation, therefore, an efficient battery/grid integration framework including physics-based lithium-ion battery models and model formulation and parameter estimation strategies for vanadium redox batch cell systems will be studied and discussed.

Chapter 2. DIRECT, EFFICIENT, AND REAL-TIME SIMULATIONS OF PHYSICS-BASED BATTERY MODELS FOR PV-BATTERY MICROGRID STRUCTURE

With renewable energy based electrical systems becoming more prevalent in homes across the globe, microgrids are becoming widespread and could pave the way for future energy distribution. Accurate and economical sizing of stand-alone power system components, including batteries, has been an active area of research, but current control methods do not make them economically feasible. Typically, batteries are treated as a black box that does not account for their internal states in current microgrid simulation and control algorithms. This might lead to under-utilization and over-stacking of batteries. In contrast, detailed physics-based battery models, accounting for internal states, can save a significant amount of energy and cost, utilizing batteries with maximized life and usability. It is important to identify how efficient physics-based models of batteries can be included and addressed in current grid control strategies. In this paper, we present simple examples for microgrids and the direct simulation of the same including physics-based battery models. A representative microgrid example, which integrates stand-alone PV arrays, a Maximum Power Point Tracking (MPPT) controller, batteries, and power electronics, is illustrated. Implementation of the MPPT controller algorithm and physics-based battery model along with other microgrid components as differential algebraic equations is presented. The results of the proposed approach are compared with the conventional control strategies and improvements in performance and speed are reported.

2.1 SIGNIFICANT AND IMPACT

Batteries have been integrated in microgrids to mitigate intermittent characteristics of alternative energy sources such as solar, wind, and wave, thereby enhancing grid operation and reliability [4, 5]. They are well suited for microgrid applications due to their versatility, high energy density, and efficiency [6]. The cost of batteries continues to decrease while their performance and life have continued to increase [7]. However, lithium-ion batteries, which are the most widely used energy storage systems implemented in microgrids today, are still the most expensive component, accounting for about 60% of the overall Capital Expenditure (CapEx) [8]. Conservative operations in current microgrids cause high cost and low energy efficiency, underutilizing and overstacking batteries. The current microgrid controls cannot utilize batteries aggressively to achieve high penetration of renewables and maximize life and usability of batteries in the meantime. They implement empirical/equivalent-circuit battery models, treating batteries as just a black box, which does not account for its internal states, and place batteries in a small portion of the entire microgrid, which means current microgrids do not consider batteries principal components [2, 9-12]. For example, if the internal temperature of the battery is not modeled, then the battery must be operated at very low rates to ensure that the internal temperature does not reach high enough values that reduce battery life and create unsafe operating conditions. Control systems based on measured external temperatures and empirical/equivalent-circuit models must be operating conservatively to avoid potential hot spots in the internal temperature [2]. It is evident that a tremendous amount of energy will be lost when batteries are conservatively operated. In contrast, detailed physics-based battery models, accounting for internal states, can help save an enormous amount of energy, utilizing batteries with maximized life and usability. In typical microgrid controls, however, the computation time will significantly increase when more detailed physics-based battery models are coupled to the entire microgrid system.

There is significant literature in simulation and control of grid and renewable grid components. This has been typically a field of electrical engineering. For example, the method used to integrate the models across different devices in the microgrid typically depends on (1) the choice/convenience of users and (2) linear models and linear control schemes, which have been used for robustness, ease of use for the researchers, and scalability to a large number of devices and systems. Unfortunately, battery models are highly nonlinear in nature, and linearization compromises the accuracy, leading to a narrower range of use for applications [13]. In this paper, we show that perhaps a better way to integrate battery models is to write the microgrid equations in mathematical form and then identify an efficient way to solve those models simultaneously with battery models. In this paper, we first show that direct Differential Algebraic Equation (DAE) implementation and simulation of microgrids gives better results regarding accuracy, simplicity, and speed, as illustrated for a simple microgrid. Next, we present how efficient the direct DAE implementation of a stand-alone PV microgrid system is, under dynamic irradiance (PV:

Photovoltaic). Finally, we have identified the gain in CPU time and the energy use by directly solving physics-based battery models with the DAE implementation in microgrid models.

2.2 MODELING AND SIMULATION OF PV ARRAYS & MPPT CONTROLLER

In this section, we compare one of the traditional Perturb and Observe (P&O) algorithms to a DAE-based algorithm for Maximum Power Point Tracking (MPPT) in a hypothetical microgrid architecture, consisting of PV arrays and MPPT controllers, as shown in Figure 2.1. We show that our depiction of MPPT algorithm as DAEs can be easily and efficiently simulated using DAE solvers. We report that the DAE-based MPPT algorithm, which enables high accuracy, simplicity, and low computation time, would facilitate maximized PV power output and simultaneous simulation of microgrid system. All simulations in this paper were carried out on a workstation with dual 8-core 3.1 GHz Intel Xeon processors with 32 GB RAM using Maple®-software.

2.2.1 *Mathematical modeling for PV arrays*

PV arrays generate power by converting solar energy directly to electricity. Typically, simulation of equivalent circuit-based models featuring one to three diodes has been the common approach to predict the PV arrays' performance [14]. For mathematical modeling of PV arrays, a single-diode equivalent circuit-based model is used (*see Figure 2.1*). This model offers a good balance between simplicity and accuracy by adjusting parameters and modifying the saturation current function to match the open-circuit voltage of the model with experimental data from the solar arrays for a broad range of temperatures. The I-V characteristics of the practical PV device, consisting of multiple cells in a parallel-series combination, is given as [15]:

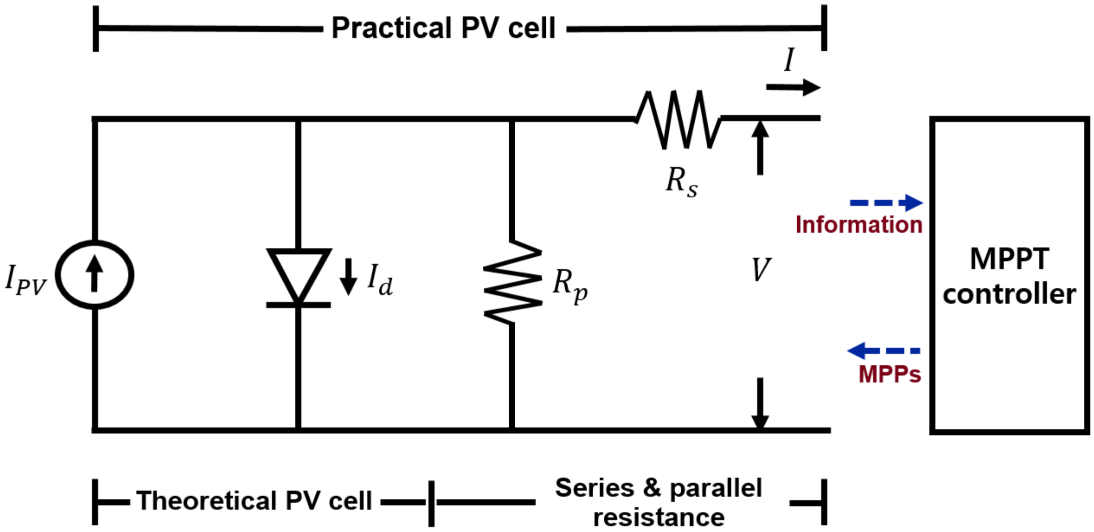

Figure 2.1. Single-diode equivalent circuit-based model of a practical PV cell and MPPT controller

$$I = I_{PV} - I_0\left[\exp\left(\frac{V + R_s I}{V_t a}\right) - 1\right] - \frac{V + R_s I}{R_p} \tag{2.1}$$

I is the PV arrays' output current, I_{PV} is the PV current, I_0 is the saturation current, and V_t is the thermal voltage. These variables are temperature-dependent, but simulation and control are conducted under the assumption that temperature is a constant (*see Table 2.3*). V is the PV arrays' output voltage, R_s is the series resistance, R_p is the parallel resistance, and a is the diode ideality constant. Meanwhile, the PV arrays' output current and voltage and PV current in Equation 2.1 can be expressed as a function of time by substituting $I = I(t)$, $I_{PV} = I_{PV}(t)$, and $V = V(t)$ as follows:

$$I(t) = I_{PV}(t) - I_0\left[\exp\left(\frac{V(t) + R_s I(t)}{V_t a}\right) - 1\right] - \frac{V(t) + R_s I(t)}{R_p} \tag{2.2}$$

All additional equations, variables, and parameters are shown in Table 2.1, 2.2, and 2.3, respectively [15].

Table 2.1. Equations for PV systems

Governing equation	**Additional equation**
$I(t)=I_{PV}(t)-I_0\left[\exp\left(\frac{V(t)+R_sI(t)}{V_ta}\right)-1\right]-\frac{V(t)+R_sI(t)}{R_p}$	$V_t=\frac{N_s\cdot k\cdot T}{q}$ $I_{PV}(t)=I_{PV,n}+\frac{K_I(T-T_n)\cdot G(t)}{G_n}$
$\frac{I(t)}{V(t)}=\frac{I_0\cdot\left(1-\frac{R_s\cdot I(t)}{V(t)}\right)\cdot\exp\left(\frac{V(t)+R_sI(t)}{V_ta}\right)}{V_ta}+\frac{1-\frac{R_s\cdot I(t)}{V(t)}}{R_p}$	$I_0=\frac{I_{sc,n}+K_I(T-T_n)}{\exp\left(\frac{V_{oc,n}+K_V(T-T_n)}{aV_t}\right)-1}$

Table 2.2. Variables for PV systems

Symbol	**Variable**	**Units**
$I(t)$	PV arrays output current	A
$I_{PV}(t)$	PV currents	A
$V(t)$	PV arrays output voltage	V
$G(t)$	Insolation	W/m^2
$P(t)$	Power Output	W

Table 2.3. Parameters for PV systems

Symbol	**Parameter**	**Values**	**Units**
R_s	Series resistance	0.221	Ω
a	Diode constant	1.3	-
R_p	Parallel resistance	415.405	Ω
N_s	Series-connected cells	54	-
k	Boltzmann constant	1.3806503×10^{-23}	J/K
q	Electron charge	1.60217646×10^{-19}	C
K_I	Current coefficient	0.0032	A/K
T_n	Nominal temperature	298.15	K
G_n	Nominal irradiation	1000	W/m^2
$I_{sc,n}$	Nominal short-circuit current	8.21	A
$V_{oc,n}$	Nominal open-circuit voltage	32.9	V
K_V	Voltage coefficient	-0.123	V/K
$I_{PV,n}$	Light-generated current at the nominal condition	8.214	A
T	Temperature	298.15	K

2.2.2 *P&O MPPT algorithm*

MPPT controllers can find Maximum Power Points (MPPs), and help PV arrays to produce peak power outputs. Various conventional MPPT algorithms such as P&O and Incremental Conductance (ICond) have widely been implemented as feedback algorithms. The P&O has been one of the most commonly used MPPT algorithms to track MPPs [16]. The P&O algorithm applies iterative processes toward MPPs by adjusting the output voltage of PV arrays with time and voltage step. The PV power at the present instant is obtained by measuring the value of the PV voltage and current, and the power at a future instant is compared to the present power after increasing or decreasing the voltage step. In the case of positive ΔP (difference in values between the future power and present power), the algorithm operates PV systems toward the optimal point by adding the voltage step. Otherwise, if ΔP is negative, the voltage value of the optimal point is determined by subtracting the voltage step. In the P&O algorithm, as the time step increases, simulation time decreases, while accuracy decreases, and vice versa [17].

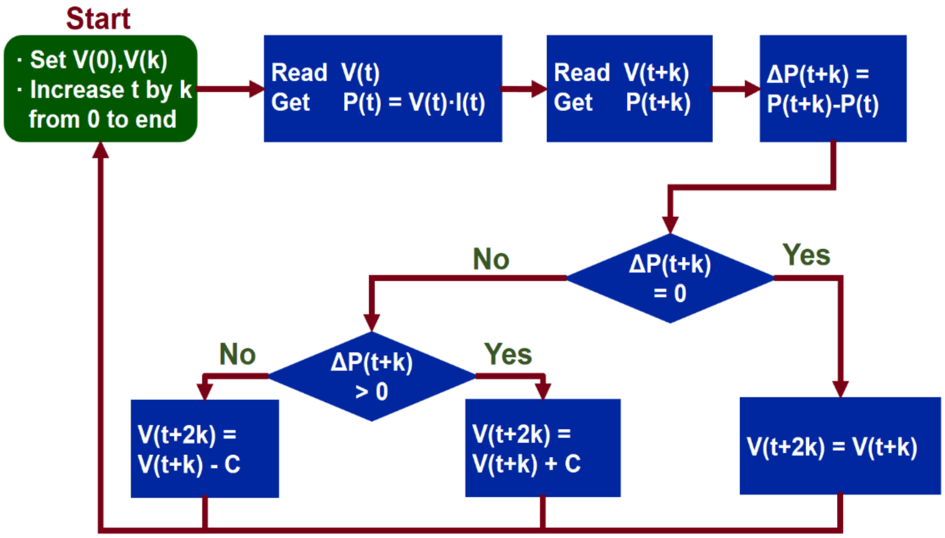

Figure 2.2. The flow chart of P&O MPPT algorithm. A trade-off occurs between the time/voltage step and accuracy. Therefore, it is important to determine the appropriate time/voltage step to achieve the best performance under the given environmental condition.

Also, the range of oscillation has a proportional relationship with the voltage step [17]. The flow chart of the P&O algorithm is presented in Figure 2.2. Even though the P&O algorithm is not able to track true MPPs, loses some amount of power due to oscillation around the MPP, and fails to track true MPPs because of its slow response to rapidly changing environmental conditions, the algorithm is the most popular, thanks to its simplicity and low hardware cost [18-22].

2.2.3 *DAE-based MPPT algorithm*

In this section we present a DAE-based implementation of MPPT algorithm. MPPs can be calculated from the following formula [23]

$$\frac{dP(V)}{dV} = \frac{d(I(V)\cdot V)}{dV} = 0 \tag{2.3}$$

in which $P(V)$ is the PV arrays' output power, $I(V)$ is the PV arrays' output current, and V is the PV arrays' output voltage. Note that both $P(V)$ and $I(V)$ are functions of the output voltage. We get Equation 2.4 by arranging Equation 2.3 as follows:

$$\frac{dI(V)}{dV} = -\frac{I(V)}{V} \tag{2.4}$$

Also, the PV arrays' output current in Equation 2.1 can be expressed as a function of voltage by substituting $I = I(V)$ as follows:

$$I(V) = I_{PV} - I_0\left[\exp\left(\frac{V + R_s I(V)}{V_t a}\right) - 1\right] - \frac{V + R_s I(V)}{R_p} \tag{2.5}$$

By differentiating Equation 2.5 with respect to *V*, we get

$$\frac{dI(V)}{dV} = -\frac{I_0\cdot\left(1 + R_s\cdot\frac{dI(V)}{dV}\right)\cdot\exp\left(\frac{V + R_s I(V)}{V_t a}\right)}{V_t a} - \frac{1 + R_s\cdot\frac{dI(V)}{dV}}{R_p} \tag{2.6}$$

By substituting Equation 2.4 into Equation 2.6, we get

$$\frac{I(V)}{V} = \frac{I_0 \cdot \left(1 - \frac{R_s \cdot I(V)}{V}\right) \cdot \exp\left(\frac{V + R_s I(V)}{V_t a}\right)}{V_t a} + \frac{1 - \frac{R_s \cdot I(V)}{V}}{R_p} \tag*{(2.7]}$$

Finally, substituting $I(V) = I(t)$, $V = V(t)$ in Equation 2.7 gives

$$\frac{I(t)}{V(t)} = \frac{I_0 \cdot \left(1 - \frac{R_s \cdot I(t)}{V(t)}\right) \cdot \exp\left(\frac{V(t) + R_s I(t)}{V_t a}\right)}{V_t a} + \frac{1 - \frac{R_s \cdot I(t)}{V(t)}}{R_p} \tag{2.8}$$

The DAE-based MPPT algorithm consists of two Algebraic Equations (AEs) in two variables (Equations 2.2 and 2.8; voltage and current as a function of time, respectively). The system's response time will significantly slow down in a real situation that involves dynamic environmental condition and long time-scale. For instance, one can use nonlinear equations solvers in computational software programs such as Maple, Maplesim, Matlab, and Simulink.

$$\frac{dy(t)}{dt} = 1 \tag{2.9}$$

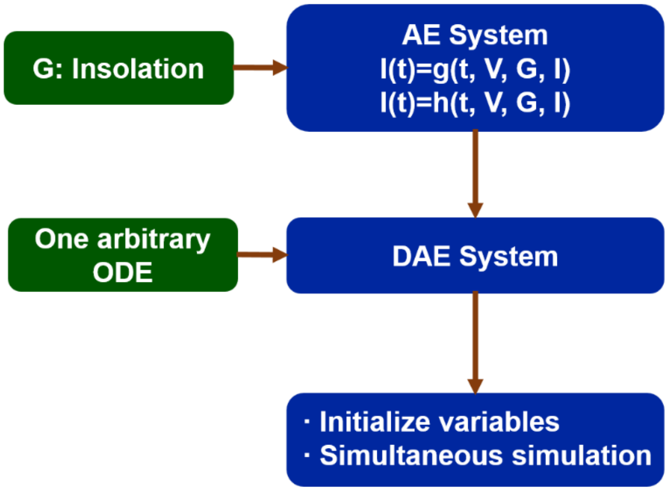

Figure 2.3. The flow chart of DAE-based MPPT algorithm. Proposed approach is 12 times faster than the P&O algorithm with higher accuracy (~1% more power) under the dynamic irradiance condition.

However, it would fail or need significantly high computation time due to the solvers' approach in finding the solution [24]. Here, we implement the DAE-based MPPT algorithm consisting of AEs only. In this case, one arbitrary Ordinary Differential Equation (ODE) (Equation 2.9), which does not affect any processes of the entire microgrid system, can be added to convert the AE system into a DAE system as shown in Figure 2.3.

2.2.4 *Results*

An example of a short time simulation with the P&O and DAE-based MPPT algorithm is shown in Figure 2.4. This will help analyze the DAE-based algorithm's performance including its accuracy, reliability, and computation time. The voltage and time step in the P&O algorithm were adjusted (0.01V and 0.001s) to produce high accuracy, thereby explicitly identifying the CPU time difference between the P&O and DAE-based MPPT algorithms. Equations 2.2, 2.8, and 2.9 were implemented for the DAE-based MPPT algorithm. At the beginning of the simulation, when t = 0, the irradiance is assumed to be 400 W/m^2 and it is increased up to 800 W/m^2 within a very short time. After that, the irradiance is kept at 800, 400, 1000, 50, 600, and 200 W/m^2 for 10 seconds each and decreased to 100 W/m^2 as illustrated in Figure 2.4a. Even though the whole-time scale is small (60 seconds), rapidly changing irradiance from 50 to 1000 W/m^2 was tested for the P&O and DAE-based MPPT algorithms' reliability. Also, solar output powers are plotted over voltage outputs at each irradiance level from Equation 2.5 as shown in Figure 2.4b. In Figures 2.4c and 2.4d, voltage and current output responses are presented by implementing the P&O and DAE-based MPPT algorithms. All MPPs in Figure 2.4b were rounded off to the 6th decimal place, and all the values of MPPs from the DAE-based MPPT algorithm at each irradiance level exactly matched to the results from Equation 2.5 with low CPU time (~0.125 s). On the other hand, the

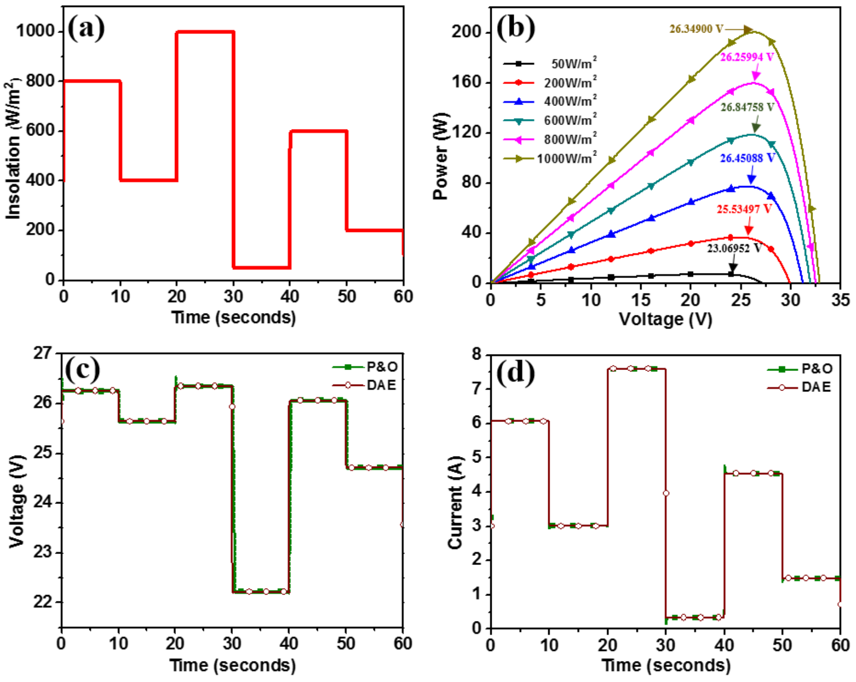

Figure 2.4. Simple case study with different irradiance values. (a) Solar irradiance at 800, 400, 1000, 50, 600, and 200 W/m2 for 10 seconds, respectively. (b) Solar power outputs over voltage from the single-diode equivalent circuit-based model. (c) Voltage outputs (d) Current outputs, from DAE-based (wine color and empty circle) and P&O (dark green color and filled square) MPPT algorithms. In this simulation, the P&O algorithm produces the same power as the proposed DAE-based algorithm, but computation cost is ~224 times higher.

CPU time of the P&O algorithm was significantly slower (27.971 s) than the DAE-based MPPT algorithm with lesser accuracy. This case study clearly illustrates the DAE-based MPPT algorithm's high accuracy, reliability, and computational speed over the traditional P&O MPPT algorithm.

2.3 MODELING OF PV ARRAYS WITH MPPT CONTROLLER & POWER ELECTRONICS COMPONENTS

In this section, we present a system with a bidirectional DC/DC converter and bidirectional DC/AC inverter (DC: Direct Current, AC: Alternative Current) that are added to the PV arrays, as shown in Figure 2.5. We compare combined PV systems' performance between the P&O and DAE-based MPPT algorithms with mathematical models of power electronics in PV microgrids under the dynamic irradiance condition. Raw irradiance data were chosen from NREL's Measurement and Instrumentation Data Center (MIDC) based on ten-minute resolution data [20].

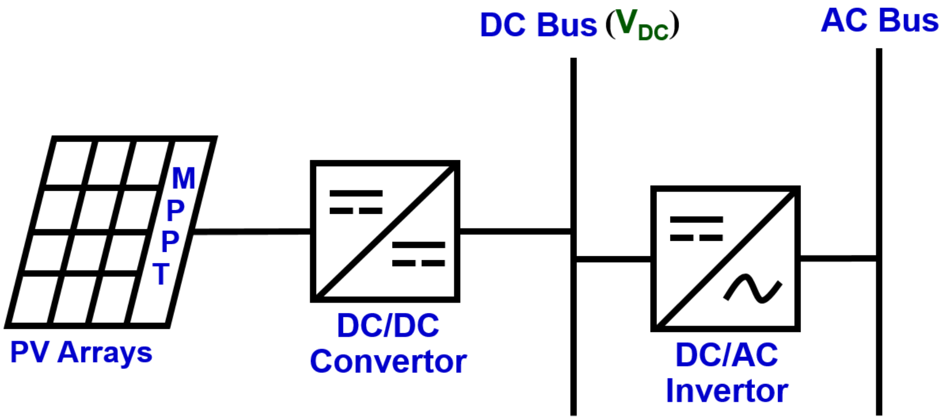

Figure 2.5. System configuration of a stand-alone PV microgrids, consisting of PV systems, a bidirectional DC/DC converter, a bidirectional DC/AC inverter.

2.3.1 *Power electronics components*

A bidirectional DC/DC converter is used for PV systems, stepping up/down voltages from its input to output. It regulates output voltages and maintains a constant voltage across DC bus from varying voltages of PV systems under the assumption that there are no energy losses. Here, the voltage value (V_{dc}) across the DC bus was fixed at 100V, which was accomplished by increasing or decreasing the duty cycle, which is performed by using Pulse Width Modulation (PWM) of the square-wave pulses to the switches of the DC/DC converter [25]. The equations implemented for the bidirectional DC/DC converter are [26]:

$$I_{dc,PV}(t) = \left(1 - D_{PV}(t)\right) \cdot I_{PV,out}(t) \tag{2.10}$$

$$V_{dc} = \frac{1}{1 - D_{PV}(t)} V_{PV,out}(t) \tag{2.11}$$

$I_{dc,PV}(t)$ is the DC bus current, $V_{PV,out}(t)$ is the output voltage, $I_{PV,out}(t)$ is the output current, and $D_{PV}(t)$ is the duty ratio of the DC/DC converter, from PV systems. A bidirectional DC/AC inverter, which changes DC to AC or AC to DC, is implemented, since most standard appliances run on AC on the consumer side. Here, the conversion efficiency (η) is fixed as 0.85.

$$P_{out,PV}(t) = \eta \cdot P_{in,PV}(t) \tag{2.12}$$

$P_{out,PV}(t)$ is the output power from the DC/AC inverter, and $P_{in,PV}(t)\left(= V_{dc} \cdot I_{dc,PV}(t)\right)$ is the input power from the DC/DC converter connected to PV systems.

2.3.2 *Results*

The MPPT simulation for PV arrays was conducted for a single day in LA, in April 2010 as shown in Figure 2.6. PV arrays were scaled up to kilowatt-scale systems. Figure 2.6a shows that the sun rises at 6 AM, and solar irradiance rises and falls until 7 PM. Under the rapidly changing environmental conditions, voltage and time step in the P&O algorithm need to be calibrated to produce the best performance as shown in Table 2.4. When the voltage step is 0.1V, the maximum power output is generated, and computation time decreases with a small decrease in power as the time step increases. In other words, when the time step is increasing from 5 to 20 seconds, power outputs are the maximum in the voltage step of 0.1V. Also, the time step of 15 seconds has a good balance between computation time and power outputs. Accordingly, the time and voltage step are fixed as 15 seconds and 0.1V, respectively. For the DAE-based MPPT algorithm, Equations 2.2, 2.8, 2.9, 2.10, 2.11, and 2.12 were implemented. The DAE-based MPPT simulation's total CPU time is 0.702 seconds, which is 12 times faster than the P&O algorithm with more power (P&O: 1307.96kWh, DAE: 1308.89kWh), as shown in Figure 2.6b. Also, while the P&O produces oscillations around MPPs (*see Figures 2.6c and 2.6d*), the DAE-based MPPT algorithm precisely follows MPPs. It is evident that the amount of energy loss will increase as the PV systems' scale increases.

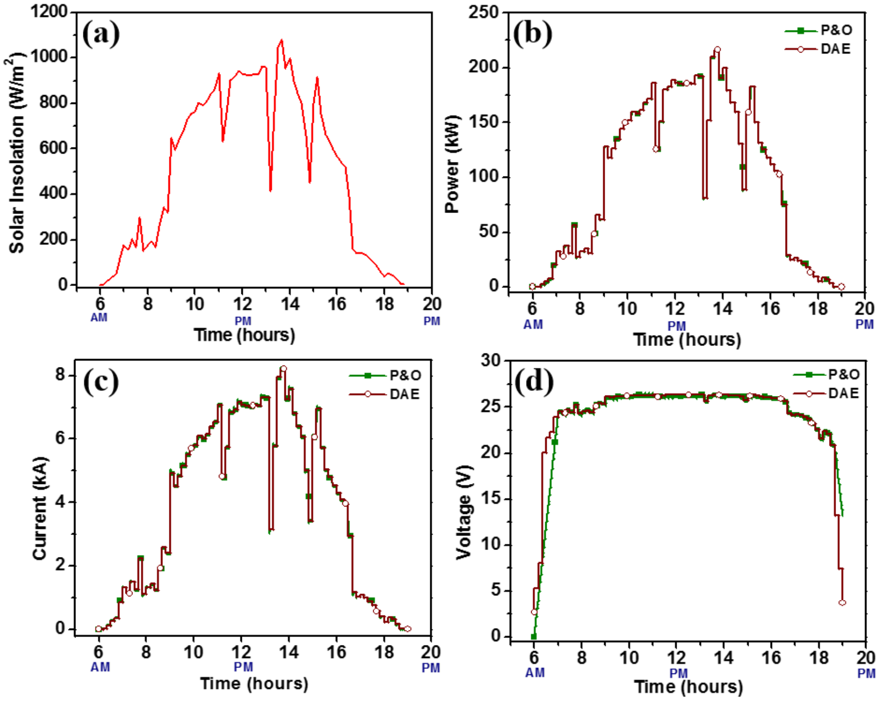

Figure 2.6. Comparison of voltage, current and power outputs between P&O and DAE-based MPPT algorithm. (voltage step = 0.1 V, time step = 15 seconds) (a) Solar irradiance in LA in April 10th, 2010. (b) Power outputs (c) Current outputs (d) Voltage outputs, from the proposed DAE (wine color and empty circle) and P&O (dark green color and filled square) MPPT algorithms. In (b), the proposed approach produces ~1% more power than the P&O algorithm for a single day. These small differences accumulate over time resulting in significant energy and cost savings. In (c) and (d), the DAE-based algorithm can track MPPs much quickly and has no oscillations compared to the P&O algorithm.

Table 2.4. Calibration of P&O algorithm by adjusting voltage and time step

		Time step (s)				
Voltage step (V)	CPU time (s) Power (kW)	1	5	10	15	20
0.05	CPU time	168.965	26.863	12.855	8.502	6.006
	Power	1308.834	1308.540	1305.880	1297.877	1287.782
0.1	CPU time	171.133	27.955	13.011	8.767	6.208
	Power	1308.792	1308.682	1308.441	1307.965	1305.725
0.5	CPU time	171.632	27.753	14.196	9.094	6.272
	Power	1306.564	1306.424	1306.249	1306.073	1305.810
0.1	CPU time	173.566	27.285	13.276	8.487	6.302
	Power	1301.177	1300.970	1300.711	1300.452	1300.124

2.4 MODELING OF PV ARRAYS WITH MPPT CONTROLLER, BATTERY & POWER ELECTRONICS COMPONENTS

Batteries and power electronics components connected to the batteries are added to the system explained in section 2.3, as shown in Figure 2.7 [25], representing a typical microgrid with generation and storage. In this section, we show the performance of the reformulated Pseudo-2-Dimensional (P2D) battery model [27] with the DAE-based MPPT algorithm in this PV-Battery microgrid. All simulations were conducted under the same environmental conditions as in the previous section. A single-step solution approach has been applied in this large simulation, which allows for DAEs in microgrid controls to be solved without a priori knowledge of exact initial conditions for algebraic variables [28].

2.4.1 *Conventional and proposed control algorithm*

Implementation of highly non-linearized DAEs in detailed battery models with MPPT feedback algorithms such as P&O and ICond causes a significant time-delay as the controls consume computation time at every time step [29-31]. However, once the DAE-based MPPT algorithm is efficiently simulated as illustrated in the earlier sections, adding efficient models for batteries is straightforward. The mathematical structure of the DAE-based MPPT helps easily add battery and power electronic models in the microgrid architecture (see Equations 2.2 and 2.8). For example, even the reformulated P2D model, one of the highly non-linearized DAE battery systems, which includes several important internal variables simulated at a reasonable computation time [27], can be simply incorporated into DAE-based MPPT algorithm, power electronics, and PV arrays mathematical models. Instead of adding one arbitrary equation (Equation 2.9), the combination of reformulated P2D battery, power electronics, PV arrays, and the DAE-based MPPT mathematical

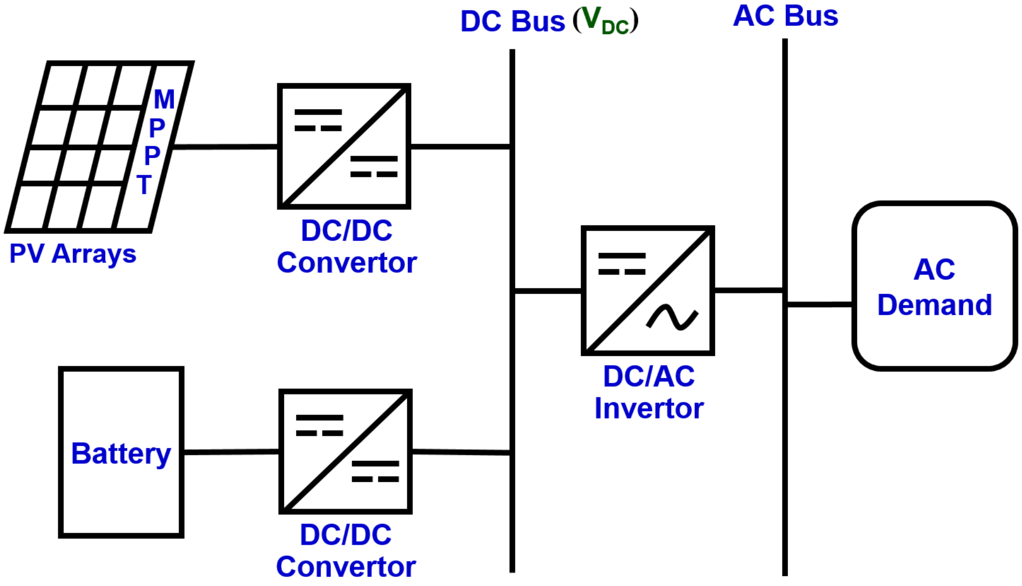

Figure 2.7. System configuration of a stand-alone PV-Battery microgrid, consisting of PV systems, bidirectional DC/DC converters, a bidirectional DC/AC inverter, and batteries.

models, which includes several ODEs and AEs, becomes a system of DAEs as shown in Figure 2.8. The DAE solvers in the computational software allow the entire microgrid system to be simulated simultaneously with high accuracy and low computation time under rapidly changing environmental conditions [24, 32]. As more detailed physics-based battery models are involved in the entire microgrid, the DAE-based MPPT algorithm will be better suited for simultaneous simulations under real environmental conditions.

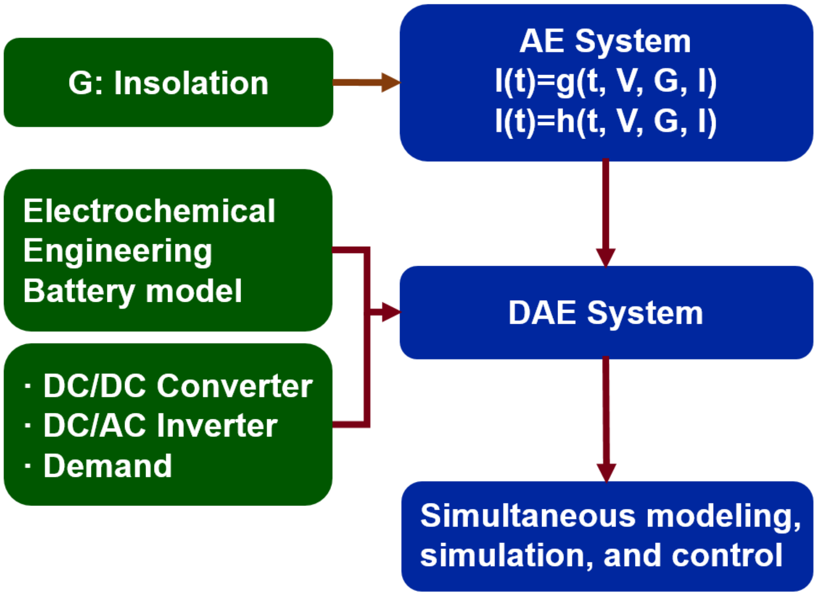

Figure 2.8. Simultaneous modeling, simulation, and control of microgrids, including DAE-based MPPT algorithm and electrochemical engineering battery model. Implementation of physics-based battery models incorporating current microgrid controls consumes considerable computation time. This is perhaps one of the reasons why empirical battery models are commonly used in grid communities. The proposed direct DAE implementation approach enables real-time simulation of physics-based models in microgrids

2.4.2 *Reformulated P2D battery model*

An ideal battery model would provide good prediction while maintaining minimal computational cost. The porous electrode P2D model, which is one of electrochemical engineering models, includes several significant internal variables and has a predictive capability for battery simulations [1, 33]. The P2D model is one of the most accurate and experimentally validated physics-based battery models that allows for modeling of critical internal states used in the literature. The simulations are conducted on a mathematically reformulated P2D model that enables entire microgrid simulations to be solved in a reasonable time [27, 33]. High accuracy and short computation time of the reformulated P2D model are well suited for grid applications [34]. The reformulated model discretizes dependent variables as a series of trial functions, rather than a finite difference approach, using coordinate transformation and orthogonal collocation [27]. Also, the Solid Electrolyte Interphase (SEI) layer is modeled by considering irreversible side reactions. During charging operations, some of the cyclable lithium ions are removed by reactions between the lithium ions and electrolyte, and the reactions create a passivation layer around the anode, which is described by Butler-Volmer kinetics (see Table 2.6) [35, 36]. Equations, variables, and parameters related to the reformulated P2D model are arranged in Table 2.5-2.8 [1, 27, 33, 35, 36].

Table 2.5. Governing equations for Li-ion P2D model

Governing equation	**Boundary conditions**
Positive	
$\varepsilon_{\text{p}} \frac{\partial c}{\partial t} = \frac{\partial}{\partial x}\left[D_{\text{eff,p}} \frac{\partial c}{\partial x} \right] + a_{\text{p}} \left(1 - t_{+}\right) j_{\text{p}}$	$\frac{\partial c}{\partial x} \rvert_{x=0} = 0$
	$-D_{eff,p} \frac{\partial c}{\partial x} \rvert_{x=l_p^-} = -D_{eff,s} \frac{\partial c}{\partial x} \rvert_{x=l_p^+}$
$-\sigma_{\text{eff,p}} \left(\frac{\partial \Phi_1}{\partial x} \right) - \kappa_{\text{eff,p}} \left(\frac{\partial \Phi_2}{\partial x} \right) + \frac{2\kappa_{\text{eff,p}} RT}{F} \left(1 - t_{+}\right) \left(\frac{\partial \ln c}{\partial x} \right) = I$	$\frac{\partial \Phi_2}{\partial x} \rvert_{x=0} = 0$
	$-\kappa_{\text{eff,p}} \frac{\partial \Phi_2}{\partial x} \rvert_{x=1_p^-} = -\kappa_{\text{eff,s}} \frac{\partial \Phi_2}{\partial x} \rvert_{x=1_p^+}$
$\frac{\partial}{\partial x}\left[\sigma_{\text{eff,p}} \frac{\partial \Phi_1}{\partial x} \right] = a_{\text{p}} F j_{\text{p}}$	$\frac{\partial \Phi_1}{\partial x} \rvert_{x=l_p^-} = 0$ $\left.\frac{\partial \Phi_1}{\partial x}\right\rvert_{x=0} = -\frac{I}{\sigma_{eff,p}}$
$\frac{\partial}{\partial t} c_p^{s,ave} = -3 \frac{j_p}{R_p}, \frac{D_{s,\text{p}}}{R_p} (c_p^{s,surf} - c_p^{s,ave}) = -\frac{j_p}{5}$	
Separator	
$\varepsilon_s \frac{\partial c}{\partial t} = \frac{\partial}{\partial x}\left[D_{\text{eff,s}} \frac{\partial c}{\partial x} \right]$	$c \rvert_{x=l_p^-} = c \rvert_{x=l_p^+}$ $c \rvert_{x=l_p+l_s^-} = c \rvert_{x=l_p+l_s^+}$
$-\kappa_{\text{eff,s}} \left(\frac{\partial \Phi_2}{\partial x} \right) + \frac{2\kappa_{\text{eff,s}} RT}{F} \left(1 - t_{+}\right) \left(\frac{\partial \ln c}{\partial x} \right) = I$	$\Phi_2 \rvert_{x=l_p^-} = \Phi_2 \rvert_{x=l_p^+}$ $\Phi_2 \rvert_{x=l_p+l_s^-} = \Phi_2 \rvert_{x=l_p+l_s^+}$
Negative electrode	
$\varepsilon_n \frac{\partial c}{\partial t} = \frac{\partial}{\partial x}\left[D_{\text{eff,n}} \frac{\partial c}{\partial x} \right] + a_n \left(1 - t_{+}\right) j_n$	$\frac{\partial c}{\partial x} \rvert_{x=l_p+l_s+l_n} = 0$
	$-D_{eff,s} \frac{\partial c}{\partial x} \rvert_{x=l_p+l_s^-} = -D_{eff,n} \frac{\partial c}{\partial x} \rvert_{x=l_p+l_s^+}$
$-\sigma_{\text{eff,n}} \left(\frac{\partial \Phi_1}{\partial x} \right) - \kappa_{\text{eff,n}} \left(\frac{\partial \Phi_2}{\partial x} \right) + \frac{2\kappa_{\text{eff,n}} RT}{F} \left(1 - t_{+}\right) \left(\frac{\partial \ln c}{\partial x} \right) = I$	$\Phi_2 \rvert_{x=1_p+l_s+l_n} = 0$ $-\kappa_{\text{eff,s}} \frac{\partial \Phi_2}{\partial x} \rvert_{x=1_p+l_s^-} = -\kappa_{\text{eff,n}} \frac{\partial \Phi_2}{\partial x} \rvert_{x=1_p+l_s^+}$
$\frac{\partial}{\partial x}\left[\sigma_{\text{eff,n}} \frac{\partial}{\partial x} \Phi_1 \right] = a_n F j_n$	$\left.\frac{\partial \Phi_1}{\partial x}\right\rvert_{x=l_p+l_s^-} = 0$ $\frac{\partial \Phi_1}{\partial x} \rvert_{x=l_p+l_s+l_n} = -\frac{I}{\sigma_{eff,n}}$
$\frac{\partial}{\partial t} c_n^{s,ave} = -3 \frac{j_n}{R_n}, \frac{D_{s,n}}{R_n} (c_n^{s,surf} - c_n^{s,ave}) = -\frac{j_n}{5}$	

Table 2.6. Additional equations for Li-ion P2D model

$$U_p = \frac{-4.656 + 88.669\theta_p^2 - 401.119\theta_p^4 + 342.909\theta_p^6 - 462.471\theta_p^8 + 433.434\theta_p^{10}}{-1 + 18.933\theta_p^2 - 79.532\theta_p^4 + 37.311\theta_p^6 - 73.083\theta_p^8 + 95.96\theta_p^{10}}$$

$$j_p = 2c^{0.5} \cdot k_p \cdot c^s \,|_{r=R_p}^{0.5} \left(\mathrm{c}_{\max,p}^s - c^s \,|_{r=R_p}\right)^{0.5} \sinh\left(\frac{\alpha F}{RT}\left(\Phi_1 - \Phi_2 - U_p\right)\right)$$

$$j_n = 2c^{\,0.5} \cdot k_n \cdot c^s \,|_{r=R_n}^{0.5} \left(\mathrm{c}_{\max,n}^s - c^s \,|_{r=R_n}\right)^{0.5} \sinh\left(\frac{\alpha F}{RT}\left(\Phi_1 - \Phi_2 - U_n - \frac{\delta \cdot F \cdot (j_n + j_{SEI})}{\kappa_{SEI}}\right)\right)$$

$$U_n = 0.7222 + 0.1387\theta_n + 0.029\theta_n^{0.5} - \frac{0.0172}{\theta_n} + \frac{0.0019}{\theta_n^{1.5}}$$

$$+0.2808\exp\left(0.90 - 15\theta_n\right) - 0.7984\exp\left(0.4465\theta_n - 0.4108\right)$$

$$\kappa_{eff,i} = \varepsilon_i^{brugg}\begin{pmatrix} 4.1253\times10^{-2} + 5.007\times10^{-4}c - 4.7212\times10^{-7}c^2 \\ +1.5094\times10^{-10}c^3 - 1.6018\times10^{-14}c^4 \end{pmatrix}, i = p,s,n$$

$$D_{eff,i} = D \cdot \varepsilon_i^{brugg}, i = p,s,n$$

$$\sigma_{eff,i} = \sigma_i \cdot \left(1 - \varepsilon_i - \varepsilon_{f,i}\right), i = p,n$$

$$a_i = \frac{3}{R_i}(1 - \varepsilon_i - \varepsilon_{f,i}),\ i = p,s,n;\ \theta_p = \frac{c^s \,|_{r=R_p}}{c_{\max,p}^s};\ \theta_n = \frac{c^s \,|_{r=R_n}}{c_{\max,n}^s}$$

$$\frac{\partial\delta}{\partial t} = \frac{j_{SEI} M_{SEI}}{\rho_{SEI}}$$

$$j_{SEI} = -\frac{k_{SEI}}{F}\exp\left(-\alpha\frac{F}{RT}\left(\Phi_1 - \Phi_2 - U_{SEI} - \frac{\delta \cdot F \cdot \left(j_n + j_{SEI}\right)}{\kappa_{SEI}}\right)\right)$$

Table 2.7. List of variables for Li-ion P2D model

Symbol	**Variables**	**Units**
c	Electrolyte concentration	mol/m^3
c_i^s	Solid phase concentration	mol/m^3
Φ_1	Solid phase potential	V
Φ_2	Liquid phase potential	V
$c^{s,surf}$	Solid phase concentration at surface	mol/m^3
$c^{s,ave}$	Average solid phase concentration	mol/m^3
I	Applied current density	A/m^2
U_i	Open circuit potential at positive $(i=p)$ and negative $(i=n)$	V
j_i	Pore wall flux at positive $(i=p)$ and negative $(i=n)$	mol/m^2/s
$\kappa_{eff,i}$	Liquid phase conductivity at positive $(i=p)$, separator $(i=s)$, and negative $(i=n)$	S/m
$D_{eff,i}$	Effective diffusion coefficient conductivity at positive $(i=p)$, separator $(i=s)$, and negative $(i=n)$	m^2/s
$\sigma_{eff,i}$	Effective solid phase conductivity at positive $(i=p)$ and negative $(i=n)$	S/m
θ_i	State of charge at positive $(i=p)$ and negative $(i=n)$	-
j_{SEI}	Flux associated with SEI layer growth	mol/m^2/s
c_{sol}	Concentration of solvent at anode surface	mol/m^3
c_{Li^+}	Concentration of electrolyte at anode surface	mol/m^3
δ	SEI layer thickness	m

Table 2.8. Parameters for Li-ion P2D model

Symbol	Parameter	Positive Electrode	Separator	Negative Electrode	Units
σ_i	Solid phase conductivity	100		100	S/m
$\varepsilon_{f,i}$	Filler fraction	0.025		0.0326	-
ε_i	Porosity	0.385	0.724	0.485	-
$Brugg$	Bruggman Coefficient	4	4	4	-
D	Electrolyte diffusivity	7.5×10^{-10}	7.5×10^{-10}	7.5×10^{-10}	m^2/s
D_i^s	Solid Phase Diffusivity	1.0×10^{-14}		3.9×10^{-14}	m^2/s
k_i	Reaction Rate constant	2.334×10^{-11}		5.031×10^{-11}	$m^{2.5}/(mol^{0.5}\, s)$
$c_{i,\max}^s$	Maximum solid phase concentration	51554		30555	mol/m^3
$c_{i,0}^s$	Initial solid phase concentration	25751		26128	mol/m^3
c_0	Initial electrolyte concentration	1000	1000	1000	mol/m^3
$R_{p,i}$	Particle Radius	2.0×10^{-6}		2.0×10^{-6}	m
a_i	Particle Surface Area to Volume	885000		723600	m^2/m^3
l_i	Region thickness	80×10^{-6}	25×10^{-6}	88×10^{-6}	m
t_+	Transference number		0.364		-
F	Faraday's Constant		96487		C/mol
R	Gas Constant		8.314		J/(mol·K)
T	Temperature		298.15		K
ρ	Density	2500	1100	2500	kg/m^3
k_{SEI}	Rate constant for SEI			1.5×10^{-6}	A/m^2
α	Transfer coefficient	0.5		0.5	-
U_{SEI}	Open circuit potential for SEI layer			0.4	V
κ_{SEI}	Conductivity of SEI layer			1	S/m
ρ_{SEI}	Density of SEI layer			2.1×10^3	kg/m^3
M_{SEI}	Molecular weight of SEI			0.026	kg/mol

2.4.3 *Simulation of Battery operation*

Batteries are charged through the power from the PV arrays converted by the DC/AC inverter and discharged based on users' demands on the microgrid. The solar energy converted by the DC/AC inverter will be provided directly to users on the microgrid for any demand below the level of the solar power, and batteries will be charged with any power available above the level of demand. In contrast, when the converted solar power decreases below the desired level of demand, batteries will be discharged to provide the stored energy to the users. The bidirectional DC/DC converter is connected to batteries in the same manner as the PV systems' configuration. Also, the role of power electronics connected to batteries, the voltage value across the DC bus, and the bidirectional DC/AC inverter's conversion efficiency are assumed to be the same as the PV systems were described in the previous section. The DC/DC converter's equations are [26]:

$$I_{dc,battery}(t) = \left(1 - D_{battery}(t)\right) \cdot I_{battery,out}(t) \tag{2.13}$$

$$V_{dc} = \frac{1}{1 - D_{battery}(t)} V_{battery,out}(t) \tag{2.14}$$

$$P_{in,battery}(t) = I_{dc,battery}(t) \cdot V_{dc} \tag{2.15}$$

$I_{dc,battery}(t)$ is the DC bus current, $V_{battery,out}(t)$ is the output voltage, $I_{battery,out}(t)$ is the output current, and $D_{battery}(t)$ is the duty ratio of the DC/DC converter, from batteries. For the bidirectional DC/AC inverter, the amount of DC/AC inverter's output power $\left(P_{out,battery}(t)\right)$ supplied by batteries' power $\left(P_{in,battery}(t)\right)$ can be calculated based on the relation between the input and output power in Equation 2.12 as shown below:

$$P_{out,battery}(t) = \eta \cdot P_{in,battery}(t) \tag{2.16}$$

$P_{out,battery}(t)$ is the output power from the DC/AC inverter, and $P_{in,battery}(t)$ is the input power from the DC/DC converter connected to batteries. Batteries are operated to make up the difference between the demand $\left(P_{demand}(t)\right)$ and the PV arrays' power $\left(P_{out,PV}(t)\right)$ converted by the DC/AC inverter.

$$P_{out,battery}(t) = P_{out,PV}(t) - P_{demand}(t) \tag{2.17}$$

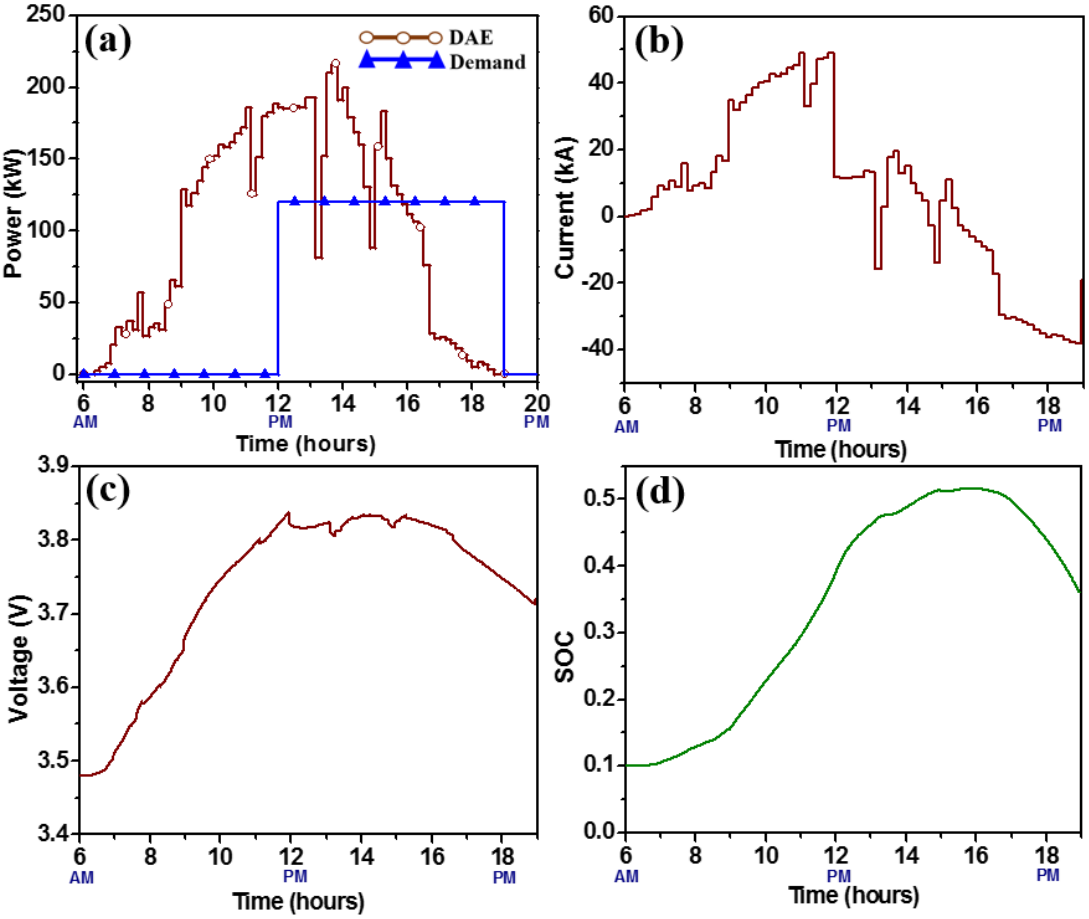

Figure 2.9. Performance of reformulated P2D battery model under dynamic irradiation condition. (a) Solar power outputs from DAE-based MPPT (wine color and empty circle) and demand (blue color and filled triangle). (b) Current outputs (c) Voltage outputs (d) SOC. The proposed approach enables aggressive control of batteries for microgrids as internal variables are predicted accurately in real-time

By substituting Equations 2.12 and 2.16 into Equation 2.17, we get

$$P_{in,battery}(t) = P_{in,PV}(t) - \frac{P_{demand}(t)}{\eta} \tag{2.18}$$

2.4.4 *Results*

The reformulated P2D model for single cathode/separator/anode cell sandwich was scaled up to a kilowatt-scale system corresponding to the power level of PV systems and demands (assuming no loss in performance). A 1500 kWh sized battery with 10% initial state of charge (SOC) was used in the simulation to illustrate the efficiency of the P2D model along with the fast computation time in proposed microgrid controls. Cost and energy savings by implementing the proposed control strategy including the electrochemical engineering model and DAE-based MPPT algorithm is also presented. The demand starts at 12 PM and continues until 7 PM at a constant value (120kW), as shown in Figure 2.9a. The total demand is 840 kWh. The power obtained from solar arrays, using

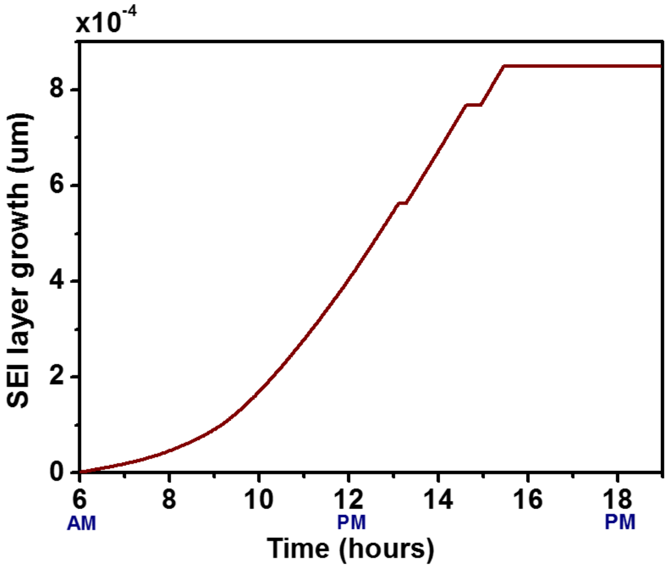

Figure 2.10. SEI layer growth predicted by the P2D battery model. The proposed approach enables real-time prediction of capacity degradation in a particular cycle. Fast simulation of degradation of batteries over multiple cycles will be useful for improving the life of the batteries for microgrid applications.

the P&O and DAE-based MPPT algorithm, are 1307.96 kWh and 1308.89 kWh, respectively. The battery will be discharged when the demand is greater than the power supplied from solar arrays, and vice versa (see Figure 2.9b). In other words, when batteries' current is below zero, which means demand is greater than solar array's power, batteries are discharged. In Figures 2.9c and 2.9d, the reformulated P2D model predicts voltage and SOC accurately with reasonable CPU time. The proposed control scheme's running time is only 19.157 seconds for a single day simulation. As we mentioned before, lithium-ion batteries are the most expensive single component accounting for about 60% of overall CapEx among the whole microgrid components [8]. Total costs of microgrids currently range between 583 and 1166 $/kWh [8]. Accordingly, total costs of the lithium-ion batteries in CapEx is between 350 and 700 $/kWh. For example, if we can reduce the battery size by 50%, total cost of the battery system will decrease to 175-350$/kWh with significant reduction in total cost for large-scale microgrids. Simple empirical/equivalent-circuit or black-box battery models will not be able to capture the essential dynamics of battery performance accurately and will provide poor estimates of cell size and costs. The proposed approach is fundamentally different from the existing microgrid control architecture. Instead of treating cells as a black box, critical internal states will be addressed with high accuracy and capable of being simulated in real-time. For example, SEI layer growth from the reformulated P2D battery model is presented in Figure 2.10. The SEI layer causes lithium ions' diffusion resistance and a voltage drop across the battery. Including the SEI layer growth as an internal variable can be used to control the capacity fade over cycles [34]. Even though capacity fade/degradation is accelerated by extreme charging patterns, increased temperature, and overcharging, the batteries degrade even under normal operation.

2.5 PRACTICAL IMPACT AND IMPLEMENTATION INTO A MICROCONTROLLER

Current state of the art typically involves using empirical models for batteries in grid simulation. Recently, aggressive and efficient control strategies for grid and renewable grids are heavily supported by the U.S. Department of Energy [37, 38]. However, current perception amongst the grid community is that physics-based battery models are too complicated to be used in grid control. We hope that this paper shows that aggressive control strategies for renewable grids can benefit from real-time simulation of physics-based battery models. In this section, we illustrate that the DAE-based microgrid control can be implemented in a low-cost microcontroller, while performing better than current microgrid algorithms. Lithium-ion battery packs in grid or otherwise are always connected to a Battery Management System (BMS). BMSs are devices that are responsible for safely operating the battery [39]. With a microcontroller or a microprocessor onboard, a BMS can be made to operate the battery for satisfying desired control goals. To make the DAE-based microgrid control commercially viable, we must be able to simulate the model in a low-cost microcontroller in real-time. As a proof-of-concept, we have used a BeagleBone Black (BBB) to represent such a microprocessor system with minimal computing specifications. BBB has 512 MB of onboard RAM with Cortex ARM processor running Linux [40] and is the size of a credit card. An open source free solver IDA, which is part of SUNDIALS [41], simulates the PV array with the DAE-based MPPT controller and power electronics (see section 2.3) in 1.1 seconds and the implementation of the reformulated P2D battery model with other microgrid components (see section 2.4) in 2.8 seconds.

2.6 PERSPECTIVES

Batteries in the microgrid system need to be understood well for accurate characterization, and an intelligent management system to monitor and maintain economic, safe and optimal operations. Conventional battery controls in the microgrid only allow for meeting the power demand but lack predictability and accuracy. This work provides new insights for research on microgrid control strategy for the following reason: simultaneous modeling, simulation, and control by incorporating physics-based electrochemical engineering battery models along with PV arrays, DAE-based MPPT algorithm, and power electronics. Our findings show that the proposed microgrids control, including the DAE-based MPPT feedback algorithms with P2D battery models, is capable of saving a significant amount of energy and cost. Proposed controls approach would help optimize the performance of batteries in microgrids. Also, proposed controls simulate the performance of individual components in the microgrid simultaneously and meet the grid constraints. Our current and future work involves performing optimal and model predictive control strategies to improve the performance of battery stacks for grid applications for improved life, deeper depth of discharge, reduced levelized cost, and to enable and benefit from two bidirectional flow of information, energy and control actions from both batteries and the rest of the grid. Advanced controls based on proposed modeling and control techniques would reduce the induced degradation of batteries and improve the performance of the overall microgrid system.

Chapter 3. VANADIUM REDOX BATCH CELL SYSTEMS

In this chapter, we study, analyze, and validate some important zero-dimensional physics-based models for Vanadium Redox Batch Cell (VRBC) systems and formulate an adequate physics-based model which can predict the battery performance accurately.

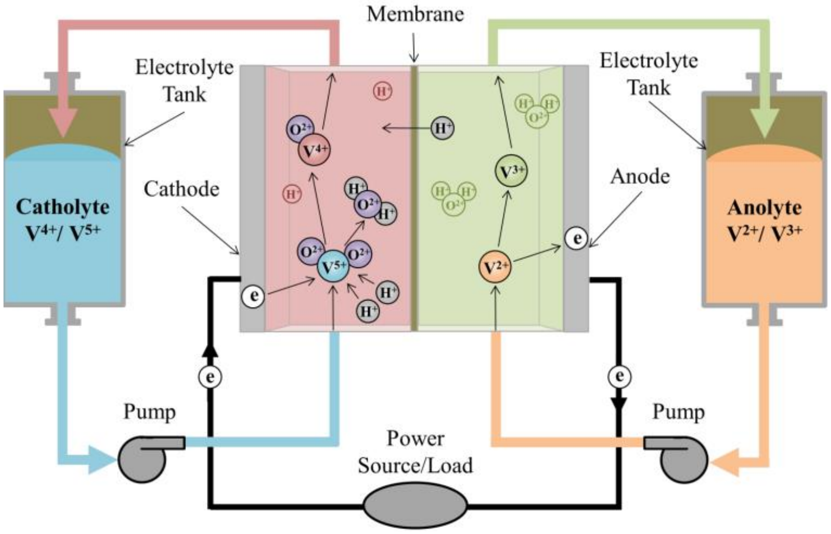

Figure 3.1. Schematic of a vanadium redox flow battery showing membrane, electrolytes, electrodes, and reservoirs. Redox flow batteries (RFBs) are one of the most promising routes to achieving this objective because of large energy storage capacity that is only limited by tank sizes and electrolyte concentrations.

In the model formulation process, a systems approach to multiple parameters estimation has been conducted, using VRBC systems at low C-rates (~ C/30). In this batch cell system, the effect of ions' crossover through the membrane is dominant, and therefore, capacity loss phenomena can be explicitly observed. Paradoxically, this means that using the batch system might be a better approach to identifying a more suitable model describing the effect of ions transport. Next, we propose an efficient systems approach, which enables to help understand the battery performance quickly by estimating all parameters of the battery system. Lastly, open source codes, executable files, and experimental data are provided to enable people's access to robust and accurate models and optimizers. In battery simulations, different models and optimizers describing the same systems produce different values of the estimated parameters. Providing an open access platform can accelerate the process to arrive at robust models and optimizers by continuous modification from users' side.

3.1 SIGNIFICANT AND IMPACT

Redox Flow Batteries (RFBs) are promising energy storage systems for grid/microgrid applications [42]. There has been significant technological progress in the recent past towards, meeting the growing need for large-scale energy storage systems such as RFBs [12]. Among different types of RFBs, Vanadium Redox Flow Batteries (VRFBs) have gained more attention, and as a result, several physics-based electrochemical models for these systems describing the battery operations have been developed.

Physics-based VRFB models can be classified by dimensions, from zero- to two-dimensional models, as shown in Table 3.1. Models in each category have their own advantages and can be used depending on users' needs. For example, zero-dimensional models have been developed to be easily implementable, enabling to quickly understand, predict, and control the battery system [43-45]. Multi-dimensional models have been implemented by including more detailed physics of the system [46]. As described in Table 3.1, the current trend is to include detailed physical phenomena, such as transport of ions and side reactions of the system [47, 48], and therefore models with more complexities have been built. A zero-dimensional model was developed for batch cell systems including diffusion of vanadium ions through the membrane [49], and this was the first attempt to simulate vanadium ions' crossover through the membrane [49].

The model was further enhanced to include all ions and transport properties of the system [44, 46, 50]. One-dimensional membrane models, which are based on dilute and concentrated solution theories, have been developed [51, 52]. In the one-dimensional membrane models, the membrane region is simplified to one dimension assuming bulk electrolytes at the positive and negative electrodes. Also, VRFB models have been developed in two-dimensions to include diffusion, migration, and convection of all ions and detailed physics of the system [46]. In this dissertation, we study and analyze Vanadium Redox Batch Cell (VRBC) systems at low C-rates with zero-dimensional physics-based models using a systems approach, providing experimental data, models, and codes. There are three objectives:

(i) The first objective is to validate current zero-dimensional models and to formulate a proper zero-dimensional model which can accurately predict capacity loss phenomena of the battery system to maximize the battery usability.

The laboratory-scale batch cell system (*see Figure 3.2*), consisting of a transparent H-cell, a membrane, electrolytes, and electrodes, has been used due to its several advantages over flow cell systems as follows: (a) Coupling the batch cell with zero-dimensional models enables easy and straightforward implementation and mitigates computational challenges to simulate models and estimate their parameters [53]. (b) In this batch system, the effect of ions' crossover through the membrane is dominant at low C-rates. The ions' crossover is one of the main causes of the capacity loss of the redox flow battery systems [46]. Therefore, the capacity loss can be explicitly observed, even for a single cycle in the batch cell system at low C-rates. The study and analysis of the batch cell system based on these low C-rates will be a good starting point to build accurate zero-dimensional models for flow battery systems.

Table 3.1. Selected physics-based electrochemical engineering models of Vanadium redox flow batteries

Model	Ions and molecules included in models									Ions and molecules transport						Gassing side reactions		Thermal effects	Transport theory	Key points	Ref. (Year)
										across electrodes			through the membrane								
	V^{2+}	V^{3+}	VO^{2+}	VO_2^+	H^+	OH^-	HSO_4^-	SO_4^{2-}	H_2O	Diff.	Mig.	Conv.	Diff.	Mig.	Conv.	H_2	O_2				
Zero-dimensional models																					
Shah *et. al.*	O	O	O	O	O	X	X	X	O	N/A: · Zero-dimensional models assume that bulk electrolyte transport happens across the membrane from positive to negative electrolytes or from negative to positive electrolytes · There are more detailed physics in real systems, but zero-dimensional models are important for control and prediction for long cycles			X H^+: No constraints for transport H_2O: Osmotic drag	X	X	X	X	Isothermal	N/A	· Allowed only H^+ and H_2O crossover through the membrane	[43] (2011)
Tang *et. al.*	O	O	O	O	X	X	X	X	X				O (Includes only V^{2+}, V^{3+}, VO^{2+}, and VO_2^+)	X	X	O Used current efficiency (not equations)	O	Isothermal	Dilute solution	· Demonstrated the batch cell model	[49] (2011)
Tang *et. al*	O	O	O	O	X	X	X	X	X				O (Includes only V^{2+}, V^{3+}, VO^{2+}, and VO_2^+)	X	X	X	X	Thermal	Dilute solution	· Coupled thermal effects with mass balance equations	[53] (2012)
Boettcher *et. al.*	O	O	O	O	O	X	O	O	O				O (All ions except for OH^-, and SO_4^{2-})	O	O	X	X	Isothermal	Dilute solution	· Limitation is uni-directional flux for Mig. and Conv.	[44] (2016)
Pugach *et. al.*	O	O	O	O	X	X	X	X	X				O (Includes only V^{2+}, V^{3+}, VO^{2+}, and VO_2^+)	O	O	X	X	Isothermal	Dilute solution	· Analytical solution for ions crossover including full directional flux	[45] (2018)
One-dimensional models (assuming bulk electrolytes at positive and negative)																					
Gandomi *et. al.*	X	X	X	X	O	X	O	X	O	N/A: One-dimensional membrane models assume positive and negative electrolytes have bulk electrolyte transport			O (Includes only H^+, HSO_4^-, and H_2O)	O	O	X	X	Isothermal	Concentrated solution	· Assumed that only H^+, HSO_4^-, and H_2O can cross the membrane	[51] (2014)
Lei *et. al.*	O	O	O	O	O	X	O	X	X				O (All ions except for SO_4^{2-}, OH^- and H_2O)	O	O	X	X	Isothermal	Dilute solution	· Included Donnan effects	[52] (2015)
Two-dimensional models																					
Shah *et. al.*	O	O	O	O	O	X	O	O	O	O (Includes only V^{2+}, V^{3+}, VO^{2+}, and VO_2^+)	O	O	O (Includes only H^+, HSO_4^-, and H_2O)	O	O	O	X	Isothermal	Dilute solution	No vanadium ions crossover through the membrane and side reactions of the same	[47] (2010)
Al-Fetlawi *et. al.*	O	O	O	O	O	X	O	O	O	O (Includes only V^{2+}, V^{3+}, VO^{2+}, and VO_2^+)	O	O	O (Includes only H^+, HSO_4^-, and H_2O)	O	O	X	O	Thermal	Dilute solution		[48] (2009)
Knehr *et. al.*	O	O	O	O	O	X	O	O	O	O (All ions except for SO_4^{2-}, and OH^-)	O	O	O	O	O	X	X	Isothermal	Dilute solution	Improved OCV and Donnan potential	[46] (2012)

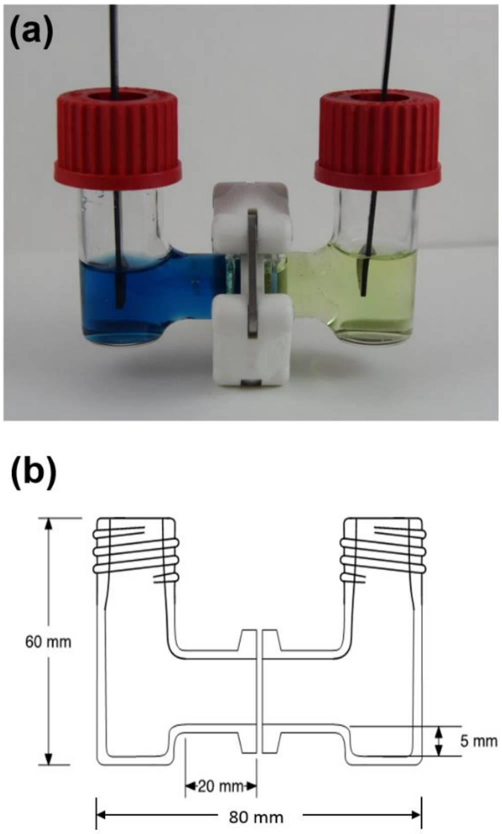

Figure 3.2. Schematic of the laboratory-scale VRBC system. (a) An actual image of the system for a discharge state. The blue electrolyte represents VO^{2+} (positive) and the green electroltye represents V^{3+} (negative). (b) Specification of the system. The batch cell system has advantages of being easy and simple to implement and a quick understanding of the performance of the RFBs. Coupling with electrochemical engineering models for the VRBC system helps modelers estimate parameters and analyze cell performance efficiently.

(ii) The second objective is to show that a systems approach that simultaneously estimates multiple parameters of the model allows users to quickly understand the battery system. For example, estimation of all the parameters of the physics-based model for the VRBC system has been addressed using two cell systems, which include two different membranes, assuming that both systems have some common characteristics, such as kinetics at the electrodes, the formal potential, and the cell resistance excluding the membrane resistance (*see Figure 3.3*).

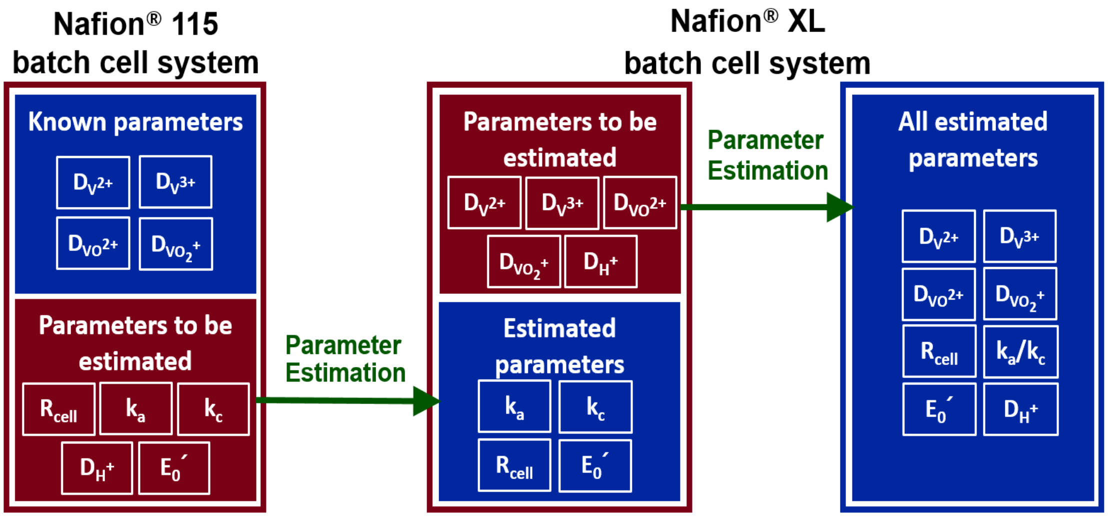

Figure 3.3. Parameter estimation of the batch cell system with charging/ discharging curves at different C-rates. We show a way of estimating all parameters in a model, which can help analyze and study the performance of the cell system.

First, a reference Nafion® 115 membrane is used. As diffusion coefficients of vanadium ions for a Nafion® 115 membrane are available in the literature, this information is utilized to estimate other cell system parameters, such as rate constants at the electrodes, the formal potential, and the cell resistance excluding the membrane resistance in the batch cell model. Next, the systems approach shows that diffusion coefficients of vanadium ions for other membranes can also be estimated based on the parameters estimated using the Nafion® 115 system. Using this concept, four vanadium ions' diffusion coefficients of a Nafion® XL membrane, which are not available in the literature, have been estimated. Once the parameters have been obtained, one can use the kinetic and transport parameters for simulating redox battery systems as well. The systems approach can be used to update the transport and kinetic parameters or any degradation inputs of redox batteries within a very short span of time during battery operation. Any mismatch between model and data over cycles of operation can be resolved with the updated parameters, and the control of the redox batteries with precise predictions based on the proposed work might lead to

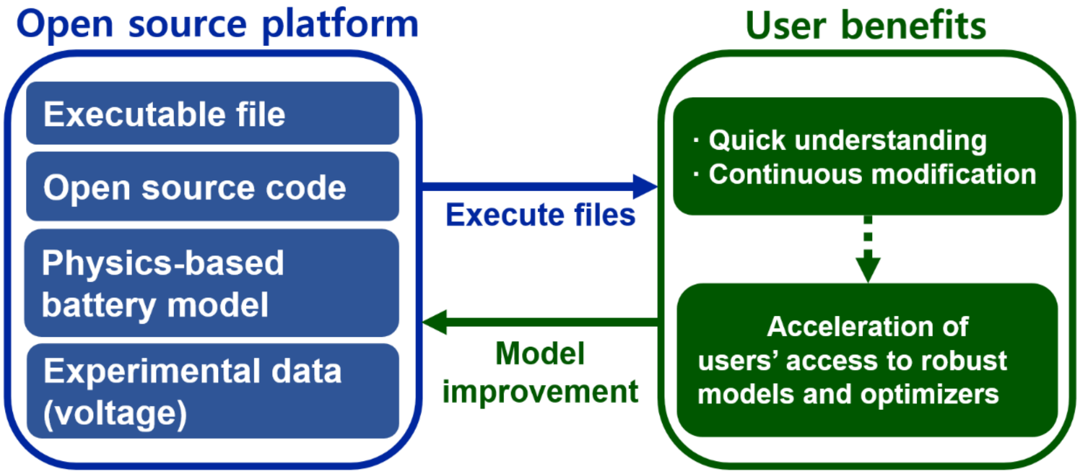

Figure 3.4. Open source platfrom and user benefit. Different models and optimizers describing the same systems produce different estimated parameters. On the open source platform, users can improve the model through continuous modification and easy access, and this accelerates to identify proper and robust models and optimizers for redox battery systems.

longer battery life and lower battery cost. While an ideal situation in simulations of physics-based battery models is to obtain proper parameters from independent experiments, many of experiments require either physical destruction of the battery or sophisticated experimental setup [54-56]. For example, dialysis cell, pumps, and measuring cylinders are utilized to investigate diffusion coefficients of ions through a membrane in an RFB experimental setup [57]. Techniques such as linear sweep voltammetry and electrochemical impedance spectroscopy were used to investigate reaction rate information for the kinetic parameters at electrodes [58, 59]. Therefore, parameter estimation from a systems approach and experiments is complementary, and the proper implementation of two approaches enhances the accuracy of parameter estimation and quick understanding of the system.

(iii) The last objective is to accelerate people's access to robust models and optimization approaches by providing an open source platform. In the open source platform, users can utilize experimental data, models, and codes for parameter estimation of the batch cell system for redox flow batteries at one place *(see Figure 3.4)*. For example, even though a systems approach helps users to understand the battery system faster, there are some critical issues with redox flow battery simulations; (a) Different models and optimizers describing the same systems provide different values of the estimated parameters (b) There is a time-delay for users to adopt approaches because most of the literature just provide the approaches as a paper. The open source platform will help to arrive at robust modeling and optimization approaches for users by continuous modification of battery models with detailed physics, additional experimental data, and different optimizers. Also, the platform enables to identify the performance of redox batteries without the need for software installation and a priori programming knowledge. These advantages of the open source platform will help accelerate the spread of redox flow battery systems.

3.2 EXPERIMENTAL

3.2.1 *Materials*

Vanadium (IV) oxide sulfate hydrate ($VOSO_4 \cdot xH_2O$)[31] and an aqueous sulfuric acid solution (H_2SO_4)[32] were purchased from Sigma Aldrich and used as received. Nafion® XL[60] and Nafion® 115[61] membranes were purchased from DuPont and used after pretreatment using distilled deionized water (DDW) and an aqueous sulfuric acid solution at 80 °C for 30 minutes, respectively. Graphite electrodes [36] were purchased from Saturn Industries.

3.2.2 *Instrument*

The performance of the batch cell was obtained at different C-rates, using a Solartron SI 1287 potentiostat [27].

3.2.3 *The batch cell system*

The H-cell (Adams and Chittenden Scientific Glass) [37] consists of a positive and a negative chamber, as shown in Figure 3.2. A membrane in contact with the electrolytes of the half-cell is located between these two chambers. The volume of the electrolytes at the positive and negative chamber is 10 ml each. Two graphite electrodes with specific reaction surface (1 cm × 1 cm × 0.1 cm) are vertically placed in the center of each chamber and fixed with the plastic caps of the H-cell. There are rubber gaskets inside these plastic caps and silicon is attached to the gaps between the electrode and the gasket to prevent oxygen leakages from outside the system.

3.2.4 *Preparation of electrolytes*

Sulfuric acid solution (H_2SO_4, 6.73 ml) was slowly added to 7.5 ml of DDW, and the final volume was adjusted to 30 mL using DDW to prepare 4M sulfuric acid solution (H_2SO_4). 0.603 g of vanadium (IV) oxide sulfate hydrate ($VOSO_4 \cdot xH_2O$) was added very slowly and stirred at 60 °C for 1 hour. The hydration of the vanadium oxide sulfate ($VOSO_4$) was determined by Karl Fischer titration using a Mettler Toledo C20 Coulometric KF Titrator with a DO308 oven attachment [46]. The instrument was located inside a dry room, where the dew point is maintained at -64°F. Karl Fisher showed two water molecules were hydrated to one vanadium oxide sulfate ($VOSO_4 \cdot 2H_2O$), and the molecular weight (201.042 g/mol) was calculated based on the indication. 30 mL of 0.1M vanadium (IV) oxide sulfate ($VOSO_4$) in an aqueous 4M sulfuric acid solution (H_2SO_4) was prepared. Next, 10 mL of 0.1M vanadium (IV) oxide sulfate ($VOSO_4$) in an aqueous 4M sulfuric acid solution (H_2SO_4) was added to the positive and negative chambers, respectively. The batch cell system was slowly charged at C/20 rate to convert VO^{2+} to V^{3+} at the anode and VO^{2+} to VO_2^+ at the cathode. When the upper limit voltage of 1.7V was exceeded, the charge was set to be terminated, and 93.9% V^{3+}/6.1% VO^{2+} electrolytes at the negative chamber were achieved by the coulombic calculation. After that, VO^{2+}/VO_2^+ electrolytes at the positive chamber were drained and refilled with a new 10 mL of 0.1 M VO^{2+} in 4M sulfuric acid solution (H_2SO_4).

3.2.5 *Cell operation*

Both Nafion® 115 and Nafion® XL systems are operated at low C-rates (~ C/30). In an ideal situation, a C-rate of 1C means the applied current when the battery is charged for one hour. For batch cell operation, 1C was calculated by a mass balance equation as below:

$$1C = \frac{F \cdot C_{VOSO_4} \cdot V_r}{1hr} \tag{3.A}$$

where F is the Faraday constant (= 26801 Ah/mol), C_{VOSO4} is the concentration of vanadium (IV) oxide sulfate (= 0.1 mol/L), and V_r presents the volume of electrolytes (=10 mL). Therefore, 1C was derived as 26.8 mA, and C/20 and C/30 were calculated as 1.34 mA, 0.89 mA, respectively. For the Nafion® 115 system**,** a typical CC-CV profile (CC: Constant Current, CV: Constant Voltage) was applied (maximum voltage: 1.7V). Once the batch cell voltage reached 1.7V, it was charged with the CV until the applied current is saturated. In other words, CV charging is continued until the exponentially decaying applied current stopped decreasing. For discharging, a CC profile was applied. The CC-CV profile was used to analyze the cell system's performance at different C-rates (C/20 and C/30), making the cell to reach full capacity. The coulombic efficiency of the Nafion® 115 system is 0.73 at C/30 and 0.81 at C/20 (*see experimental data in Figure 3.8 and 11*). It shows that the higher current rates give the higher coulombic efficiency [62]. For the Nafion® XL cell system, a CC profile was applied to the batch cell system during the charging and discharging process. The temperature of the H-cell was maintained at 25°C in a Tenney Environmental Chamber [28]. The gas washer, which was filled with water and connected to the argon line and cell system, minimizes evaporation of electrolytes. During the charging and discharging process, a magnetic stirrer was used to make uniform concentrations of the electrolyte in the positive and negative chambers.

3.3 MODEL FORMULATION

Various zero-dimensional VRFB models accounting for ion transport phenomena, such as diffusion, migration, and convection, have been developed. In this section, several important zero-dimensional models are validated, using voltage outputs obtained from the batch cell systems equipped with a Nafion® 115 membrane at C/30. First, the diffusion model for a batch cell system demonstrated by A. Tang *et al.* is validated. In this diffusion model, the proton transport is removed from governing equations, and the formal potential is used, which combines a standard potential, proton concentration, and ions activity coefficients. Second, the concept of uni-directional ions migration and convection with the same direction of ions diffusion, which was proposed by P. A. Boettcher *et al.* in 2016 [44], is added to the diffusion model and validated. Third, the anti-directional ions flux is added to the uni-direction model and validated. The zero-dimensional model including both uni- and anti-directional ion's migration and convection was proposed by M. Pugach *et al.* in 2018 [45]. Lastly, the proton concentration is separated from the formal potential and its transport is added to the full-direction model to formulate an adequate zero-dimensional physics-based model for a systems approach. Ideally, parameters should be estimated from one set of data, and the same set of estimating parameters is used to fit another set of data. However, if the formal potential includes the proton concentration, the formal potential should be estimated for every other C-rate because the proton concentration depends on applied C-rates. This is not an efficient system approach.

In the model formulation process, simultaneous estimation of multiple parameters, called a systems approach, has been carried out using experimental voltage profiles of charging and discharging protocols for the first cycle (CC-CV charging and CC discharging at C/30). The model parameters are fitted with the experimental data to estimate their values using mathematical optimization techniques. 200 (=*N*) data points for charge and discharge voltage were collected at regular time intervals. The optimization routine finds the optimal values for which the objective function (as given in equation 3.B) subject to the model equations, initial conditions, and bounds for the parameters, is minimized. Using realistic values of these parameters as initial guesses, the model can be simulated to predict the values of voltage at certain time intervals. The final estimated parameters are obtained by solving an optimization problem where the sum of squares of the differences in the voltage outputs between the model and experiment divided by the total number of experimental data points (known as the Mean Square Error, MSE) for the first cycle (charging and discharging) of the system is minimized, and unknown parameters are used as decision variables [63]. The objective function of the optimization approach can be expressed as follows [64]:

$$\begin{gathered}\mathrm{Min}\,\frac{1}{\mathrm{N}-\mathrm{n}_{\mathbf{p}}}\sum_{j=1}^{N}\left[\mathrm{V}_{\exp,j}-\mathrm{V}_{\mathrm{model},j}(\mathbf{p})\right]^{2}\\ \mathrm{s.t.}\ \mathbf{p}^{\mathrm{L}}\le\mathbf{p}\le\mathbf{p}^{\mathrm{U}}\end{gathered}\tag{3.B}$$

where N is the total number of experimental data points for charging and discharging, n_p is the number of estimating parameters, $V_{exp,\,j}$ and $V_{model,\,j}$ ($\mathbf{p}$) indicate the experimental and model predicted voltage value of the batch cell for the j^{th} data point, $\mathbf{p}$ is the vector of the estimating parameters, and $\mathbf{p}^{\mathbf{L}}$ and $\mathbf{p}^{\mathbf{U}}$ represent the lower and upper bounds for the vector of the estimating parameters ($\mathbf{p}$). The trial-and-error method has been utilized to obtain initial guesses and

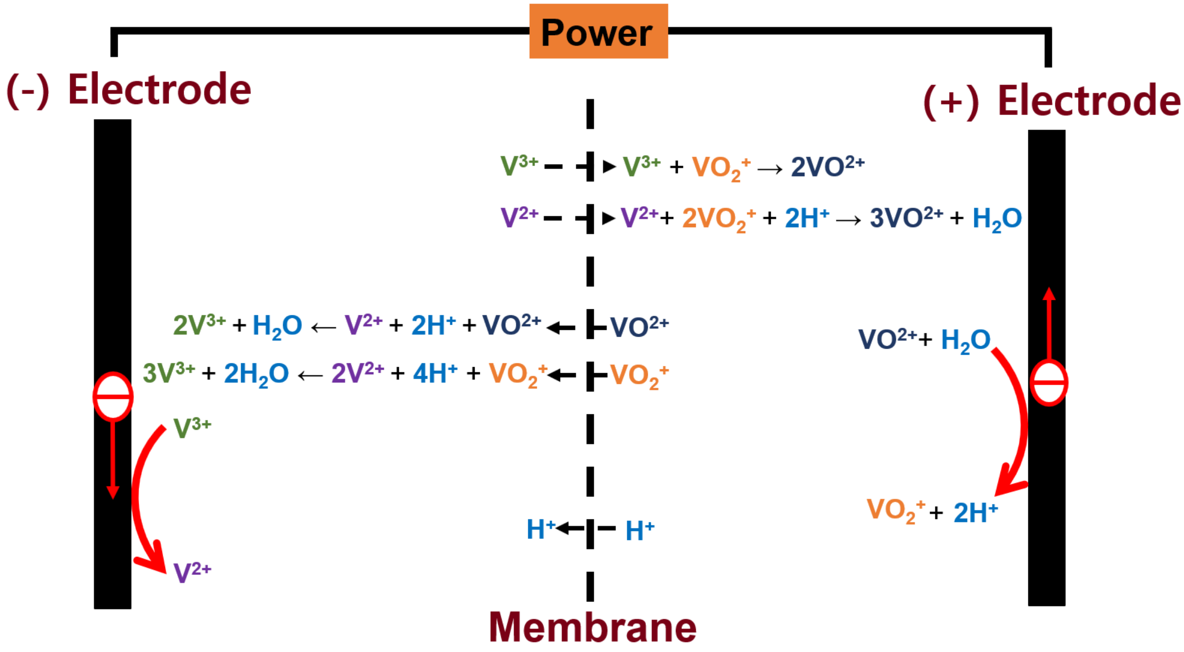

Figure 3.5. Side reactions caused by crossover of vanadium ions through the membrane durging charging. One mole of V^{2+}, which moves across the membrane from the negative electrolyte, reacts with two moles of VO_2^+ in the positive electrolytes producing three moles of VO^{2+}. One mole of V^{3+} crossover from the negative electrolyte causes a chemical reaction with one mole of VO_2^+ producing two moles of VO^{2+} in the positive electrolyte. Similarly, in the negative electrolyte, two moles of V^{3+} are produced by a chemical reaction between one mole of V^{2+} and one mole of VO^{2+}, which moves from the positive electrolyte, and three moles of V^{3+} are produced by a chemical reaction between two moles of V^{2+} and one mole of VO_2^+, which moves from the positive electrolyte.

lower/upper bounds in this optimization problem [65]. Initial guesses were set up based on the physical characteristics of the batch system, and lower and upper bounds were adjusted based on the initial guesses (up to 20% from initial guesses for most cases) to obtain converged values of the unknown parameters and identify minimized MSE. Analysis and studies of simulations and optimizations in this work were carried out on a workstation with dual 8-core, 3.10 GHz Intel Xeon processors, 32.0 GB RAM using the NLPsolve [44] in the optimization package of the Maple® software [66].

3.3.1 *Model 1: Diffusion model*

The diffusion model includes the crossover of the vanadium ions through the membrane by diffusion and the ions' side reactions in the electrolyte, as shown in Figure 3.5 [49]. Once vanadium ions cross the membrane, reactions between two different vanadium ions occur, producing VO^{2+} ions at the positive electrolyte and V^{3+} ions at the negative electrolyte, and this, in turn, causes the capacity loss of the battery [49].

3.3.1.1 Assumptions

The following assumptions were made in the diffusion model for the batch cell system: (i) Side reactions between two different vanadium ions, due to the crossover of ions through the membrane, occur immediately the vanadium ions cross the membrane [46]; (ii) Since the gas washer is connected to the batch cell system to minimize evaporation of the electrolyte, evaporation of the electrolyte is ignored in the model; (iii) Faraday's law of electrolysis has been assumed to estimate the rate of reactions of vanadium ions at the cathode and anode; (iv) Hydrogen and oxygen that evolve at the electrode during charging and discharging, are ignored [47, 48]; (v) No side reactions take place between other vanadium ions inside the membrane; (vi) The sulfuric acid (H_2SO_4) completely dissociates into protons and sulfate ions (SO_4^{2-}); (vii) Activity coefficients of vanadium ionic species are not equal to 1, and the proton concentration is not accurately known due to several ionic equilibria in the electrolytes [49].

3.3.1.2 Governing equations

Accumulation, generation, and diffusion terms of Equations 3.1 to 3.4 (or 3.1´~ 3.4´) and 3.5~3.8 (or 3.5´~ 3.8´) in Tables 3.2 and 3.3 are used in the diffusion model [44, 49]. Table 3.2 and 3.3

include dynamics of concentrations for vanadium ions during charging and discharging, respectively. In the diffusion model, the only difference between governing equations of charging and discharging is the direction of the applied current because the model does not include migration and convection terms. In Tables 3.2 and 3.3, mass balance equations, consisting of the rate of accumulation of ions, the rate of ions entering the opposite chamber, the rate of ions flowing out from their own chamber, and the rate of loss or generation of ions, were established for vanadium ions. For example, the rate of accumulation of each vanadium ion species (V^{2+}, V^{3+}, VO^{2+}, and VO_2^{+}) is the sum of the rate of production of the vanadium ions by side reactions, the rate of outflow into the opposite chamber, and the rate of generation or loss at the electrode by the electrochemical reactions [67].

3.3.1.3 Additional equations

Equations 3.9-1, 3.10-1, and 3.11 are used in the diffusion model in Table 3.4. The cell voltage, the open circuit voltage, and the overpotential are used in the model [43, 44, 49]. Also, kinetics at the positive and negative electrode is added to the original diffusion model to study the system more details. The cell voltage is given by Equation 3.9-1 [49], and the open circuit voltage is expressed as Equation 3.10-1. In the open circuit voltage, the formal potential is used, extracting activity coefficients and proton concentrations from the logarithmic term, following the assumption (vii) [49]. The overpotential at the positive and negative electrodes, including the activation barrier, is calculated as given in Equations 3.11, and a charge transfer coefficient of 0.5 is applied to the overpotential [43]. All relevant variables and parameters, which were used to the model and simulate the batch system, are listed in Tables 3.5 and 3.6, respectively.

Table 3.2. Governing equations (charging process)

Accum.	**= Gen.**	**+ In – Out**		**No.**
		(Diffusion term)	**(Migration and electro-osmotic convection term)**	
Uni-directional model				
$V_r \dfrac{dC_{V^{2+}}(t)}{dt}$	$= + \dfrac{i_{app}}{F}$	$-\left(D_{V^{2+}}C_{V^{2+}}(t)+2D_{VO_2^+}C_{VO_2^+}(t)+D_{VO^{2+}}C_{VO^{2+}}(t)\right)\dfrac{A_m}{d_m}$	$-2\left(D_{VO^{2+}}C_{VO^{2+}}(t)+D_{VO_2^+}C_{VO_2^+}(t)\right)\dfrac{F}{RT}A_m\nabla\phi-\left(C_{VO^{2+}}(t)+2C_{VO_2^+}(t)\right)v_mA_m$	**[3.1]**
$V_r \dfrac{dC_{V^{3+}}(t)}{dt}$	$= - \dfrac{i_{app}}{F}$	$-\left(D_{V^{3+}}C_{V^{3+}}(t)-3D_{VO_2^+}C_{VO_2^+}(t)-2D_{VO^{2+}}C_{VO^{2+}}(t)\right)\dfrac{A_m}{d_m}$	$+\left(4D_{VO^{2+}}C_{VO^{2+}}(t)+3D_{VO_2^+}C_{VO_2^+}(t)\right)\dfrac{F}{RT}A_m\nabla\phi+\left(2C_{VO^{2+}}(t)+3C_{VO_2^+}(t)\right)v_mA_m$	**[3.2]**
$V_r \dfrac{dC_{VO^{2+}}(t)}{dt}$	$= - \dfrac{i_{app}}{F}$	$-\left(D_{VO^{2+}}C_{VO^{2+}}(t)-3D_{V^{2+}}C_{V^{2+}}(t)-2D_{V^{3+}}C_{V^{3+}}(t)\right)\dfrac{A_m}{d_m}$	$-2D_{VO^{2+}}C_{VO^{2+}}(t)\dfrac{F}{RT}A_m\nabla\phi-2v_mA_mC_{VO^{2+}}(t)$	**[3.3]**
$V_r \dfrac{dC_{VO_2^+}(t)}{dt}$	$= + \dfrac{i_{app}}{F}$	$-\left(D_{VO_2^+}C_{VO_2^+}(t)+2D_{V^{2+}}C_{V^{2+}}(t)+D_{V^{3+}}C_{V^{3+}}(t)\right)\dfrac{A_m}{d_m}$	$-D_{VO_2^+}C_{VO_2^+}(t)\dfrac{F}{RT}A_m\nabla\phi-v_mA_mC_{VO_2^+}(t)$	**[3.4]**
Full directional model				
$V_r \dfrac{dC_{V^{2+}}(t)}{dt}$	$= + \dfrac{i_{app}}{F}$	$-\left(D_{V^{2+}}C_{V^{2+}}(t)+2D_{VO_2^+}C_{VO_2^+}(t)+D_{VO^{2+}}C_{VO^{2+}}(t)\right)\dfrac{A_m}{d_m}$	$-2\left(D_{VO^{2+}}C_{VO^{2+}}(t)+D_{VO_2^+}C_{VO_2^+}(t)-D_{V^{2+}}C_{V^{2+}}(t)\right)\dfrac{F}{RT}A_{mem}\nabla\phi-\left(C_{VO^{2+}}(t)+2C_{VO_2^+}(t)-C_{V^{2+}}(t)\right)v_mA_m$	**[3.1´]**
$V_r \dfrac{dC_{V^{3+}}(t)}{dt}$	$= - \dfrac{i_{app}}{F}$	$-\left(D_{V^{3+}}C_{V^{3+}}(t)-3D_{VO_2^+}C_{VO_2^+}(t)-2D_{VO^{2+}}C_{VO^{2+}}(t)\right)\dfrac{A_m}{d_m}$	$+\left(4D_{VO^{2+}}C_{VO^{2+}}(t)+3D_{VO_2^+}C_{VO_2^+}(t)+3D_{V^{3+}}C_{V^{3+}}(t)\right)\dfrac{F}{RT}A_{mem}\nabla\phi+\left(2C_{VO^{2+}}(t)+3C_{VO_2^+}(t)+C_{V^{3+}}(t)\right)v_mA_m$	**[3.2´]**
$V_r \dfrac{dC_{VO^{2+}}(t)}{dt}$	$= - \dfrac{i_{app}}{F}$	$-\left(D_{VO^{2+}}C_{VO^{2+}}(t)-3D_{V^{2+}}C_{V^{2+}}(t)-2D_{V^{3+}}C_{V^{3+}}(t)\right)\dfrac{A_m}{d_m}$	$-2\left(D_{VO^{2+}}C_{VO^{2+}}(t)+3D_{V^{2+}}C_{V^{2+}}(t)+3D_{V^{3+}}C_{V^{3+}}(t)\right)\dfrac{F}{RT}A_{mem}\nabla\phi-\left(C_{VO^{2+}}(t)+3C_{V^{2+}}(t)+2C_{V^{3+}}(t)\right)v_mA_m$	**[3.3´]**
$V_r \dfrac{dC_{VO_2^+}(t)}{dt}$	$= + \dfrac{i_{app}}{F}$	$-\left(D_{VO_2^+}C_{VO_2^+}(t)+2D_{V^{2+}}C_{V^{2+}}(t)+D_{V^{3+}}C_{V^{3+}}(t)\right)\dfrac{A_m}{d_m}$	$-\left(D_{VO_2^+}C_{VO_2^+}(t)-4D_{V^{2+}}C_{V^{2+}}(t)-3D_{V^{3+}}C_{V^{3+}}(t)\right)\dfrac{F}{RT}A_{mem}\nabla\phi-\left(C_{VO_2^+}(t)-2C_{V^{2+}}(t)-C_{V^{3+}}(t)\right)v_mA_m$	**[3.4´]**

Table 3.3. Governing equations (discharging process)

Accum.	= Gen.	+In – Out		
		(Diffusion terms)	**(Migration and electro-osmotic convection terms)**	**No.**
Uni-directional model				
$V_r \frac{dC_{V^{2+}}(t)}{dt}$	$= -\frac{i_{app}}{F}$	$-\left(D_{V^{2+}}C_{V^{2+}}(t)+2D_{VO_2^+}C_{VO_2^+}(t)+D_{VO^{2+}}C_{VO^{2+}}(t)\right)\frac{A_m}{d_m}$	$-2D_{V^{2+}}C_{V^{2+}}(t)\frac{F}{RT}\frac{\Delta\phi(t)}{d_m}A_m - v_m C_{V^{2+}}(t)A_m$	**[3.5]**
$V_r \frac{dC_{V^{3+}}(t)}{dt}$	$= +\frac{i_{app}}{F}$	$-\left(D_{V^{3+}}C_{V^{3+}}(t)-3D_{VO_2^+}C_{VO_2^+}(t)-2D_{VO^{2+}}C_{VO^{2+}}(t)\right)\frac{A_m}{d_m}$	$-3D_{V^{3+}}C_{V^{3+}}(t)\frac{F}{RT}\frac{\Delta\phi(t)}{d_m}A_m - v_m C_{V^{3+}}(t)A_m$	**[3.6]**
$V_r \frac{dC_{VO^{2+}}(t)}{dt}$	$= +\frac{i_{app}}{F}$	$-\left(D_{VO^{2+}}C_{VO^{2+}}(t)-3D_{V^{2+}}C_{V^{2+}}(t)-2D_{V^{3+}}C_{V^{3+}}(t)\right)\frac{A_m}{d_m}$	$+6\left(D_{V^{2+}}C_{V^{2+}}(t)+D_{V^{3+}}C_{V^{3+}}(t)\right)\frac{F}{RT}\frac{\Delta\phi(t)}{d_m}A_m+\left(3C_{V^{2+}}(t)+2C_{V^{3+}}(t)\right)v_m A_m$	**[3.7]**
$V_r \frac{dC_{VO_2^+}(t)}{dt}$	$= -\frac{i_{app}}{F}$	$-\left(D_{VO_2^+}C_{VO_2^+}(t)+2D_{V^{2+}}C_{V^{2+}}(t)+D_{V^{3+}}C_{V^{3+}}(t)\right)\frac{A_m}{d_m}$	$-\left(4D_{V^{2+}}C_{V^{2+}}(t)+3D_{V^{3+}}C_{V^{3+}}(t)\right)\frac{F}{RT}\frac{\Delta\phi(t)}{d_m}A_m-\left(2C_{V^{2+}}(t)+C_{V^{3+}}(t)\right)v_m A_m$	**[3.8]**
Full directional model				
$V_r \frac{dC_{V^{2+}}(t)}{dt}$	$= -\frac{i_{app}}{F}$	$-\left(D_{V^{2+}}C_{V^{2+}}(t)+2D_{VO_2^+}C_{VO_2^+}(t)+D_{VO^{2+}}C_{VO^{2+}}(t)\right)\frac{A_m}{d_m}$	$-2\left(D_{V^{2+}}C_{V^{2+}}(t)-D_{VO^{2+}}C_{VO^{2+}}(t)-D_{VO_2^+}C_{VO_2^+}(t)\right)\frac{F}{RT}A_m\nabla\phi-\left(C_{V^{2+}}(t)-C_{VO^{2+}}(t)-2C_{VO_2^+}(t)\right)v_m A_m$	**[3.5′]**
$V_r \frac{dC_{V^{3+}}(t)}{dt}$	$= +\frac{i_{app}}{F}$	$-\left(D_{V^{3+}}C_{V^{3+}}(t)-3D_{VO_2^+}C_{VO_2^+}(t)-2D_{VO^{2+}}C_{VO^{2+}}(t)\right)\frac{A_m}{d_m}$	$-\left(3D_{V^{3+}}C_{V^{3+}}(t)+4D_{VO^{2+}}C_{VO^{2+}}(t)+3D_{VO_2^+}C_{VO_2^+}(t)\right)\frac{F}{RT}A_m\nabla\phi-\left(C_{V^{3+}}(t)+2C_{VO^{2+}}(t)+3C_{VO_2^+}(t)\right)v_m A_m$	**[3.6′]**
$V_r \frac{dC_{VO^{2+}}(t)}{dt}$	$= +\frac{i_{app}}{F}$	$-\left(D_{VO^{2+}}C_{VO^{2+}}(t)-3D_{V^{2+}}C_{V^{2+}}(t)-2D_{V^{3+}}C_{V^{3+}}(t)\right)\frac{A_m}{d_m}$	$+2\left(3D_{V^{2+}}C_{V^{2+}}(t)+3D_{V^{3+}}C_{V^{3+}}(t)+D_{VO^{2+}}C_{VO^{2+}}(t)\right)\frac{F}{RT}A_m\nabla\phi+\left(3C_{V^{2+}}(t)+2C_{V^{3+}}(t)+C_{VO^{2+}}(t)\right)v_m A_m$	**[3.7′]**
$V_r \frac{dC_{VO_2^+}(t)}{dt}$	$= -\frac{i_{app}}{F}$	$-\left(D_{VO_2^+}C_{VO_2^+}(t)+2D_{V^{2+}}C_{V^{2+}}(t)+D_{V^{3+}}C_{V^{3+}}(t)\right)\frac{A_m}{d_m}$	$-\left(4D_{V^{2+}}C_{V^{2+}}(t)+3D_{V^{3+}}C_{V^{3+}}(t)-D_{VO_2^+}C_{VO_2^+}(t)\right)\frac{F}{RT}A_m\nabla\phi-\left(2C_{V^{2+}}(t)+C_{V^{3+}}(t)-C_{VO_2^+}(t)\right)v_m A_m$	**[3.8′]**

Table 3.4. Other equations of all-Vanadium redox batch batteries

	No.
$E_{cell}(t) = E_{cell}^{rev}(t) - i_{app} R_{cell,total} + \eta_2(t) - \eta_1(t)$	[3.9-1]
$E_{cell}(t) = E_{cell}^{rev}(t) + i_{app} R_{cell-mem} + i_{app} \dfrac{d_m}{A_m \sigma_m} + \eta_2(t) - \eta_1(t)$	[3.9-2]
$E_{cell}^{rev}(t) = E_0^{'} + \dfrac{RT}{F} \ln\left(\dfrac{C_{V^{2+}}(t) C_{VO_2^+}(t)}{C_{V^{3+}}(t) C_{VO^{2+}}(t)} \right)$	[3.10-1]
$E_{cell}^{rev}(t) = E_0^{'} + \dfrac{RT}{F} \ln\left(\dfrac{C_{V^{2+}}(t) C_{VO_2^+}(t) C_{H_p^+}(t)^2}{C_{V^{3+}}(t) C_{VO^{2+}}(t)} \right)$	[3.10-2]
$\eta_1(t) = -\dfrac{2RT}{F} \arcsin\left(\dfrac{i_{app}}{2Fk_a \sqrt{C_{V^{3+}}(t) C_{V^{2+}}(t)}} \right), \eta_2(t) = \dfrac{2RT}{F} \arcsin\left(\dfrac{i_{app}}{2Fk_c \sqrt{C_{VO^{2+}}(t) C_{VO_2^+}(t)}} \right)$	[3.11]
$v_{mem} = \dfrac{\kappa c_f F}{u_w A_m \sigma_m} i_{app}$	[3.12]
$\nabla \phi = \dfrac{i_{app}}{A_m \sigma_m}$	[3.13]
$\sigma_m = \dfrac{F^2}{RT} \sum_i z_i^2 C_i(t) D_i \approx \dfrac{F^2}{RT} \left(C_{H_p^+}(t) + C_{H_n^+}(t) \right) D_{H^+}$	[3.14]

Table 3.5. Variables of all-Vanadium redox batch cell systems

Symbol	Variable	Units
$C_{V^{2+}}(t)$	Concentration of Vanadium (II)	mol m^{-3}
$C_{V^{3+}}(t)$	Concentration of Vanadium (III)	mol m^{-3}
$C_{VO^{2+}}(t)$	Concentration of Vanadium (IV)	mol m^{-3}
$C_{VO_2^+}(t)$	Concentration of Vanadium (V)	mol m^{-3}
$C_{H_p^+}(t)$	Concentration of Proton in Positive Electrolytes	mol m^{-3}
$C_{H_n^+}(t)$	Concentration of Proton in Negative Electrolytes	mol m^{-3}
$E_{cell}(t)$	Cell voltage	V
$E_{cell}^{rev}(t)$	Open circuit voltage	V
$\eta_1(t)$	Overpotential at anode	V
$\eta_2(t)$	Overpotential at cathode	V

Table 3.6. Parameters of all-Vanadium redox batch cell system used in Simulations

Symbol	Parameter	Values	Units
Geometrical parameters			
d_m	Thickness of membrane - Nafion® 115	127×10^{-6}	m
	- Nafion® XL	27.5×10^{-6}	
A_m	Cross sectional area of the membrane	1.77×10^{-4}	m^2
A_e	Surface area of the electrode for reaction	2.3×10^{-4}	m^2
V_r	Volume of electrolyte	10^{-5}	m^3
T	Temperature	298	K
Operational parameters			
i_{app}	Applied Current	C/20: 1.34×10^{-3} C/30: 0.89×10^{-3}	A
j_{app}	Current density	C/20: 5.83 C/20: 3.87	A m^{-2}
Parameters collected from the literature			
F	Faraday constant	96485.34	s A mol^{-1}
R	Ideal gas constant	8.314	J K^{-1} mol^{-1}
κ	Electro-kinetic permeability of membrane	1.95×10^{-19}	m^2
c_f	Concentration of fixed-charge in membrane	1900	mol m^{-3}
u_w	Water viscosity	8.9×10^{-4}	Pa s
$D_{V^{2+}}$	V^{2+} diffusion coefficient of Nafion® 115	0.88×10^{-11}	m^2 s^{-1}
$D_{V^{3+}}$	V^{3+} diffusion coefficient of Nafion® 115	0.32×10^{-11}	m^2 s^{-1}
$D_{VO^{2+}}$	VO^{2+} diffusion coefficient of Nafion® 115	0.68×10^{-11}	m^2 s^{-1}
$D_{VO_2^+}$	VO_2^+ diffusion coefficient of Nafion® 115	0.59×10^{-11}	m^2 s^{-1}
Initial concentration			
$C^0_{V^{2+}}$	Initial concentration of V^{2+} ions	0.001	mol m^{-3}
$C^0_{V^{3+}}$	Initial concentration of V^{3+} ions	93.9	mol m^{-3}
$C^0_{VO^{2+}}$	Initial concentration of VO^{2+} ions	99.999	mol m^{-3}
$C^0_{VO_2^+}$	Initial concentration of VO_2^+ ions	0.001	mol m^{-3}
$C^0_{H_p^+}$	Initial concentration of protons at the positive electrolytes	8000	mol m^{-3}
$C^0_{H_n^+}$	Initial concentration of protons at the negative electrolytes	8000	mol m^{-3}

3.3.1.4 Parameter estimation

There are four parameters to be estimated; the rate constants at the positive and negative electrodes, the cell resistance, and the formal potential. For the best performance of the optimization problem, the rate constants are expressed in term of an exponential function ($k_c=e^{-A}$ and $k_c=e^{-B}$), and indices (A and B) of the exponential function are used as optimizing variables because the original parameters of the rate constants are too small (~10^{-10}) to identify properly.

3.3.1.4.1 Initial guesses

Initial guesses of parameters are determined within physically reasonable ranges of the VRBC systems. For example, the kinetic constants at electrodes for redox batteries are known to be of the order of 10^{-6} to 10^{-9} [43, 46]. The formal potential is known as the value of 1.4 V for 2M vanadium ions in 5M sulfate electrolytes at 50% state-of-charge [49]. The value of the total resistance of the batch cell is not reported but its initial guess is determined by fitting with experimental data based on the initial guesses of other parameters. The initial guesses for the rate constants at the positive and negative electrodes, the formal potential, and the cell resistance were 1.02×10^{-6} m/s, 1.37×10^{-6} m/s, 1.4 V, and 2 Ω, respectively.

3.3.1.4.2 Lower and upper bounds

The lower and upper bounds for rate constants at the positive and negative electrodes were 2.50×10^{-6} to 4.04×10^{-6} m/s and 3.56×10^{-7} to 5.29×10^{-6} m/s, respectively. In this case, a range of ±20% from the initial guesses applies to the scaled exponential values (A and B). The bounds for the formal potential were given as 1.26 to 1.54V. The lower bound was set up to a standard potential (=1.26V) for reactions at the positive and negative electrodes in the VRBC system, and the upper

(a) Charging

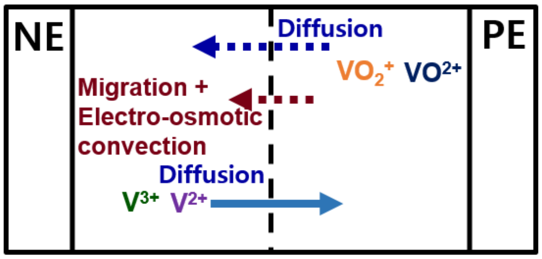

(b) Discharging

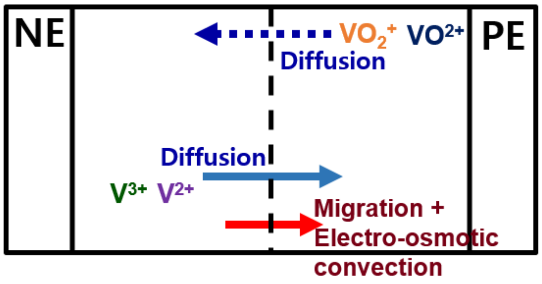

Figure 3.6. Crossover of vanadium ions through the membrane in the uni-direction model during (a) charging and (b) discharging. PE and NE represent positive and negative electrodes, respectively. A blue-colored dotted arrow indicates VO^{2+}/VO_2^+ diffusion (see the first arrow from the top in (a) Charge and (b) Discharge), a wine-colored dotted arrow represents VO^{2+}/VO_2^+ migration and electro-osmotic convection (see the second arrow from the top in (a) Charging), a sky-blue colored solid arrow shows V^{2+} / V^{3+} diffusion (see the third arrow from the top in (a) Charging and the second arrow from the top in (b) Discharging), and a red-colored solid arrow represents V^{2+}/V^{3+} migration and electro-osmotic convection (see the third arrow from the top in (b) Discharging).

bound was determined to be in the range of +10% from the initial guess. The lower and upper bounds for the cell resistance were 0 and 5 Ω, respectively. The bounds of the batch cell resistance were adjusted to broader ranges to precisely investigate the optimized values because physically meaningful values were not available.

3.3.1.4.3 Results

The converged parameters for rate constants at the positive and negative electrodes, the formal potential, and the cell resistance are 2.05×10^{-6} m/s, 4.23×10^{-7} m/s, 1.43 V, and 5 Ω. The minimized MSE was 1.72 mV. The comparison of voltage profiles between model outputs and experimental data is shown in Figure 3.8a. The results indicate that there is a significant discrepancy between model outputs and experimental data. Both charging and discharging predictions from model outputs have longer profiles than experimental data. Additions of more detailed physics and ions transport are required.

3.3.2 *Model 2: Diffusion model + Uni-directional migration and convection*

The concepts of uni-directional vanadium ions' migration and electro-convection are added to the diffusion model and validated. In the VRFB system, convection effects consist of the hydraulic-osmotic and the electro-osmotic convection [46, 50]. The hydraulic-osmotic convection occurs due to water osmosis by the half-cell pressure gradient. This effect causes the crossover of water along with ions through the membrane due to viscous interactions between fluid and charge carriers. In the electro-osmotic convection, ions diffusion and migration lead to a half-cell osmotic gradient, and the water movement due to this osmotic gradient carries the ions again [46, 50]. For the hydraulic-osmotic convection, when the volumetric flow of the system is static, the half-cell pressure gradient becomes negligible because the half-cell gradient is proportional to the volumetric flow of the system [46]. In the VRBC system, therefore, the hydraulic osmotic effect can be negligible due to static electrolytes, and only the electro-osmotic effect is considered [68]. In a real VRBC system, both migration and electro-osmotic convection are applied from the positive to the negative electrolyte during charging, and from the negative to the positive during discharging. According to the uni-direction zero-dimensional model proposed by P. A. Boettcher et al. [44], however, it is not possible for migration and convection effects to have the anti-directional flux to counter the diffusion flux since there are no ion sources from the opposite compartment [44]. Therefore, the uni-direction model includes only VO^{2+} and VO_2^+ ions' migration and convection effects from the positive to negative electrolyte during charging, and only V^{2+} and V^{3+} ions' migration and convection effects from the negative to the positive electrolyte during discharging, as shown in Figure 3.6 [44].

3.3.2.1 Assumptions

In addition to the assumptions of the diffusion model, one more assumption is added i.e. (viii) The membrane conductivity is constant during charging and discharging.

3.3.2.2 Equations

For governing equations, Equations 3.1~3.4 and 3.5~3.8 in Table 3.2 and 3.3 are used. Uni-directional migration and electro-osmotic convection effects have been added to the diffusion model [43, 44, 46, 68]. For additional equations, Equations 3.9-2, 3.10-1, 3.11, 3.12, and 3.13 are used [43, 44, 49, 68]. The cell system's ohmic loss of the diffusion model is divided into ohmic losses associated with the membrane resistance and the cell system resistance excluding the membrane resistance, as shown in Equation 3.9-2. The potential gradient and the convection velocity across the membrane can be expressed as Equations 3.12 and 3.13, respectively [43, 44, 49, 68].

3.3.2.3 Parameter estimation

There are five parameters to be estimated; rate constants at the positive and negative electrodes, the cell resistance excluding the membrane resistance, the formal potential, and the membrane conductivity. The membrane resistance can be quantified by dividing the thickness of the membrane by the membrane area and conductivity (*see Equation 3.9-2*).

3.3.2.3.1 Initial guesses

The same initial guesses are applied to the same parameters used in the diffusion model. The initial guess for the additional parameter, i.e. the membrane conductivity, is determined at a value of 10 S/m based on the known physical range of the Nafion® 115 membrane conductivity within 5 and 30 S/m [45, 50, 69].

3.3.2.3.2 Lower and upper bounds

The same bounds are used for the same parameters of the diffusion model. The bounds for the membrane conductivity were given as 0 to 20 S/m to find the optimal value within a physically meaningful range, and the lower and upper bounds for the cell resistance excluding the membrane resistance were 0 to 5 Ω, respectively.

3.3.2.3.3 Results

The converged parameters for rate constants at the positive and negative electrodes, the cell resistance excluding the membrane resistance, the formal potential, and the membrane conductivity are 8.75×10^{-7} m/s, 1.36×10^{-6} m/s, 5 Ω, 1.45 V, and 4.84 S/m, respectively. Also, the minimized MSE was 0.46 mV. The comparison of voltage profiles between model outputs and experimental data is presented, as shown in Figure 3.8b. The result shows that the end part of the charging profile between model outputs and the experimental data is not matched well. The longer charging profile is predicted from model outputs compared to the experimental data. Therefore, more accurate zero-dimesional models are required, adding detailed physics or ion transport.

3.3.3 *Model 3: Diffusion model + Full directional migration and convection*

In this section, anti-directional migration and electro-osmotic convection for diffusion are added to the uni-direction model in the previous section. The zero-dimentional model, which includes both anti- and uni- directional migration and convection, was proposed by M. Pugach *et al.* in 2018 [45]. This model adopts analytical solutions for ions' migration and convection [50] and uses the formal potential to calculate the open circuit potential. When vanadium ions cross the membrane, the ions face the potential gradient, which slows down or increases the total ion flux, as described in Figure 3.7. The migration and electro-osmotic convection effects occur from the positive side to the negative side during charging, which is the same direction to the diffusion flux of VO^{2+} and VO_2^+ and the opposite direction to the diffusion flux of V^{2+} and V^{3+}. During discharging, the migration and electro-osmotic convection effects occur from the negative side to the positive side for vanadium ions of the system. In vanadium redox battery systems, when migration and convection are in the opposite direction to diffusion, the diffusion effect is typically larger than the sum of migration and convection effect [46]. In this case, it might be reasonable for a zero-dimensional model to include both uni- and anti-directional convection and migration. To ensure that this concept helps improve the accuracy of the model, the full-direction model is validated.

3.3.3.1 Assumptions

The same assumptions used in the uni-direction model are used.

3.3.3.2 Equations

For governing equations, Equations 3.1´- 3.4´and 3.5´- 3.8´ in Tables 3.2 and 3.3 are used. The same additional Equations 3.9-2, 3.10-1, 3.11, 3.12, and 3.13 used in the uni-direction model are used.

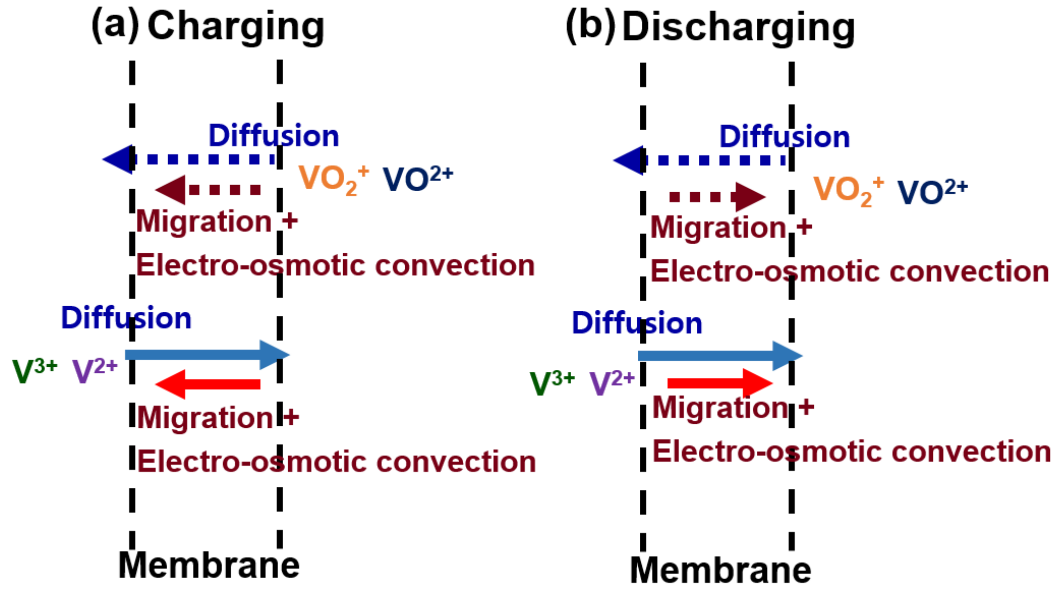

Figure 3.7. Crossover of vanadium ions through the membrane by diffusion, migration, and electro-osmotic convection during (a) charging and (b) discharging. A blue-colored dotted arrow indicates VO^{2+}/VO_2^+ diffusion (see the first arrow from the top in (a) Charge and (b) Discharge), a wine-colored dotted arrow represents VO^{2+}/VO_2^+ migration and electro-osmotic convection (see the second arrow from the top in (a) Charging and (b) Discharging), a sky-blue colored solid arrow shows V^{2+} / V^{3+} diffusion (see the third arrow from the top in (a) Charging and (b) Discharging), and a red-colored solid arrow represents V^{2+}/V^{3+} migration and electro-osmotic convection (see the fourth arrow from the top in (a) Charging and (b) Discharging). The main transport phenomena of the batch system are diffusion, migration, and electro-osmotic convection. The diffusion of vanadium ions through the membrane has the same direction regardless of charging and discharging and the direction of migration and electro-osmotic convection through the membrane is affected by charging/discharging conditions.

3.3.3.3 Parameter estimation

The same parameters used in the uni-direction model are estimated, and all initial guesses and bounds are the same as the uni-direction model.

3.3.3.3.1 Results

The converged parameters for the rate constants at the positive and negative electrodes, the cell resistance excluding the membrane resistance, the formal potential, and the membrane conductivity are 1.20×10^{-6} m/s, 1.16×10^{-6} m/s, 2.95 Ω, 1.45 V, and 6.05 S/m, respectively. Also, the minimized MSE was 0.19 mV. The fit of voltage profiles between model outputs and experimental data has a good agreement, as shown in Figure 3.8c. According to the literature, both zero-dimesional uni- and full-direction models for VRFB systems are fitted well with experimental data for a single cycle [44, 45]. In the VRBC system at low C-rates, however, only the full-direction model leads to more accurate prediction compare to the uni-direction model. One of the possible reasons is that in the VRBC system at low C-rates, capacity loss occurs explicitly even for the first cycle. Adding inaccurate ions transport terms can cause significant differences between model outputs and experimental data. This can be a good example of showing how the batch cell system at low C-rates, which does not look like a practical system, can contribute to improving the model development, and why the systems approach is essential for the accurate prediction of the battery performance.

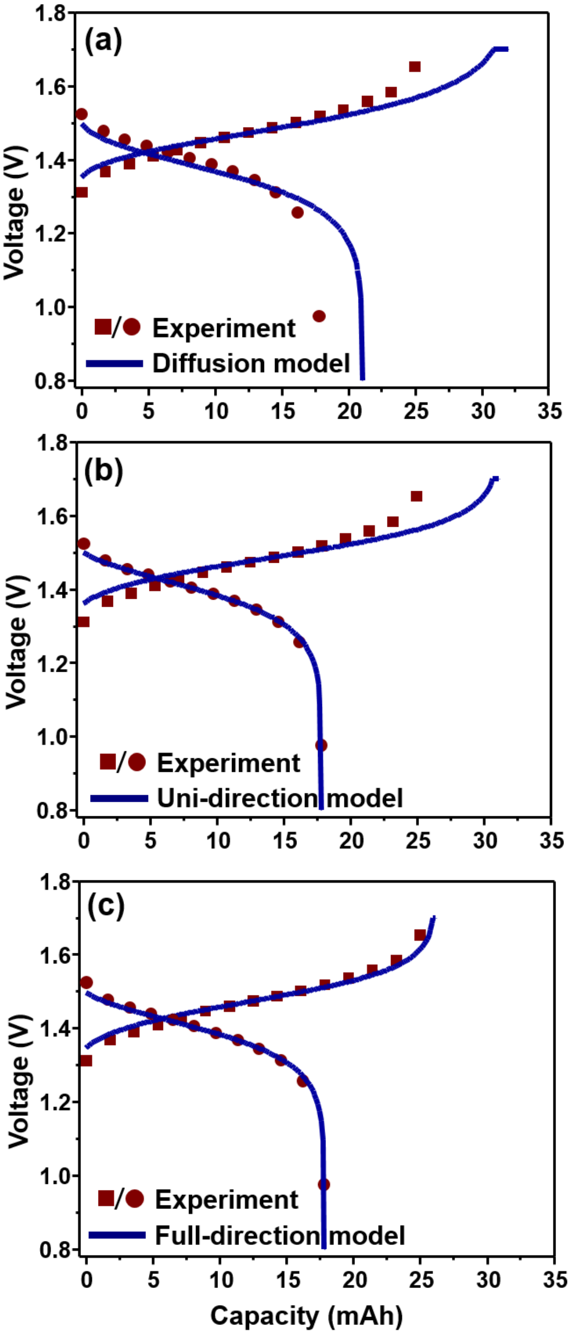

Figure 3.8. Model formulation process and comparison of voltage profiles between different model outputs and experimental data from the batch cell system including the Nafion® 115 membrane. Voltage profiles at C/30 (Experimental data: charge (wine color and filled square dots), discharge (wine color and filled circle), the model (blue-color straight line). (a) Diffusion model (b) Uni-direction model (c) Full-direction model. Parameters were simultaneously estimated at C/30, minimizing the mean of the sum-of-squared differences between the model and experiment outputs.

3.3.4 *Model 4: Diffusion model + Full directional ion flux+ Proton transport*

In the full-direction model, the formal potential was derived by taking the proton concentration and activity coefficients of vanadium ions from the logarithmic term of the open circuit voltage. In this case, the value of the formal potential needs to be identified or estimated for every other C-rate and different systems including different membranes. This is not an efficient way of utilizing a systems approach. The ideal case is that one set of all estimated parameters obtained from one set of experimental data should be applied to other sets of experimental data. For this, the dynamics of proton concentrations is added to the full direction model. In the previous section, the membrane conductivity was assumed to be constant during the cell operation. However, the membrane conductivity can be approximated by Equation 3.14 in Table 3.4, including the protons' concentration and diffusion coefficient. By doing this, the proton transport effect is added to the full-direction model while keeping the number of estimated parameters same.

3.3.4.1 Assumptions

The assumption (vii) for the diffusion model need to be modified as follows: (vii) Activity coefficients of vanadium ionic species are not equal to 1.

3.3.4.2 Equations

For governing equations, Equations 3.1´~ 3.4´, 3.5´~ 3.8´, and 3.9~3.12 in Tables 3.2, 3.3, and 3.7 are used, respectively. For additional equations, Equations 3.9-2, 3.10-2, and 3.11~3.14 in Table 3.4 are used. The logarithmic term of the open circuit voltage, including the proton concentration term, is used as shown in Equation 3.10-2, and the membrane conductivity is expressed as Equation 3.14.

3.3.4.3 Parameter estimation

There are five parameters to be estimated; rate constants at the positive and negative electrodes, the cell resistance excluding the membrane resistance, the formal potential, and the diffusion coefficient of protons. The initial guesses, bounds, and converged parameters are summarized in Table 3.8, and values in Table 3.8 were rounded off to the third decimal place.

3.3.4.3.1 Initial guesses

Initial guesses for rate constants at the positive and negative electrodes and the cell resistance excluding the membrane resistance are the same with the full-direction model. However, initial guesses of the formal potential and protons' diffusion coefficient are determined as the value of 1.35 V and 1.03×10^{-10} m^2/s, respectively. The converged value of the formal potential of the proposed model in this section is expected to be smaller than the converged value from the full-direction model in the previous section since the proton concentration term is taken from the logarithmic term and added back to the logarithmic term of Equation 3.14-2. Also, Nafion® membranes typically allow the proton transport 10^2 ~10^3 times faster than other ions [46, 68].

3.3.4.3.2 Lower and upper bounds

Bounds for rate constants at the positive and negative electrodes and the cell resistance excluding the membrane resistance are the same as the full direction model. The bounds for the formal potential were given as 1.26 V to 1.49 V. A standard potential was used for the lower bound, and a deviation of +10% from the initial condition was applied to the upper bound. The ±20% ranges of lower and upper bounds for the diffusion coefficient of protons were applied to the scaled exponential values. Therefore, the bounds for the diffusion coefficient of protons were given as 1.03×10^{-11} to 1.02×10^{-9} m^2/s.

3.3.4.3.3 Results

The converged parameters for rate constants at the positive and negative electrodes, the cell resistance excluding the membrane resistance, the formal potential, and the diffusion coefficient of protons are 1.13×10^{-6} m/s, 1.13×10^{-6} m/s, 2.98 Ω, 1.35 V, and 1×10^{-10} m^2/s, respectively. Also, the minimized MSE was 0.22 mV, and a good agreement between model outputs and experimental data is observed, as shown in Figures 3.9a. To study and analyze the effects of ions' transport in the VRBC system, a simple model, which does not include diffusion, migration, and electro-osmotic convection of vanadium ions through the membrane, is presented as shown in Figures 3.9b, 3.9d, and 3.9f. There are no mathematical equations describing crossover of vanadium ions through the membrane in the simple model. So, in the simple model, only Accumulation and Generation terms of the Equations 3.1~3.4 (or 3.1´~3.4´) and 3.5~3.8 (or 3.5´~3.8´) in Tables 3.2 and 3.3 are used for charging and discharging, respectively. Except for the governing equations of vanadium ions, the same equations used in the full-direction model including the proton effect are simulated adopting the proton transport (Equations 3.15~3.18 in Table 3.7), additional equations (Equations 3.9-2, 3.10-2, 3.11, 3.12, and 3.13 in Table 3.4) with parameters (Tables 3.5), and estimated parameters (Table 3.8).

In Figures 3.9a and 3.9b, the charging profile of the VRBC model, that includes the effect of diffusion, migration, and convection is found longer than that of the simple model. Partial self-discharge of vanadium ions through the membrane is one of the main reasons for this capacity loss. To study this capacity loss in details, Figures 3.9c, 3.9d, 3.9e, and 3.9f describe the comparison of the predicted concentration of vanadium ions for the VRBC system as well as the simple model. Ideally, V^{2+} ions should only be generated from V^{3+} ions through an electrochemical reaction at the negative electrode during charging (*see Figure 3.9d*). In reality, V^{2+} ions are continuously depleted in negative electrolytes due to side reactions with VO^{2+}/VO_2^+ ions and crossover of V^{2+} ions through the membrane (*see Figure 3.9c*). Likewise,

VO_2^+ ions should be only produced for charging (*see Figure 3.9f*), but they are also depleted in the positive electrolyte because of their crossover and side reactions giving rise to VO^{2+} ions (*see Figure 3.9e*). The self-discharge of vanadium ions, which happens during charging, causes a slower charging until the cell is achieved at the maximum voltage. In contrast, this self-discharge leads to faster discharge in shorter discharge time. During discharge, V^{2+} and VO_2^+ ions are depleted due to electrochemical reactions at the negative electrode and their side reactions with other vanadium ions and crossover through the membrane, thereby dropping the concentration of V^{2+} and VO_2^+ ions faster (*see Figures 3.9c and 3.9e*). For this reason, the self-discharge of vanadium ions, which happens during discharge, causes a faster discharge until the cell achieves the minimum voltage. Importantly, the VRBC/VRFB system does not produce any inert third compound, such as Li-ion SEI/plating, that can cause irreversible capacity loss [70]. Rather, side reactions in VRBC/VRFB systems are disproportionate reactions, which convert vanadium ions from one oxidation state to another state [49].

3.3.4.3.4 Sensitivity analysis for the Initial guess

Table 3.9 describes the sensitivity analysis for the initial guess. The sensitivity analysis was conducted with changes of -10%, -5%, +5%, and 10% from the original initial guess. When one initial guess is changed, the other initial guesses remain at their original value. For the Nafion® 115 system, the optimal value of most parameters is stable for the changes in initial guesses (up to 20%). However, the cell resistance excluding the membrane shows a tendency to be unstable for initial guesses variations.

Table 3.7. Governing equations for proton transport

Accumulation	= Generation	+ In – Out (Diffusion terms)	(Migration and electro-osmotic convection terms)	No.
Charge				
$V_r \dfrac{dC_{H_p^+}(t)}{dt}$	$= + \dfrac{2i_{app}}{F}$	$+\left(D_{H^+}C_{H_n^+}(t) - D_{H^+}C_{H_p^+}(t)\right)\dfrac{A_m}{d_m}$	$-\left(D_{H^+}C_{H_p^+}(t) + D_{H^+}C_{H_n^+}(t)\right)\dfrac{F}{RT}A_m\nabla\phi - v_m\left(C_{H_p^+}(t) + C_{H_n^+}(t)\right)A_m$	**[3.15]**
$V_r \dfrac{dC_{H_n^+}(t)}{dt}$	$= 0$	$+\left(-D_{H^+}C_{H_n^+}(t) + D_{H^+}C_{H_p^+}(t)\right)\dfrac{A_m}{d_m}$	$+\left(D_{H^+}C_{H_p^+}(t) + D_{H^+}C_{H_n^+}(t)\right)\dfrac{F}{RT}A_m\nabla\phi + v_m\left(C_{H_p^+}(t) + C_{H_n^+}(t)\right)A_m$	**[3.16]**
Discharge				
$V_r \dfrac{dC_{H_p^+}(t)}{dt}$	$= - \dfrac{2i_{app}}{F}$	$+\left(D_{H^+}C_{H_n^+}(t) - D_{H^+}C_{H_p^+}(t)\right)\dfrac{A_m}{d_m}$	$+\left(D_{H^+}C_{H_p^+}(t) + D_{H^+}C_{H_n^+}(t)\right)\dfrac{F}{RT}A_m\nabla\phi + v_m\left(C_{H_p^+}(t) + C_{H_n^+}(t)\right)A_m$	**[3.17]**
$V_r \dfrac{dC_{H_n^+}(t)}{dt}$	$= 0$	$+\left(-D_{H^+}C_{H_n^+}(t) + D_{H^+}C_{H_p^+}(t)\right)\dfrac{A_m}{d_m}$	$-\left(D_{H^+}C_{H_p^+}(t) + D_{H^+}C_{H_n^+}(t)\right)\dfrac{F}{RT}A_m\nabla\phi - v_m\left(C_{H_p^+}(t) + C_{H_n^+}(t)\right)A_m$	**[3.18]**

Table 3.8. Estimated parameters of all-Vanadium redox batch cell systems (full-direction model)

Symbol	Parameter	Lower bound	Upper bound	Initial guess	95% Confidence interval	Final value	Units
$R_{cell\text{-}mem}$	Resistance excluding the membrane resistance	0	5	2	2.93~3.03	2.98	Ω
k_c	Rate constant at positive electrode	0.20×10^{-6}	4.04×10^{-6}	1.02×10^{-6}	1.07~ 1.19×10^{-6}	1.13×10^{-6}	$m^2\,s^{-1}$
k_a	Rate constant at negative electrode	3.56×10^{-7}	5.29×10^{-6}	1.37×10^{-6}	1.06 ~ 1.21×10^{-6}	1.13×10^{-6}	$m^2\,s^{-1}$
$E_0^{'}$	Formal potential	1.26	1.49	1.35	1.34~1.35	1.35	V
D_{H^+}	H^+ diffusion coefficient of						
	Nafion® 115	1.03×10^{-11}	1.02×10^{-9}	1.03×10^{-10}	9.93×10^{-11}~1×10^{-10}	1×10^{-10}	$m^2\,s^{-1}$
	Nafion® XL	3.09×10^{-11}	2.52×10^{-9}	2.79×10^{-10}	4.32×10^{-11} ~8.84×10^{-10}	1.66×10^{-10}	$m^2\,s^{-1}$
$D_{V^{2+}}$	V^{2+} diffusion coefficient for Nafion® XL	1.26×10^{-13}	2.8×10^{-11}	1.88×10^{-12}	3.02×10^{-14} ~2.58×10^{-11}	0.88×10^{-12}	$m^2\,s^{-1}$
$D_{V^{3+}}$	V^{3+} diffusion coefficient for Nafion® XL	1.26×10^{-13}	2.8×10^{-11}	1.88×10^{-12}	9.37×10^{-13} ~ 1.73×10^{-12}	1.27×10^{-12}	$m^2\,s^{-1}$
$D_{VO^{2+}}$	VO^{2+} diffusion coefficient for Nafion® XL	8.2×10^{-13}	1.29×10^{-10}	1.03×10^{-11}	8.58×10^{-12} ~ 1.21×10^{-11}	1.02×10^{-11}	$m^2\,s^{-1}$
$D_{VO_2^+}$	VO_2^+ diffusion coefficient for Nafion® XL	3.79×10^{-13}	6.88×10^{-11}	5.11×10^{-12}	4.09×10^{-12} ~ 5.33×10^{-12}	4.67×10^{-12}	$m^2\,s^{-1}$

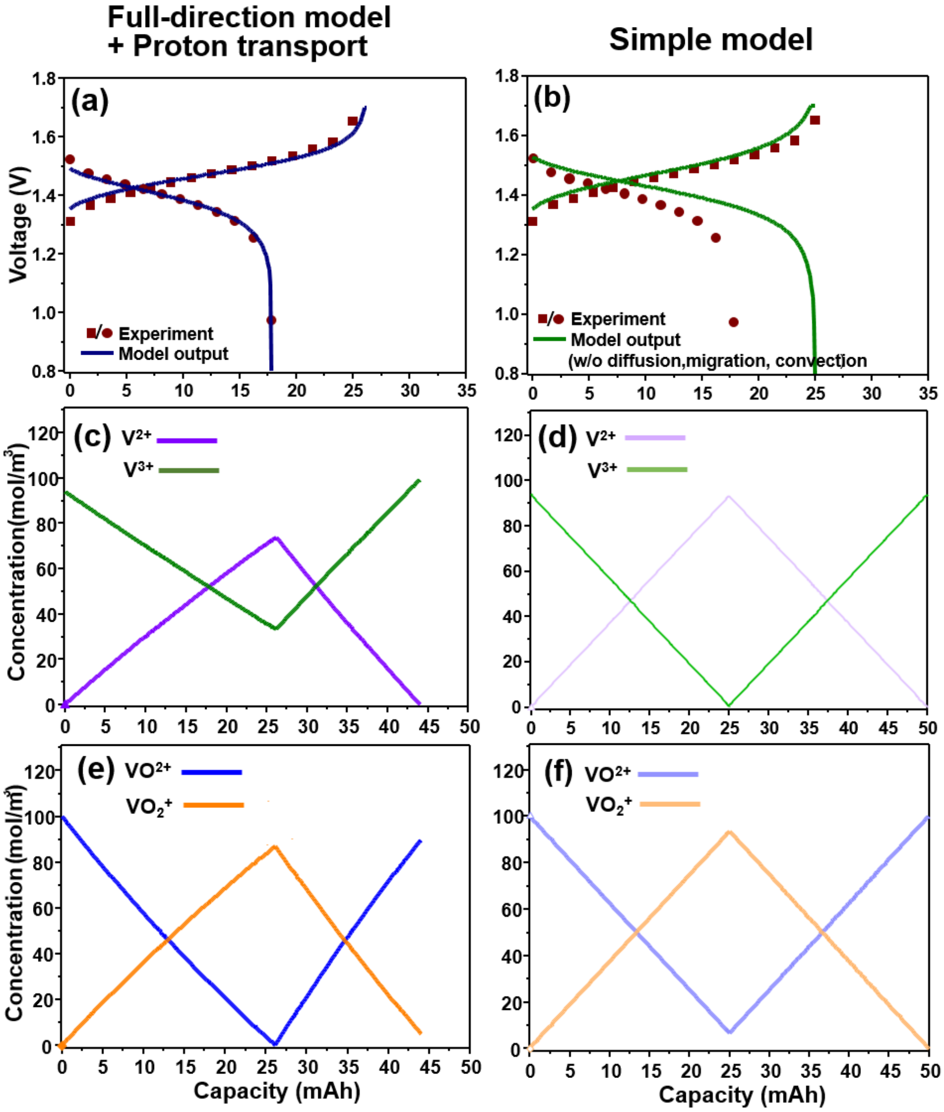

Figure 3.9. Comparison of voltage and predicted concentration profiles between the full-direction model including the proton transport and the simple model for the batch cell system equipped with the Nafion® 115 membrane at C/30. (Experimental data: charge (wine color and filled square dots), discharge (wine color and filled circle), the full-direction model: blue-color straight line, and the simple model: green-color straight line). (a) Full-direction model including the proton transport vs. experimental data, (b) Simple model vs. experimental data, (c) V^{2+} (purple color) and V^{3+} (green color) concentration profiles from the VRBC model at C/30, (d) V^{2+} (light purple color) and V^{3+} (light green color) concentration profiles from the simple model at C/30, (e) VO^{2+} (blue color) and VO_2^+ (orange color) concentration profiles from the VRBC model at C/30, and (f) VO^{2+} (light blue color) and VO_2^+ (light orange color) concentration profiles from the simple model at C/30. An imbalance of the vanadium ion concentration between the positive and negative electrolytes causes capacity loss of VRBC/VRFB systems. and the simple model: green-color straight line).

Table 3.9. Sensitivity Analysis for Initial Guesses

Parameter	Original initial guess	Original optimal value	Optimal value from the initial guess variation				
Nafion® 115 system			Initial guess variation				
			k_a ± 10%	k_c ± 10%	E_0' ± 10%	$R_{cell\text{-}mem}$ ± 10%	D_{H^+} ± 10%
Rate constant at negative electrode (k_a) $\times 10^{-6}$	1.37	1.13	1.06 ~ 1.61	1.05~1.17	0.91~1.33	1.14~1.18	1.18~1.33
Rate constant at positive electrode (k_c) $\times 10^{-6}$	1.02	1.13	0.91~1.28	1.03~1.26	0.96~1.32	1.05~1.14	1.04~1.10
Formal potential (E_0')	1.35	1.35	1.35~1.35	1.35~1.35	1.35~1.35	1.35~1.35	1.35~1.35
Resistance excluding the membrane resistance ($R_{cell\text{-}mem}$)	2	2.98	1.36~ 4.97	0.40~5.00	1.17~2.06	1.72~3.24	1.64~5.00
H^+ diffusion coefficient (D_{H^+}) $\times 10^{-10}$	1.03	1	1~1	1~1	1~1	1~1	1~1
Nafion® XL system			Initial guess variation				
			$D_{V^{2+}}$ ± 10%	$D_{V^{3+}}$ ± 10%	$D_{VO^{2+}}$ ± 10%	$D_{VO_2^+}$ ± 10%	D_{H^+} ± 10%
V^{2+} diffusion coefficient for Nafion® XL ($D_{V^{2+}}$) $\times 10^{-12}$	1.88	0.88	0.22~1.21	0.13~1.69	0.13~0.25	0.13~1.41	0.13~1.52
V^{3+} diffusion coefficient for Nafion® XL ($D_{V^{3+}}$)$\times 10^{-12}$	1.88	1.27	1.10~1.42	1.06~1.86	1.13~1.45	1.15~1.73	0.95~1.67
VO^{2+} diffusion coefficient for Nafion® XL ($D_{VO^{2+}}$)$\times 10^{-11}$	1.03	1.02	0.48~0.97	0.97~1.04	0.98~1.07	1.00~1.04	0.95~1.01
VO_2^+ diffusion coefficient for Nafion® XL ($D_{VO_2^+}$) $\times 10^{-12}$	5.11	4.67	4.77~4.94	4.68~5.08	4.60~5.00	4.5~5.23	4.76~5.15
H^+ diffusion coefficient (D_{H^+}) $\times 10^{-10}$	2.79	1.66	1.68~1.93	1.74~2.42	1.96~2.84	1.65~2.86	1.67~2.31

3.4 MODEL VALIDATION WITH DIFFERENT MEMBRANES

In this section, a systems approach is performed with the Nafion® XL system, using the full-direction model including the proton transport in the previous section. In the Nafion® 115 and Nafion® XL system, some parameters are known a priori while other parameters are estimated through the parameter estimation approach, as shown in Figure 3.3. For example, diffusion coefficients of vanadium ions for other membranes, which have not yet been investigated, are estimated based on the predetermined other parameters in the Nafion® 115 cell system. The Nafion® XL membrane equipped batch cell system has been considered, where diffusion coefficients have not been identified. Therefore, there are total ten parameters to be estimated; four diffusion coefficients of different vanadium ionic species for Nafion XL, two diffusion coefficients of protons for Nafion® 115 and XL membranes, the cell resistance excluding the membrane resistance, two rate constants at cathode and anode, and the formal potential. While system parameters, including the formal potential, the cell resistance excluding the membrane resistance, and two rate constants at electrodes remain the same as obtained for the Nafion® 115 system, other remaining parameters including five diffusion coefficients of the ionic species through the Nafion® XL membrane are estimated through the systems approach. The diffusion coefficients of five ionic species are expressed and scaled in term of exponential functions as well, where the indices appearing to the power of the exponential factor (e) are used as the parameters for optimization.

3.4.1 *Assumption and equations*

The same assumptions and equations used in the full-direction model are used.

3.4.2 *Parameter estimation*

The same systems approach used in the full-direction model inlcuding the proton transport has been attempted at C/30. There are five parameters to be estimated; five diffusion coefficients of vanadium ions and protons. The initial guesses, bounds, and converged parameters are summarized in Table 3.8, and values in Table 3.8 were rounded off to the third decimal place.

3.4.2.1 Initial guesses

Diffusion coefficients of the Nafion® membrane are known to be in the range of 10^{-11} to $10^{-13,}$ [44, 46, 49] and the diffusion coefficient of protons is known to be in the scale of 10^{-9} to 10^{-10}. Based on this information, the initial guesses for diffusion coefficients of V^{2+}, V^{3+}, VO^{2+}, VO_2^{+}, and protons were determined as the value of 1.88×10^{-12} m^2/s, 1.88×10^{-12} m^2/s, 1.03×10^{-11} m^2/s, 5.11×10^{-12} m^2/s, and 2.79×10^{-10} m^2/s, respectively.

3.4.2.2 Lower and upper bounds

The range of lower and upper bounds for ions diffusion coefficients was set up using the scaled exponential values with a range of ±20% from the initial guesses. Therefore, the lower and upper bounds for diffusion coefficients of V^{2+}, V^{3+}, VO^{2+}, VO_2^{+}, and protons were 1.26×10^{-13} to 2.80×10^{-11} m^2/s, 1.26×10^{-13} to 2.80×10^{-11} m^2/s, 8.2×10^{-13} to 1.29×10^{-10} m^2/s, 3.79×10^{-13} to 6.88×10^{-11} m^2/s, and 3.09×10^{-11} to 2.52×10^{-9} m^2/s respectively.

3.4.2.3 Results

The converged values for diffusion coefficients of V^{2+}, V^{3+}, VO^{2+}, VO_2^{+} and protons are estimated as 0.88×10^{-12} m^2/s, 1.27×10^{-12} m^2/s, 1.02×10^{-11} m^2/s, 4.67×10^{-12} m^2/s, and 1.66×10^{-10} m^2/s, respectively. The minimized MSE of the Nafion® XL system is 1.21 mV. Figure 3.10a presents the comparison of voltage profiles between the model output and the experimental data, and Figures 3.10b and 3.10c show the predicted concentration of V^{2+}, V^{3+}, VO^{2+}, and VO_2^+ ions of the batch cell system having Nafion® XL membrane. Like the Nafion® 115 system, the changes in concentration of V^{2+}/V^{3+} ions are smaller than that of VO^{2+}/VO_2^+ ions during charging**.** The imbalance of vanadium ion concentration between the positive and negative electrolytes causes capacity loss of VRBC systems. The imbalance of the Nafion® XL system is more severe than that of Nafion® 115. In Figure 3.10b, one of the observed phenomena is that the change in concentration of V^{2+} ions follows a typical behavior of vanadium redox flow batteries, but the concentration of V^{3+} ions barely changes during charge. Initially, the concentration of V^{3+} ions slightly increases and then begins to decrease. This is because the applied C-rate is significantly lower than that of typical vanadium redox flow battery systems. The low applied C-rate reduces the consumption rate of V^{3+} ions at the electrode. Also, the estimated diffusion coefficient of V^{3+} ions is smaller than that of VO^{2+} and VO_2^+ ions. As a result, the entering rate of V^{3+} ions through the membrane by the side reaction of VO^{2+} and VO_2^+ ions is higher than the sum of the rate of consumption of V^{3+} ions at the negative electrode and flowing-out rate of V^{3+} ions to the opposite electrolyte. This is the reason that the concentration of V^{3+} ions increases initially. Meanwhile, in the positive electrolyte, the concentration of VO_2^+ ion is increasing, and the concentration of VO^{2+} ions is decreasing during the charging process. This affects the entering rate of V^{3+} ions through the membrane from the positive electrolyte. According to the result of the parameter estimation, the diffusion coefficient of VO^{2+} ions through the membrane is higher than that of other ions, and the changes in the concentration of VO^{2+} and VO_2^+ ions in the positive electrolyte lead to a reduction in the amount of V^{3+} ions entering. This causes a decrease in the concentration of V^{3+} ions in the

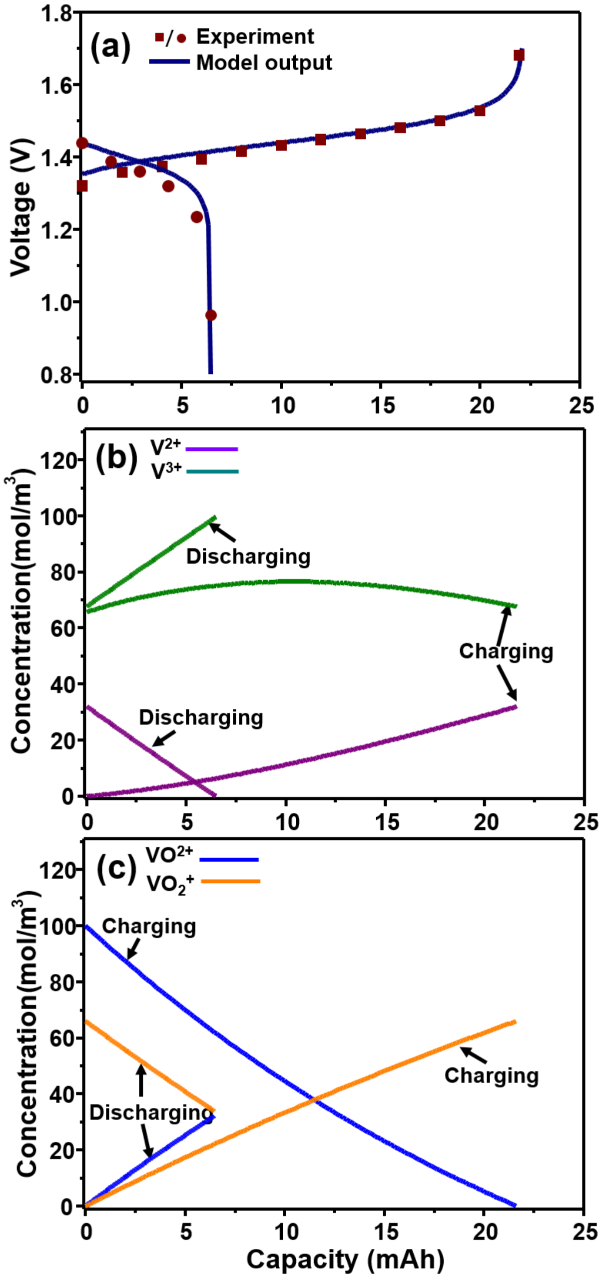

Figure 3.10. Comparison of voltage profiles between model outputs and experimental data, and predicted vanadium ion concentrations vs. capacity, for the batch cell system including the Nafion® XL membrane at the first cycle. The batch cell system is charged first and then discharged. (a) Voltage profiles from experiment data (charge: wine color and filled square, discharge: wine color and filled circle) and model outputs (blue-color straight line) at C/30 (b) V^{2+} (purple color) and V^{3+} (green color) concentration profiles at C/30. (c) VO^{2+} (blue color) and VO_2^+ (orange color) concentration profiles at C/30. Parameters were estimated at C/30 based on cell system parameters predetermined in the Nafion® 115 system, minimizing the mean of sum-of-squared differences between the model and experiment outputs.

negative electrolyte. Therefore, the concentration of V^{3+} ions begins to decrease after a certain time.

3.4.2.4 Sensitivity analysis for the Initial guesses

For the Nafion® XL system, the optimal values of diffusion coefficients from different initial guesses are more sensitive compared to optimal values in the Nafion® 115 system (*see Table 3.9*). Diffusion coefficients of VO^{2+} and VO_2^+ ions are relatively stable compared to diffusion coefficients of V^{2+} and V^{3+} ions. In most cases of VO^{2+} and VO_2^+ ions, the optimal values were estimated as ±15% deviation from the initial guess variations of the other parameters. However, the diffusion coefficients of V^{2+} and V^{3+} ions were estimated to be considerable difference depending on the initial guess variation. In the case of the Nafion® XL system, therefore, it is more important to estimate parameters by the proper initial guess.

3.5 UNIQUENESS ISSUE WITH A SYSTEM APPROACH

In most optimization methods for battery system simulations, it is required to identify appropriate initial guesses that provide model outputs, which are close to experimental data.[71] However, parameter estimation techniques pose the following fundamental question: How would one know if a set of estimated values is unique or not? In other words, how would one convince if the converged values are the global minimum? If not, would there be multiple sets of parameter values that would provide similar MSEs? The answers and efforts to mitigate theses doubts help build a better battery system coupling with parameter estimation techniques. For example, the order of magnitude of the diffusivity of vanadium ionic species for the Nafion® XL membrane was estimated as $VO^{2+}>VO_2^{+}>V^{3+}>V^{2+}$ in the previous section. However, the information on diffusivities of the vanadium ionic species for the Nafion® XL membrane is not available from the

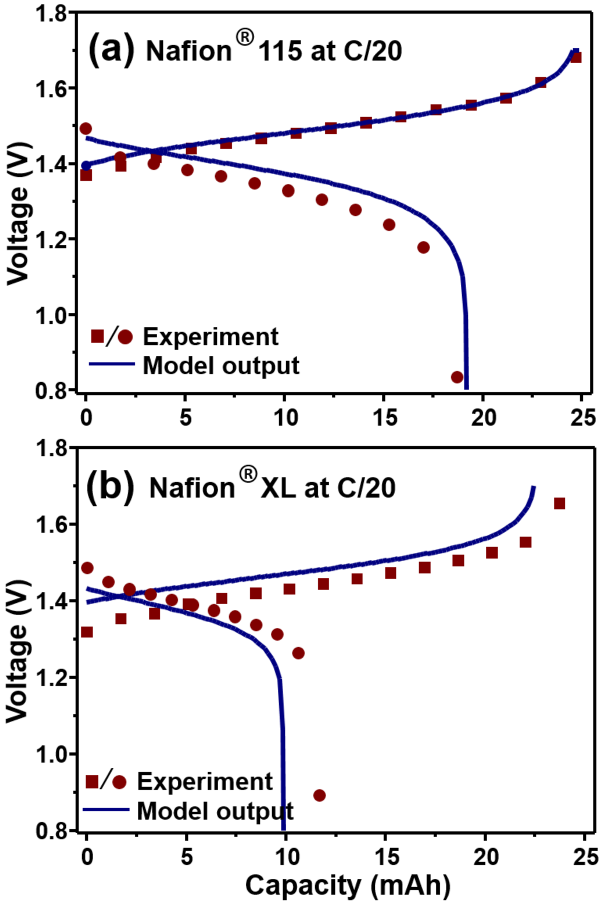

Figure 3.11. Comparison of voltage profiles between model outputs and experimental data from the batch cell system at C/20. Voltage profiles of (a) the Nafion® 115 system and (b) the Nafion® XL system (Experimental data: wine color and filled square dots, VRBC model outputs: blue color and straight plot).

literature, and how would the converged parameters be confirmed to be correct values using a systems approach? Currently, most global optimization techniques for battery simulations cannot guarantee the global minimum [71]. In parameter estimation, when a black-box model is used to simulate parameters and called with an optimizer, a global optimum cannot be guaranteed [71]. Therefore, one of the current approaches of dealing with this issue is to adopt more experimental data including different C-rates and confirm them with model outputs.[72, 73] Another way to mitigate the uncertainties of the converged values is to calculate the confidence interval.

3.5.1 *Different C-rates*

The estimated parameters in the previous step were applied to the system at higher C-rates (C/20), and a good agreement has been observed for both Nafion® 115 and Nafion® XL systems, having the low value of MSEs, as shown in Figure 3.11. The MSE of the Nafion® 115 and Nafion® XL system at C/20 is obtained as 2.67 mV and 16.49 mV, respectively. More experimental data will be utilized for parameter estimation studies of redox flow batteries to further improve the system reliability in our future work.

3.5.2 *Confidence interval*

The confidence interval is defined by an upper and lower limit, and within the confidence interval, the converged value is considered to be a statistically true value with a predefined level of confidence [50]. The small-confidence-interval model contains a smaller design uncertainty for the converged parameters [50]. The 95% confidence interval can be calculated as follows [64]:

$$\mathbf{p}_{opt} - t_{95\%} S_E \sqrt{a_{ii}} \le \mathbf{p} \le \mathbf{p}_{opt} + t_{95\%} S_E \sqrt{a_{ii}} \tag{3.C}$$

where $\boldsymbol{p}_{opt}$ is the vector of converged parameters, $t_{95\%}$ (=1.69) is the value of Student's t-distribution with (N-n_p) degrees of freedom, and the value of standard deviation (= S_E) is a square root of MSE (*see Equation 3.B*). The vector of a_{ii} is the i^{th} diagonal element of the inverse matrix of the transpose Jacobian multiplied by the Jacobian for parameter estimation, which is described as Equation 3.D.

$$(J^T \cdot J)^{-1}, J = \left(\frac{\Delta V}{\Delta p_i}\right)_j = \left(\frac{V(p_{opt,i} + \Delta p_i) - V(p_{opt,i})}{\Delta p_i}\right)_j \tag{3.D}$$

The i is the order of the estimating parameters, the j is the order of the experimental data point, J is the Jacobian, J^T is the transpose Jacobian, and Δp_i (=10^{-12}) is a change in the value of parameters. For this convergence interval calculation, the numerical Jacobian is calculated, which can be obtained using results from the computational software solver. The 95% confidence intervals for each parameter are summarized in Table 3.8, and values in Table 3.8 were rounded off to the third decimal place.

3.5.2.1 Nafion® 115 system

The 95% confidence intervals for the rate constants at the positive and negative electrodes, the cell resistance excluding the membrane resistance, and the diffusion coefficient of protons, and the formal potential are 1.07×10^{-6} to 1.19×10^{-6}m/s, 1.06×10^{-6} to 1.21×10^{-6} m/s, 2.93 to 3.03Ω, 9.93×10^{-11} to 1×10^{-10} m^2/s, and 1.34 to 1.35V, respectively.

3.5.2.2 Nafion® XL system

The 95% confidence interval for diffusion coefficients of V^{2+}, V^{3+}, VO^{2+}, VO_2^+, and protons are 3.02×10^{-14} to 2.58×10^{-11} m^2/s, 9.37×10^{-13} to 1.73×10^{-12} m^2/s, 8.58×10^{-12} to 1.21×10^{-11} m^2/s, 4.09×10^{-12} to 5.33×10^{-12} m^2/s, and 4.32×10^{-11} to 8.84×10^{-10} m^2/s, respectively.

3.6 OPEN SOURCE PLATFORM

Another possible way to confirm the uniqueness of the estimated parameters is to compare the converged values from different models describing the same system. The benefits and usability of this proposed approach can be accelerated and maximized through an open source platform provided in this paper (*see Figure 3.4*). The open source platform for models, experimental database, and estimation techniques enable users to continuously modify models with detailed physics, additional experimental data, and more optimizers. By doing this, users can arrive at robust optimization approaches. In an open source platform, executable files, source codes, and experimental data are also provided so that the proposed approach can be pragmatically implemented from users' point of view (*see the Appendix section*).

3.6.1 *Target users*

The executable files were designed for experimental researchers who are not familiar with mathematical approaches or have the necessary computational infrastructure. Also, the source codes can be used by both modelers and experimental researchers to understand redox flow cell models and optimization approaches. Most of the literature on parameter estimation of redox flow batteries only provide model equations, estimation methods, and simulation and estimation results [74-76]. In those cases, however, if users want to estimate parameters of the redox battery system by following a way of estimation published in the literature, they need to install the specific computational software, write down model equations, and reproduce parameter estimation techniques. Although parameter estimation is a very active area of research in practical applications, this process is not an efficient way from a practical point of view. To resolve this issue, we provide executable files where the original programs are written in Fortran. The executable files can be used as an optimization tool to quickly address the parameter estimation problems for the redox battery systems. For example, the executable files allow users to estimate model parameters by simply providing experimental conditions (e.g., applied current, voltage data, and time intervals) and bounds for the parameters. Users can execute the file without any special computational requirement including any software installation and a priori programming knowledge. This enables users to easily understand VRBC/VRFB models and parameter estimation approaches. The detailed instruction of the executable files is explained in the Appendix section.

3.6.2 *Solver and optimization*

The executable files were generated after compiling the model equation files written in Fortran and integrated the same with the open source DAE solver package with zero crossing (DASKR) [77], and Sequential Least SQuares Programming (SLSQP) [78]. The SLSQP algorithm includes the Han-Powell quasi-Newton method and it can identify and optimize the battery performance with high speed and accuracy.[65, 79] In this paper, the optimization algorithm was run to adopt high accuracy ($\sim 10^{-9}$) and a maximum of 1000 iterations.

3.6.3 *Converged parameters*

The same initial guesses of the parameters presented in the previous section of this paper and adjusted bounds were used for the executable files. The difference of most converged parameters optimized by NLPsolve in Maple and open source platform of SLSQP with DASKR interface was found to be less than 10%. While using the SLSQP optimization, the converged parameters of the Nafion® 115 system for rate constants at the positive and negative electrodes, the cell resistance excluding the membrane resistance, the diffusion coefficient of protons, and the formal potential are found as 1.01×10^{-6} m/s, 1.37×10^{-6} m/s, 2 Ω, 1.02×10^{-10} m/s, 1.39 V respectively. The converged parameters of the Nafion® XL system for the diffusion coefficients of V^{2+}, V^{3+}, VO^{2+}, VO_2^+, and protons, are found as 1.92×10^{-12} m^2/s, 1.94×10^{-12} m^2/s, 1.24×10^{-11} m^2/s, 4.78×10^{-12} m^2/s, 2.78×10^{-10} m^2/s, respectively.

Chapter 4. DIRECT NUMERICAL METHOD OF LINES TECHNIQUES FOR POTENTIAL AND CURRENT DISTRIBUTIONS: PRIMARY AND SECONDATRY APPROXIMATIONS

For detailed RFB models, an efficient simulation is important. In this chapter, as a starting point, we study and analyze the current distribution, which is governed by Laplace equations, using efficient and direct numerical method of lines techniques. The current distribution of electrochemical cell systems is directly related to electrochemical phenomena such as multiple simultaneous electrode reactions and electrolytic reactions in multiple-dimensional RFB models. Therefore, mathematical modeling of the current distribution can help understand the physical phenomena of the VRFB system, and an efficient and robust simulation approach can be utilized to control and design the system, maximizing usability and performance of VRFB cell systems. The mathematical way of identifying the current distribution is to solve the potential distribution, which is governed by Laplace's equation. However, most approaches to Laplace's equation have dealt with other applications and physics (e.g., steady-state heat transfer). Therefore, the objective of this paper is to provide efficient and robust numerical approaches for electrochemical cell systems. For this, a direct numerical method of lines is proposed, using staggered grid finite volume methods. It solves the system directly, adopting a standard computational solver. Also, the proposed approach adopts variable node spacing and polynomial approximations near boundary conditions to yield smoother and continuous current distribution profiles, addressing discontinuities in boundary conditions. This proposed approach can be extended to many different types of electrochemical cell systems, providing insight that minimizes computational costs of the system.

4.1 BACKGROUND

With advances in science and technology, various types/geometries of electrochemical cells have been developed in a wide range of research fields [80, 81]. Applications for electrochemical cells range from small Implantable Cardioverter-Defibrillator (ICD) devices operating at 10 micro-Ampere (µA) to large-scale energy storage systems that can quickly deliver 100 Ampere (A) transients, as shown in Table 4.1 [62, 80]. For example, there are typical lab-scale electrochemical cells, such as rectangular cell systems, hull cell systems, H-type cell systems, and coplanar galvanic thin-layer cell systems [71, 82-84]. Also, several new types/geometries of electrochemical cell systems have been developed for their own purpose. Prismatic and cylindrical types of lithium-ion batteries have been adopted in electric cars [85-87], multiple-stack rectangular cells have been implemented in renewable grid applications [62], a louvered configuration of photo-electrochemical cells have been developed for solar-driven water splitting systems [81], coplanar thin-layer galvanic cells have been utilized in a microfluidic sensor [88], and multi-plate or coiled configuration batteries have been developed for ICDs [80].

Different electrochemical cells have different geometries, which affect current distributions on electrodes of the system [89]. The current distribution is directly related to electrochemical phenomena such as multiple simultaneous electrode reactions (e.g., vanadium ions' interconversion and gas evolution in flow batteries) [71], moving boundaries in deposition/stripping process (e.g., dendrite growth in lithium metal batteries) [90, 91], and current distributions for electrode architectures (e.g., electrode design enhancing the system performance) [92]. Therefore, the electrochemical phenomena can be better understood through analysis of the current density distribution [93].

Table 4.1. Various types/geometries of electrochemical cells

Types	Application examples	Comments	Ref
Rectangular cell	Redox flow batteries: Large-scale energy storage system (kW to MW)	The system adopts porous electrode and multiple cells in multiple stacks.	[[62]]
Hull cell	Experimental tool: Investigation of single metal, alloy and composite deposition	The hull cell has been extended to several structures of hull cell (e.g., cylinder hull cell).	[[94-97]]
Coplanar electrode cell	Microfluidic device: microsensor	The electric field of the system is used for microsensors	[[88, 98]]
H-cell	Redox batch cell system: Study and analysis of ions transport	It helps clearly observes capacity fade of the system.	[[71]]
Louvered-design cell	Solar -hydrogen device	The device is photoelectrochemical cell system.	[[81]]
Cylindrical cell	Lithium-ion batteries: Electric vehicles (Tesla)	The structure can withstand high internal pressure without deforming.	[[85]]
Pouch cell	Lithium ion batteries: Electric vehicles, mobile phones, tablets, and laptops	The cell enables efficient space (90-95% packing efficiency).	[[99]]
Button cell (coin cells)	Medical implant, watches, hearing aids, car key, and memory backup	The cell is typically non-rechargeable battery.	[[99]]
Prismatic cell	Lithium ion batteries: Hybrid and electric vehicles.	The cell was introduced in the early 1990s. It satisfies thinner sizes.	[[99]]
Coiled configuration cell	Li battery: Implantable cardioverter defibrillators	Strips of anode and cathode wound together.	[[81]]

Modeling and simulation of the current distribution of electrochemical cells enable to help understand and control the system. In modeling and simulations, the current distribution has been typically identified by the potential distribution of electrochemical cell systems [100]. The potential distribution is governed by Laplace’ equation, which is driven from thin layer approximations assuming that the concentration gradient layer towards electrode is negligibly [100]. An efficient and robust simulation technique of Laplace’s equation for the potential/current distribution of electrochemical cells is a central research topic, which enables to maximize the system performance and usability. For example, lithium metal is receiving great attention in recent years as an anode material because of its high-energy density and capacity compared to the graphite used in lithium-ion batteries [101]. However, there have been safety concerns due to irregular dendrite growth at the lithium metal anode [102], and the behavior of dendrite growth is related to current distributions [91]. Efficient ways to simulate current distributions and control methodologies of the system might be one of the possible ways to control the dendrite growth more uniformly, maximizing battery life and usability [90, 91]. Also, when electrochemical cells, such as batteries and fuel cells, are incorporated into large-scale systems, efficient simulation is required to predict and control the system in real-time [103].

Various numerical approaches have been proposed to solve Laplace's equation, mitigating its mathematical/computational challenges. For example, steady-state heat transfer in solids, which is governed by Laplace's equation, has been solved by different kinds of numerical methods such as the successive over-relaxation method [104], the implicit alternative direction method [104], and the false transients method [105-108]. In the false transient method, a time derivative of the dependent variable was added to Laplace's equation, the Finite Difference Method (FDM) was used to approximate the spatial derivatives, and the resulting system of equations were solved by the Method Of Lines (MOL) [105-107, 109-112]. Also, a semi-analytical MOL was proposed for several examples of electrochemical cell systems [82]. This approach discretized second-order derivatives in one of the spatial directions using the FDM followed by solving the resulting system using the exponential matrix method to integrate analytically in one of the coordinates [82]. However, most of the past approaches might not be relevant to identify current distributions of electrochemical cell systems because they dealt with other applications of different configurations and boundary conditions (e.g., steady-state heat transfer) or used analytical solutions, which are limited to simple geometries. In this paper, therefore, we provide efficient numerical approaches that enable to predict current distributions of electrochemical cells with minimum computational costs. A direct numerical MOL approach is proposed, using a rectangular cell system, a hull cell system, and a coplanar thin-layer galvanic cell system (*see Figure 4.1*).

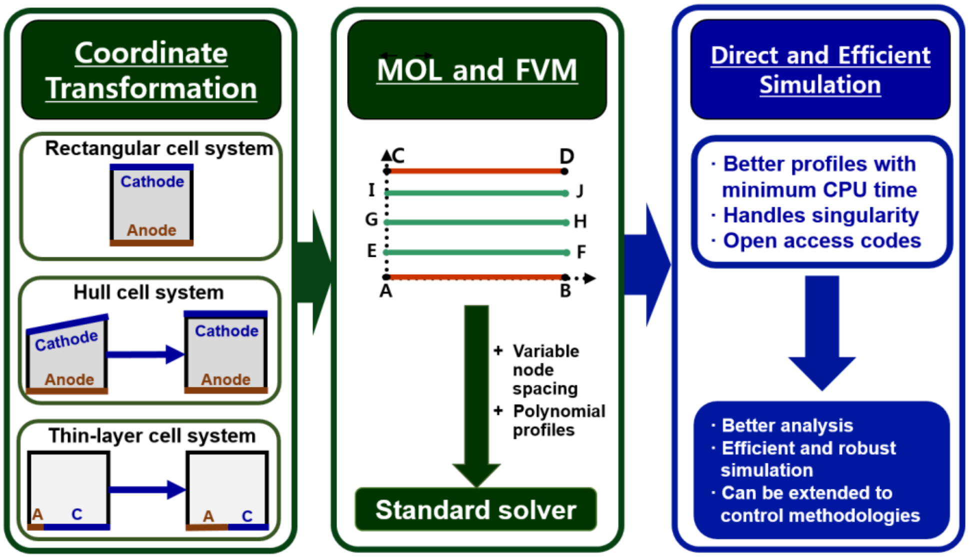

Figure 4.1. Fast and accurate approach to identifying current and potential distributions of electrochemical cell systems. The objective of this work is to provide an efficient and robust numerical approach for a rectangular cell, a hull cell, and a coplanar thin-layer galvanic cell, using the finite volume method. First, the coordinate of the cell system is scaled from 0 to 1, one dimension of the same is discretized using FVM, and polynomial profiles and variable node spacing are adopted for the adequate prediction, providing smooth profiles near boundaries. This approach is applicable to other cell structures and control methodologies.

4.2 METHOD

In this proposed approach, the MOL has been implemented, using the Finite Volume Method (FVM) [113]. Typically, the MOL has been used to solve two-dimensional equations by adding dummy derivatives. As of today, however, solvers have been developed to a point where the resulting two-point boundary value problems in one spatial direction can be directly and efficiently solved numerically (e.g., when the system is discretized in the other direction). It is possible to achieve higher-order approximations in the discretization of spatial derivatives without significant increases in the computational complexity. This technique has the broad applicability to physical and chemical systems modeled by PDEs.

The second derivative of the potential in one direction is cast into the FVM while retaining the second derivative in the other direction as it is. There are several advantages of FVM compared to FDM [114]; (i) FVM is straightforward to implement. (ii) While FDM solves differential form, FVM is a general solution technique for uniform and un-structured grids since it solves the integral form. (iii) FVM handles better discontinuities in Boundary Conditions (BC) compared to FDM. The MOL, which is a semi-discrete method, is a general way of solving Partial Differential Equations (PDEs) as a system of Ordinary Differential Equations (ODEs). The resulting system of ODEs is numerically solved with linear or non-linear boundary conditions of the system (e.g., primary or secondary current distributions), adopting a standard computational solver. This proposed approach is applied for three electrochemical cells.

First, we show a direct way to mathematically identify the current distribution (primary and secondary current distributions) of the rectangular cell. It can help understand more complicated cell architectures. For this, the comparison of current distributions between MOL and FDM, MOL and FVM, and Finite Element Method (FEM) obtained by COMSOL Multiphysics 5.0 is presented. Laplace's equation is discretized by using FDM and FVM in the y-direction and resulting variables are solved as a function of x-direction. While y-derivatives of Laplace's equation are discretized using FDM or FVM, the x-derivatives of Laplace's equation are utilized as ODEs.

Next, hull cell and thin-layer galvanic cell systems are presented as examples of other electrochemical cell structures. The same direct approach is adopt, using FVM, but the coordinate transformation is conducted for an efficient simulation [27] (*see Figure 4.1*). After that, the concept of variable node spacing or polynomial approximations close to the boundary of the system is introduced. The results obtained by several combinations of proposed approaches (e.g., variable node spacing with quadratic profile vs. constant node spacing with quadratic profiles) is compared to other cases, and a better approach is proposed in terms of computational costs and accuracy. For polynomial approximations, a higher order polynomial profile might can be implemented depending on the number of node points chosen, but a quadratic approximation was found to be good enough to identify the desired accuracy.

4.2.1 *Rectangular cell*

The rectangular cell includes two insulating walls (AC and BD), electrolytes, and two planar electrodes (anode and cathode) at opposite ends of the cell (AB and CD), which are perpendicular to both of two insulating walls, as shown in Figure 4.2.

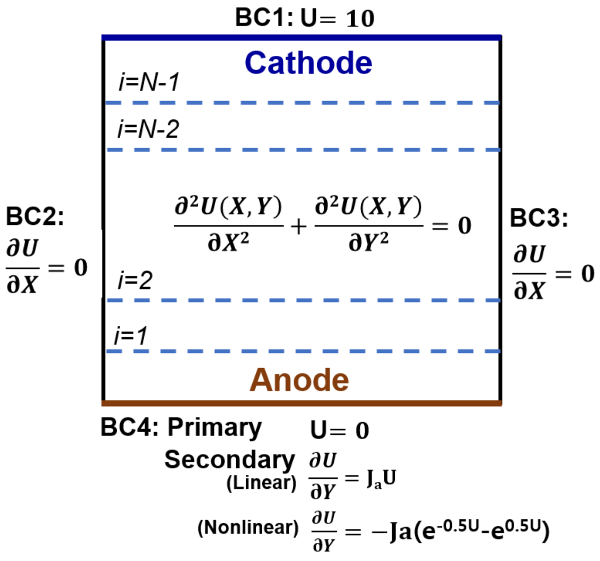

Figure 4.2. The rectangular cell system. The rectangular cell system is known to produce linear potential and current distribution profiles across the system. Also, there have been developed extensive applications based on this rectangular cell system. The proposed approach adopts the finite volume method and will start from this rectangular cell, comparing it to other numerical approaches such as finite difference and finite element methods.

4.2.1.1 Model and BCs

Consider a rectangular cell with dimensionless length ‘1’ (AB=CD=1) and height ‘1’ (AC=BD=1). The potential distribution, which is governed by the Laplace’s equation, is given as follow [100]:

$$\frac{\partial^2 U(X,Y)}{\partial X^2}+\frac{\partial^2 U(X,Y)}{\partial Y^2}=0 \tag{4.1.1}$$

in which U(X,Y) is the cell potential distribution, X is the cell length, and Y is the cell width. Also, Boundary Conditions (BCs) are given by follwing equations:

At X=0 and X=1 for $0 \le Y \le 1$,

$$\frac{\partial U(0,Y)}{\partial X}=0 \text{ and } \frac{\partial U(1,0)}{\partial X}=0 \tag{4.1.2}$$

At Y=0 for $0 \le X \le 1$ (BCs of anode),

$$U(X,0)=0 \text{ : Primary distribution} \tag{4.1.3}$$

$$\frac{\partial U(X,0)}{\partial Y}=J_a U(X,0) \tag{4.1.4}$$

: Linear kinetics (secondary distribution)

$$\frac{\partial U(X,0)}{\partial Y}=2J_a \sinh\left(\frac{U(X,0)}{2}\right) \tag{4.1.5}$$

: Non-linear kinetics (secondary distribution)

where J_a (=10A/m^2) is the polarization.[100]

At Y=1 for $0 \le X \le 1$,

$$U(X,0)=10 \tag{4.1.6}$$

4.2.1.2 Model and FDM

In this section, the governing equations, boundary conditions, and initial conditions are discretized using the MOL and the FDM. Figure 4.3(b) shows an example that how the FDM sets coordinates when the number of internal points is 4 (N=4). The subscript i presents ith order of nodes, and when N=4, the value i ranges from 0 to 5. The potential value on the ith node is Φ_i ,and the ith position of the coordinates is Y_i. For example, Y_i can be expressed as $Y_i=h_1+Y_{i-1}$ ($Y_0=0$). Also, the node spacing between the ith and (i-1)th nodes is presented as h_i . In the FDM, when the node spacing is constant ($h=h_i=h_{i-1}$), all node spacing values (h) equal to 1/ (N+1). Equations 4.1.1, 4.1.3, 4.1.4, 4.1.5, and 4.1.6 are expressed as Differential Algebraic Equations (DAEs) for internal states of the system, including system boundaries. Equation 4.1.2 is utilized as two boundary points of the cell system. Below is the detailed explanation.

4.2.1.2.1 For i=0.

There are three current distribution approximations at the anode: Primary, linear secondary, and non-linear secondary current distributions.

4.2.1.2.1.1 Primary approximation

Equation 1.7, which is obtained from Equation 4.1.3, is the primary current distribution at the anode.

$$U_0(X)=0 \text{: Primary approximation} \tag{4.1.7}$$

The subscript of the cell potential distribution (=i) represents the discretized order along Y direction (from 0 to N+1) of the cell system.

4.2.1.2.1.2 Linear secondary approximation

Equation 4.1.8 is the linear secondary current distribution at the anode, which is obtained from Equation 4.1.4.

$$\frac{\partial U_0(X)}{\partial Y} = J_a U_{anode}(X) \text{ : Linear secondary approximation} \quad (4.1.8)$$

The first order of Y-derivatives are discretized as follows:

$$\frac{\partial U_0(X)}{\partial Y} = \frac{U_1(X) - U_0(X)}{h} \quad (4.1.9)$$

Equation 1.8 is inserted into Equation 4.1.9.

$$\frac{U_1(X) - U_0(X)}{h} = J_a U_{anode}(X) = J_a U_0(X) \quad (4.1.10)$$

Equation 4.1.10, $U_0(X)$, can be expressed as a function of $U_1(X)$ as follows:

$$U_0(X) = \frac{U_1(X)}{h} \Bigg/ \left(J_a + \frac{1}{h} \right) \quad (4.1.11)$$

4.2.1.2.1.3 Non-linear secondary approximation

Equation 4.1.12 is the non-linear secondary current distribution at the anode, which is obtained from Equation 4.1.5.

$$\frac{\partial U_0(X)}{\partial Y} = 2J_a \sinh\left(\frac{U_{anode}(X)}{2} \right) \text{: Non-linear secondary approximation} \quad (4.1.12)$$

In the case of the primary and linear secondary current distribution approximations, boundary conditions, $U_0(x)$, can be expressed as a constant or a function of $U_1(x)$, and those can be inserted into internal discretized equations. In the case of the non-linear secondary approximation, however, this inserted solving process is not possible. Therefore, all equations should be solved at the same time. To do this, the non-linear secondary boundary condition is expressed as the second order X- and Y- derivatives to be discretized, as follows:

$$\frac{\partial^2 U_0(X)}{\partial X \partial Y} = J_a \frac{\partial U_0(X)}{\partial X} \cosh\left(\frac{U_{\mathrm{anode}}(X)}{2}\right) = J_a \frac{\partial U_0(X)}{\partial X} \cosh\left(\frac{U_0(X)}{2}\right) \qquad (4.1.13)$$

The second order of X- and Y-derivatives are discretized by the following equation.

$$\frac{\partial^2 U_0(X)}{\partial X \partial Y} = \frac{\dfrac{\partial U_1(X)}{\partial X} - \dfrac{\partial U_0(X)}{\partial X}}{h} \qquad (4.1.14)$$

Equation 4.1.15 is obtained by substituting Equation 4.1.13 into 4.1.14,

$$\frac{\dfrac{\partial U_1(X)}{\partial X} - \dfrac{\partial U_0(X)}{\partial X}}{h} = J_a \frac{\partial U_0(X)}{\partial X} \cosh\left(\frac{U_0(x)}{2}\right) \qquad (4.1.15)$$

4.2.1.2.2 For i from 1 to N.

The second order Y-derivatives of Laplace's equation are discretized using the FDM by a following equation [113]:

$$\frac{\partial^2 U(X,Y)}{\partial Y^2} = \frac{U_{i+1}(X) - 2U_i(X) + U_{i-1}(X)}{h^2}, \qquad i = 1..N \qquad (4.1.16)$$

Substituting Equation 4.1.16 into 4.1.1, Laplace's equation becomes:

$$\frac{d^2 U_i(X)}{dX^2} + \frac{U_{i+1}(X) - 2U_i(X) + U_{i-1}(X)}{h^2} = 0, \qquad i = 1..N \qquad (4.1.17)$$

4.2.1.2.3 For i=N+1.

Equation 4.1.18 is obtained from Equation 4.1.6, which is the cathode boundary condition.

$$U_{N+1}(X) = 10 \qquad (4.1.18)$$

4.2.1.2.4 Solving process with two boundary points

Boundary conditions for two insulating walls (Equations 4.1.2) are utilized as two boundary points in this ODE system (see Equations 4.1.19).

$$\frac{\partial \mathrm{U_i}(0)}{\partial \mathrm{X}} = 0 \text{ and } \frac{\partial \mathrm{U_i}(1)}{\partial \mathrm{X}} = 0, \quad i = 1..N \tag{4.1.19}$$

Discretized governing equations are solved with given boundary conditions of anode and cathode and two boundary points, using a general DAE solver in the Maple software. For primary approximations, Equations 4.1.7, 4.1.17, 4.1.18, and 4.1.19 are solved. For secondary linear and non-linear approximations, Equations 4.1.11, 4.1.17, 4.1.18, and 4.1.19, and Equations 4.1.15, 4.1.17, 4.1.18, and 4.1.19 are used, respectively.

4.2.1.3 Model and FVM

In this section, the FVM is utilized to substitute the second order derivatives of Laplace’s equation in the Y-direction. Figure 4.3(a) describes the FVM coordinate and compares the FVM coordinate with the FDM coordinate. For example, when the number of FDM internal nodes is 4, the number of FVM internal nodes is 5 (N´=5), and the FVM includes imiginary points beyond or before its boundaries (see Φ'_0 and Φ'_6). Likewise the FDM coordinate, the subscript i presents the ith order of nodes, but in the FVM coordinate, when N´=n, the value i ranges from 0 to n+1 (e.g., when n=5, i ranges from 0 to 6). The potential value on the i^th node is expressed as Φ'_i and the value is located in the middle of Φ_{i-1} and Φ_{i+1} in the FDM coordinate. In the one-dimensional coordinate of the FVM, Φ'_i can be expressed as a function of $(\Phi'_{i-1} + \Phi'_{i+1})/2$. Also, the i^th position of the coordinates can be expressed as $Y_i = h'_i/2 + Y_{i-1}$ ($Y_1 = h_1/2$).

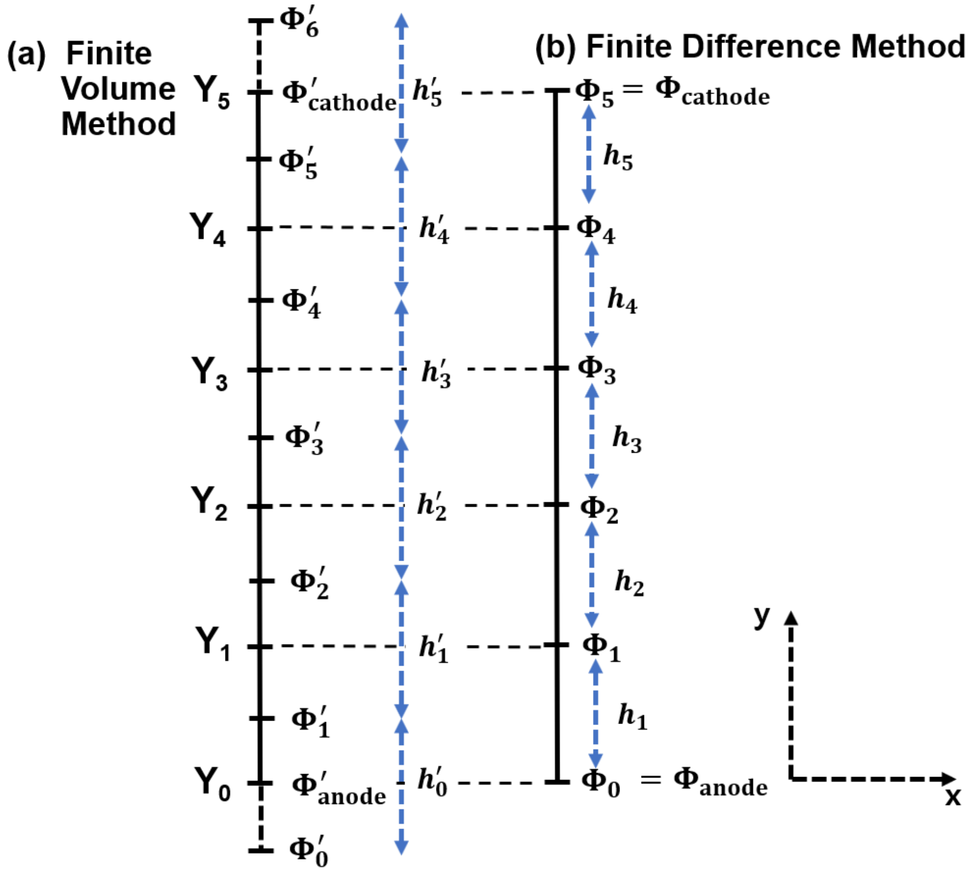

Figure 4.3. The comparison of the 1-D coordinate between finite difference and finite volume methods. The potential values (Φ_i and Φ'_i), the node spacing (h_i and h'_i), and the coordinate position (Y_i) are described on the 1-D coordinate of the finite difference and finite volume method. In the 1-D coordinate, potential profiles of Φ'_i in the FVM is located in the middle of Φ_{i-1} and Φ_{i+1} in the FDM, and the 1-D coordinate has the linear profile, Φ'_i can be expressed as $(\Phi_{i-1}+\Phi_{i+1})/2$. Therefore, Φ'_{anode} can be calculated by $(\Phi'_0+\Phi'_1)/2$.

4.2.1.3.1 For i=0.

The same three current distribution approximations (primary, secondary linear, and secondary non-linear approximations) are used.

4.2.1.3.1.1 Primary approximation

Equation 4.1.7 is used as the primary current distribution at the anode.

4.2.1.3.1.2 Linear secondary approximation

For the constant node spacing in the FVM**,** the first order of Y-derivatives are discretized as follows:

$$\frac{\partial U(X,Y)}{\partial Y} = \frac{U_1(X) - U_0(X)}{\frac{h_1}{2} + \frac{h_0}{2}} = \frac{U_1(X) - U_0(X)}{\frac{h}{2} + \frac{h}{2}} \tag{4.1.20}$$

Equation 4.1.22 is obtained by substituting Equation 1.8 and $U_{anode}(X)=(U_0(X) +U_1(X))/2$ into Equation 4.1.21. In the FDM, $U_{anode}(X)$ equals to $U_0(X)$, but in the FVM, $U_{anode}(X)$ is expressed as $(U_0(X) +U_1(X))/2$.

$$\frac{U_1(X) - U_0(X)}{h} = J_a\left(U_{anode}(X)\right) = J_a\left(\frac{U_0(X) + U_1(X)}{2}\right) \tag{4.1.21}$$

Equation 4.1.23, $U_0(X)$, can be expressed as a function of $U_1(X)$ as follows:

$$U_0(X) = -U_1(X)\frac{(J_a h - 2)}{(J_a h + 2)} \tag{4.1.22}$$

4.2.1.3.1.3 Non-linear secondary approximation

For constant node spacing in the FVM, the second order of X- and Y-derivatives are discretized by the following equation.

$$\frac{\partial^2 U(X,Y)}{\partial X \partial Y} = \frac{\frac{\partial U_1(X)}{\partial X} - \frac{\partial U_0(X)}{\partial X}}{\frac{h_1}{2} + \frac{h_0}{2}} = \frac{\frac{\partial U_1(X)}{\partial X} - \frac{\partial U_0(X)}{\partial X}}{\frac{h}{2} + \frac{h}{2}} \tag{4.1.23}$$

Equation 4.1.25 is obtained by substituting Equation 4.1.13 and $U_{anode}(X)= (U_0(X) +U_1(X))/2$ into Equation 4.1.24,

$$\frac{\frac{\partial U_1(X)}{\partial X}-\frac{\partial U_0(X)}{\partial X}}{h}=J_a\frac{\partial U_0(X)}{\partial X}\cosh\left(U_{anode}(X)\right)=J_a\frac{\partial U_0(X)}{\partial X}\cosh\left(\frac{U_0(X)+U_1(X)}{2}\right) \quad (4.1.24)$$

4.2.1.3.2 For i from 1 to N.

The second order Y-derivative of Laplace’s equation is discretized using the FVM by a following equation:

$$\frac{\partial^2 U(X,Y)}{\partial Y^2}=\frac{U_{i+1}(X)-U_i(X)}{h_i\left(\frac{h_{i+1}}{2}+\frac{h_i}{2}\right)}-\frac{U_i(X)-U_{i-1}(X)}{h_i\left(\frac{h_i}{2}+\frac{h_{i-1}}{2}\right)}, \quad i=1..N \quad (4.1.25)$$

Substituting Equation 4.1.26 into Equation 4.1.1, Laplace’s equation becomes as follows:

$$\frac{d^2U_i(X)}{dX^2}+\frac{U_{i+1}(X)-U_i(X)}{h_i\left(\frac{h_{i+1}}{2}+\frac{h_i}{2}\right)}-\frac{U_i(X)-U_{i-1}(X)}{h_i\left(\frac{h_i}{2}+\frac{h_{i-1}}{2}\right)}=0, \quad i=1..N \quad (4.1.26)$$

4.2.1.3.3 For i=N+1.

Equation 4.1.18 is used as the cathode boundary condition.

4.2.1.3.4 Solving process with two boundary points

Equations 4.1.19 is adopted as two boundary points. Therefore, Equations 4.1.7, 4.1.26, 4.1.18, and 4.1.19, Equations 4.1.22, 4.1.26, 4.1.18, and 4.1.19, and Equations 4.1.24, 4.1.26, 4.1.18, and 4.1.19 are solved for primary, secondary linear, and secondary non-linear approximations, respectively, using a general DAE solver in the Maple software.

4.2.1.4 Results

Figure 4.4 shows the potential and current distribution profiles along X- and Y-axis of the rectangular cells generated by the FVM, the FVM, and the FEM obtained by COMSOL. A simple

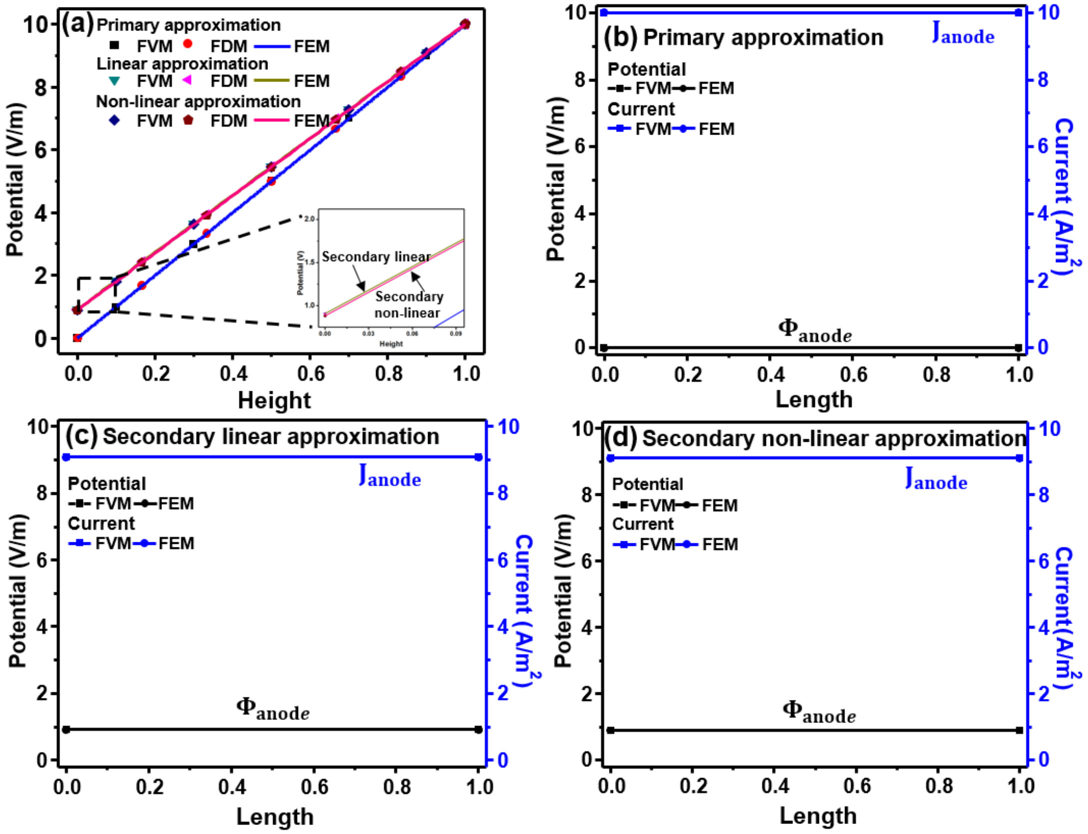

Figure 4.4. The comparison of potential and current distributions between the Finite Volume Method (FDM), the Finite Volume Method (FVM), and the Finite Element Method (FEM) obtained by COMSOL in the rectangular system. (a) Potential distribution of primary, secondary linear, and secondary non-linear approximations along y-axis (height) of the cell system and Potential and current distributions with (b) primary current approximations (c) secondary linear approximations, and (d) non-linear current approximations. The FDM and FVM produce the same linear and symmetric profiles as the results of the FEM, with a lower number of nodes (See Table II).

rectangular cell generates a linear and uniform profile across the entire cell. Figure 4.4a shows a comparison of the potential profiles along the height of the cell between the FDM, the FVM, and the FEM when the number of nodes (N) is 5. Figure 4.4b, 4.4c, and 4.4d show the potential and current distributions generated by the FVM and the FEM with the primary, secondary linear, and secondary non-linear approximations, respectively (when N=5). When the number of nodes becomes lower, the simulation consumes less computational costs (see Table 4.2), but accuracy is not affected by the number of nodes and numerical methods.

Table 4.2. Comparison of computational time in rectangular cell

Method	Number of nodes	Current distribution	Number of DAE	CPU time (s)	RSME	Software
FDM	N=2	Primary	2	0.109	0	Maple
		linear	2	0.078	0	
		Non-linear	3	0.218	0	
	N=5	Primary	5	0.109	0	
		Linear	5	0.109	0	
		Non-linear	6	0.234	0	
	N=10	Primary	10	0.140	0	
		Linear	10	0.156	0	
		Non-linear	11	0.234	0	
FVM	N=2	Primary	2	0.094	0	Maple
		Linear	2	0.093	0	
		Non-linear	2	0.936	0	
	N=5	Primary	5	0.093	0	
		Linear	5	0.094	0	
		Non-linear	6	1.778	0	
	N=10	Primary	10	0.156	0	
		Linear	10	0.125	0	
		Non-linear	11	0.359	0	
FEM	N/A	Primary	N/A	1s	0	COMSOL
		Linear	N/A	4s	0	
		Non-linear	N/A	2s	0	

4.2.2 Hull cell

The Hull cell, an electroplating test cell enabling to determine the “throwing power”, has been used to qualitatively identify how irregular deposits form on electrodes of the cell [100]. The cell forms non-uniform deposits caused by different current densities along the surface of electrodes [100]. The Hull cell consists of two insulating walls, electrolytes, and two planar electrodes at opposite ends of the cell; the anode is perpendicular to both of two insulating walls and the cathode is at an angle with one of the two insulating walls [83]. The original cell schematic, governing equations, and boundary conditions are described in Figure 4.5. The coordinate transformed cell schematic, governing equations, and boundary conditions are presented in Figure 4.6.

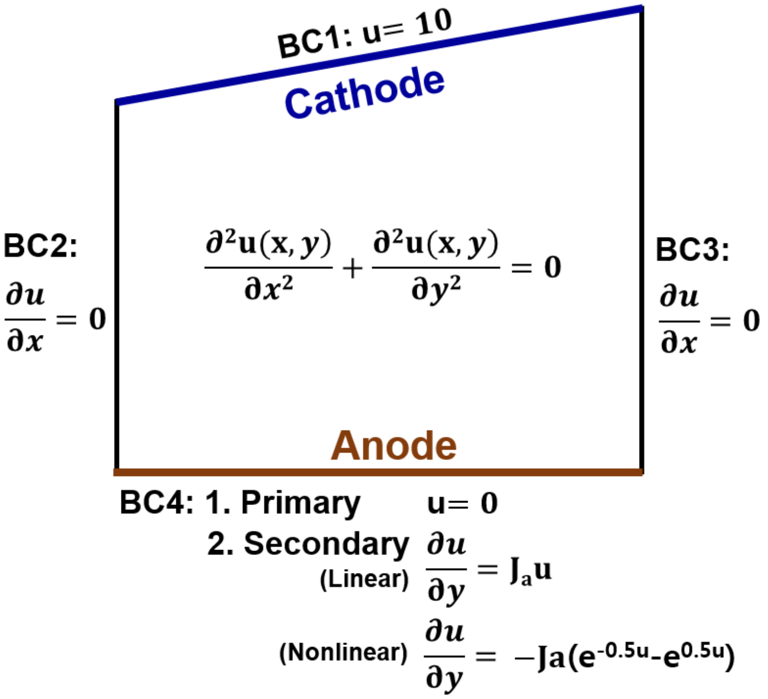

Figure 4.5. The original Hull cell system. The tilted cathode brings non-uniform potential and current distributions, and the Hull cell is presented as an example of different electrodes geometries.

4.2.2.1 Model and BCs

The potential distribution of the Hull Cell, which is governed by Laplace's equation, is expressed as below [83]:

$$\frac{\partial^2 u(x,y)}{\partial x^2}+\frac{\partial^2 u(x,y)}{\partial y^2}=0 \tag{4.2.1}$$

At y=1+0.5x for 0≤ x≤ 1 (BC of the cathode),

$$u(0,1+0.5x)=10 \tag{4.2.2}$$

In the Hull cell, we assume that the length (x) and width (y) of the cathode follow the relation of y=1+0.5x.

At x=0 and x=1 for 0≤ y(=1+0.5x) ≤ b (BCs of insulating walls),

$$\frac{\partial u(0,y)}{\partial x}=0 \text{ and } \frac{\partial u(1,y)}{\partial x}=0 \tag{4.2.3}$$

At y=0 for 0≤ x ≤ 1 (BCs of anode),

$$u(x,0)=0 \text{: Primary distribution} \tag{4.2.4}$$

$$\frac{\partial u(x,0)}{\partial y}=J_a u(x,0) \tag{4.2.5}$$

: linear kinetics (secondary distribution)

$$\frac{\partial u(x,0)}{\partial y}=-J_a(e^{-0.5u(x,0)}-e^{0.5u(x,0)}) \tag{4.2.6}$$

: non-linear kinetics (secondary distribution)

where J_a (=10A/m^2)is the polarization.[100]

4.2.2.2 Coordinate transformation

The coordinate transformation of X=x, U=u, and Y=y/ (1+0.5x) are inserted into Equations 4.2.1-4.2.6, and coordinate transformed Laplace's equations are presented as follow:

$$\frac{\partial^2 U(X,Y)}{\partial X^2}+\frac{(1+0.25Y^2)}{(1+0.5X)^2}\frac{\partial^2 U(X,Y)}{\partial Y^2}-\frac{Y}{(1+0.5X)}\frac{\partial^2 U(X,Y)}{\partial Y\partial X}+\frac{0.5Y}{(1+0.5X)^2}\frac{\partial U(X,Y)}{\partial Y}=0 \tag{4.2.7}$$

At Y=1 for 0≤X≤1 (BC of the cathode),

$$U(X,1)=10 \tag{4.2.8}$$

At X=0 and X=1 for 0≤Y≤1 (BC of insulating walls),

$$\frac{\partial U(0,Y)}{\partial X}=\frac{0.5Y}{(1+0.5X)}\frac{\partial U(0,Y)}{\partial Y} \quad \text{and} \quad \frac{\partial U(1,Y)}{\partial X}=\frac{0.5Y}{(1+0.5X)}\frac{\partial U(1,Y)}{\partial Y} \tag{4.2.9}$$

At Y=0 for 0≤X≤1 (BC of anode), for primary current distribution,

$$U(X,0)=0 \tag{4.2.10}$$

, for the secondary distribution approximation,

$$\frac{\partial U(X,0)}{\partial Y}=J_a(1+0.5X)\,U(X,0) : \text{linear kinetics} \tag{4.2.11}$$

$$\frac{\partial U(X,0)}{\partial Y}=-J_a(1+0.5X)(e^{-0.5U(X,0)}-e^{0.5U(X,0)}) : \text{non-linear kinetics} \tag{4.2.12}$$

4.2.2.2.1 MOL and FVM

The transformed Laplace's equation is discretized by using the FVM along the Y-direction and the resulting variables are solved as a function of X-direction, as shown in Figure 4.6.

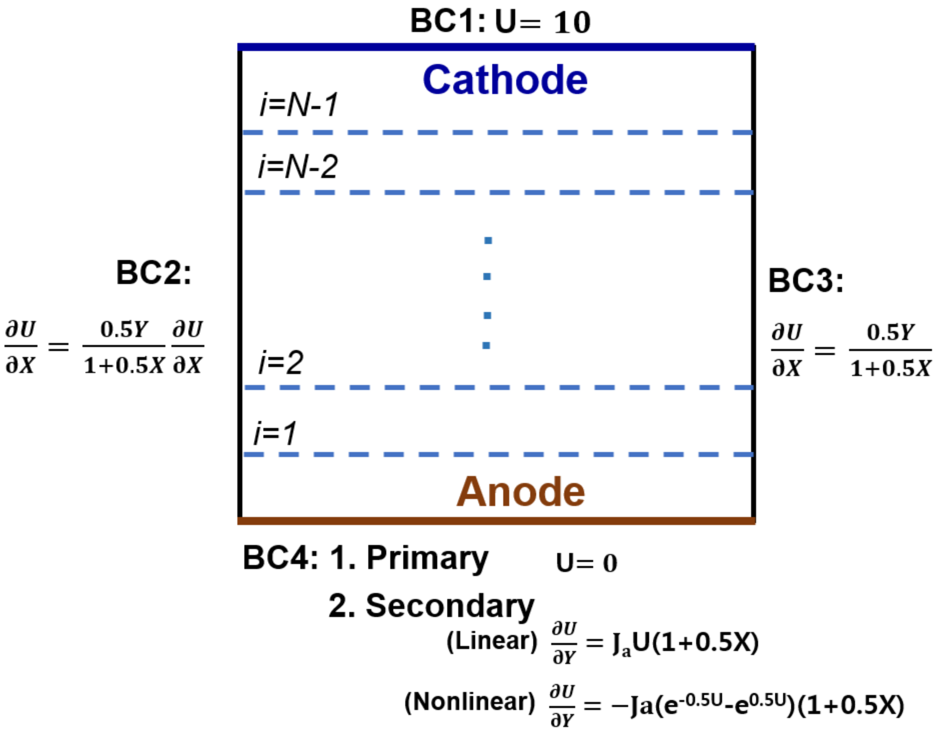

Figure 4.6. The reformulated Hull cell system. The Hull system is scaled from 0 to 1 for both length and height. This will enable the system to be solved efficiently.

4.2.2.2.1.1 For i=0

Equations 4.2.13, 4.2.14, and 4.2.15 are obtained from Equation 4.2.10, 4.2.11, and 4.2.12, respectively.

$$U_0(X) = 0 \quad \text{(Primary current distribution)} \qquad (4.2.13)$$

$$\frac{\partial U_0(X)}{\partial Y} = J_a(1+0.5X)\,U_0(X) \quad \text{(Secondary linear current distribution)} \qquad (4.2.14)$$

$$\frac{\partial U_0(X)}{\partial Y} = -J_a(1+0.5X)(e^{-0.5U_0(X)} - e^{0.5U_0(X)}) \quad \text{(Secondary non-linear current distribution)} \; (4.2.15)$$

4.2.2.2.1.2 For i from 1 to N.

The second order of *Y*-derivatives are discretized by the following set of equations.

$$\frac{\partial^2 U(X,Y)}{\partial Y^2} = \frac{U_{i+1}(X) - U_i(X)}{h_i\left(\frac{h_{i+1}}{2} + \frac{h_i}{2}\right)} - \frac{U_i(X) - U_{i-1}(X)}{h_i\left(\frac{h_i}{2} + \frac{h_{i-1}}{2}\right)} \quad i = 1..N-1 \quad (4.2.16)$$

$$\frac{\partial U(X,Y)}{\partial Y} = \frac{U_i(X) - U_{i-1}(X)}{\frac{h_i}{2} + \frac{h_{i-1}}{2}} \quad i = 2..N-1 \quad (4.2.17)$$

$$\frac{\partial^2 U(X,Y)}{\partial Y \partial X} = \frac{\frac{dU_i(X)}{dX} - \frac{dU_{i-1}(X)}{dX}}{\left(\frac{h_i}{2} + \frac{h_{i-1}}{2}\right)} \quad i = 2..N-1 \quad (4.2.18)$$

Substituting Equations 4.2.16-4.2.18 to 4.2.7, Laplace’s equation is expressed as:

$$\frac{d^2U_i(X)}{dX^2} + \frac{(1+0.25Y_i^2)}{(1+0.5X)^2}\frac{U_{i+1}(X) - U_i(X)}{h_i\left(\frac{h_{i+1}}{2} + \frac{h_i}{2}\right)} - \frac{U_i(X) - U_{i-1}(X)}{h_i\left(\frac{h_i}{2} + \frac{h_{i-1}}{2}\right)} - \frac{Y_i}{(1+0.5X)}\frac{\frac{dU_i(X)}{dX} - \frac{dU_{i-1}(X)}{dX}}{\left(\frac{h_i}{2} + \frac{h_{i-1}}{2}\right)} + \frac{0.5Y_i}{(1+0.5X)^2}\frac{U_i(X) - U_{i-1}(X)}{\left(\frac{h_i}{2} + \frac{h_{i-1}}{2}\right)} = 0$$

$$(4.2.19)$$

in which Y_i is the variable distances.

4.2.2.2.1.3 i=N+1

Equation 4.2.20 is obtained from Equation 4.2.8, which is the cathode boundary condition.

$$U_{N+1}(X) = 1 \quad (4.2.20)$$

4.2.2.2.1.4 Solving process with two boundary condition points

Boundary conditions for two insulating walls (Equations 4.2.9) are utilized as initial conditions in this ODE system (see Equations 4.2.21).

$$\frac{\partial U_i(0)}{\partial X} = 0.5Y_i\frac{\partial U_i(0)}{\partial Y} \text{ and } \frac{\partial U_i(1)}{\partial X} = 0.5Y_i\frac{\partial U_i(1)}{\partial Y} \quad i = 1..N \quad (4.2.21)$$

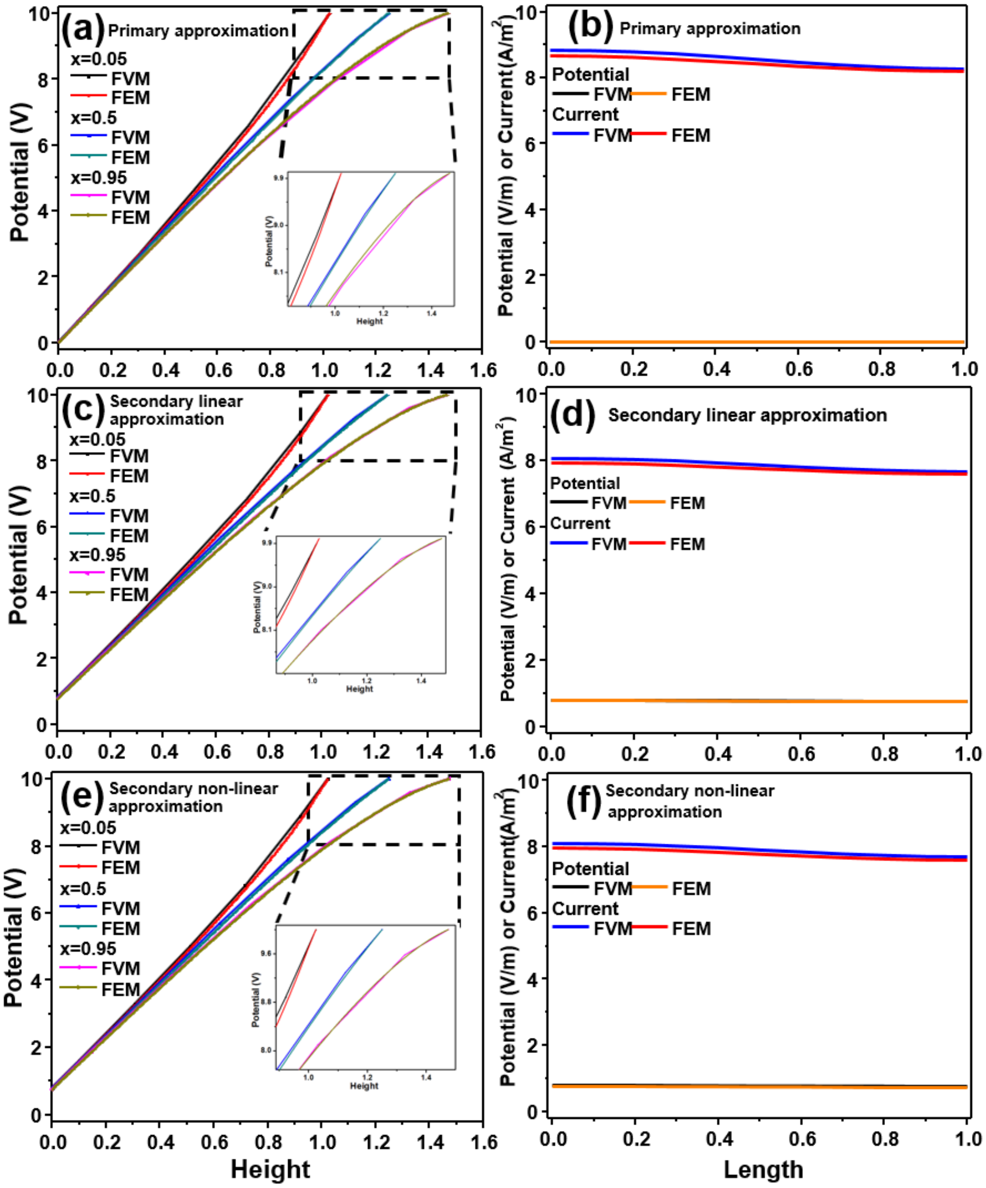

Figure 4.7. Comparison of potential distribution with constant nodes. When x=0.05, x=0.5, and x=0.95, (a) Primary current distribution (c) Secondary linear current distribution (e) Secondary non-linear current distribution along with y-axis. When y=0.5, (b) Primary current distribution (d) Secondary linear current distribution, and (d) Secondary non-linear current distribution.

Discretized governing equations are solved with given boundary conditions of anode and cathode and two boundary condition points, using a general DAE solver in the Maple software. For primary approximations, Equations 4.2.13, 4.2.19, and 4.2.20 are solved. For secondary linear and non-linear approximations, Equations 4.2.14, 4.2.19, and 4.2.20 and Equations 4.2.15, 4.2.19, and 4.2.20 are used, respectively.

4.2.2.2.1.5 Results

Figure 4.7 shows potential and current distributions in the Hull cell for primary, secondary linear, and secondary non-linear boundary conditions at J_a=10. Figure 4.7a,4.7c, and 4.7e present potential and current distribution along with the height of the cell generated by primary, secondary linear, and secondary non-linear approximations. Figure 4.7b, 4.7d, and 4.7f present potential distributions along the length of the cell. Profiles near boundaries are not smooth for primary, secondary linear, and secondary non-linear approximations, accuracy of the same is required to be improved. To mitigate this issue, in the next section, we adopt polynomial approximations near boundaries of the system.

4.2.2.2.2 MOL and FVM with quadratic profiles

In this section, we introduce polynomial profiles to improve accuracy of near boundaries of the system and minimize computational costs.

4.2.2.2.2.1 For i=0

Equations 4.2.13, 4.2.14, and 4.2.15 are used.

4.2.2.2.2.2 For i=1.

$$U(X,Y)=a+bY+cY^2 \tag{4.2.22}$$

$$U_0(X)=a=U_0(X) \tag{4.2.23}$$

$$U_1(X) = a + b\left(\frac{h_1}{2}\right) + c\left(\frac{h_1}{2}\right)^2 \tag{4.2.24}$$

$$U_2(X) = a + b\left(h_1 + \frac{1}{2}h_2\right) + c\left(h_1 + \frac{1}{2}h_2\right)^2 \tag{4.2.25}$$

By solving Equations 4.2.22-4.2.25, the coefficients of the polynomial approximation (a, b, and c) can be expressed as a function of $U_0(X)$, $U_1(X)$, and $U_2(X)$ as follows:

$$a = 0 \tag{4.2.26}$$

$$b = \frac{2(U_2(x)h_1^2 - 4U_1(x)h_1^2 - 4U_1(x)\,h_1h_2 - U_1(x)h_2^2)}{(2h_1^2 + 3h_1h_2 + h_2^2)} \tag{4.2.27}$$

$$c = \frac{4(U_2(x)h_1 - 2U_1(x)h_1 - U_1(x)\,h_2)}{(2h_1^2 + 3h_1h_2 + h_2^2)\,h_1} \tag{4.2.28}$$

By substituting Equations 4.2.26, 4.2.27, and 4.2.28, potential distribution near boundaries of the system can be identified.

4.2.2.2.2.3 For i from 2 to N-1

Equation 4.2.23 is used.

4.2.2.2.2.4 For i=N

Following equations (4.2.24-4.2.26) are solved by using the quadratic approximation (Equations 4.2.16) and the boundary condition of the cathode (Equation 4.2.8).

$$U_{N+1}(X) = a + b + c = 1 \tag{4.2.29}$$

$$U_N(X) = a + b\left(1 - \frac{1}{2}h_N\right) + c\left(1 - \frac{1}{2}h_N\right)^2 \tag{4.2.30}$$

$$U_{N-1}(x) = a + b\left(1 - h_N - \frac{1}{2}h_{N-1}\right) + c\left(1 - h_N - \frac{1}{2}h_{N-1}\right)^2 \tag{4.2.31}$$

Coefficients of the quadratic approximations (a, b, and c as a function of $U_0(X)$, $U_1(X)$, and $U_2(X)$) can be identified by solving Equations 4.2.29, 4.2.30, and 4.2.31, and the second order Y-derivates at the Nth node point can be obtained as follows:

$$\frac{d^2U_N(X)}{dY^2} = -\frac{8(h_N U_{N-1}(X) - h_{N-1}U_N(X) - 2h_N U_N(X) + h_{N-1} + h_N)}{h_N(2h_N^2 + 3h_N h_{N-1} + h_{N-1}^2)} \tag{4.2.32}$$

4.2.2.2.2.5 For i=N+1

Equation 4.2.20 is used.

4.2.2.2.2.6 Results

Potential distribution in the Hull cell for primary, secondary linear, and secondary non-linear approximations at J_a=10 case is shown in Figure 4.8. Figure 4.8a, 4.8c, and 4.8e present potential distribution along with the height of the cell generated by primary, secondary linear, and secondary non-linear approximations. Figure 4.8b, 4.8d, and 4.8f present potential distributions along the length of the cell. Profiles near boundaries are generating smooth profiles near cathode boundaries. Such a discretization allows to get converged results in lesser total node points compared to other approaches including FDM and FEM generated by COMSOL.

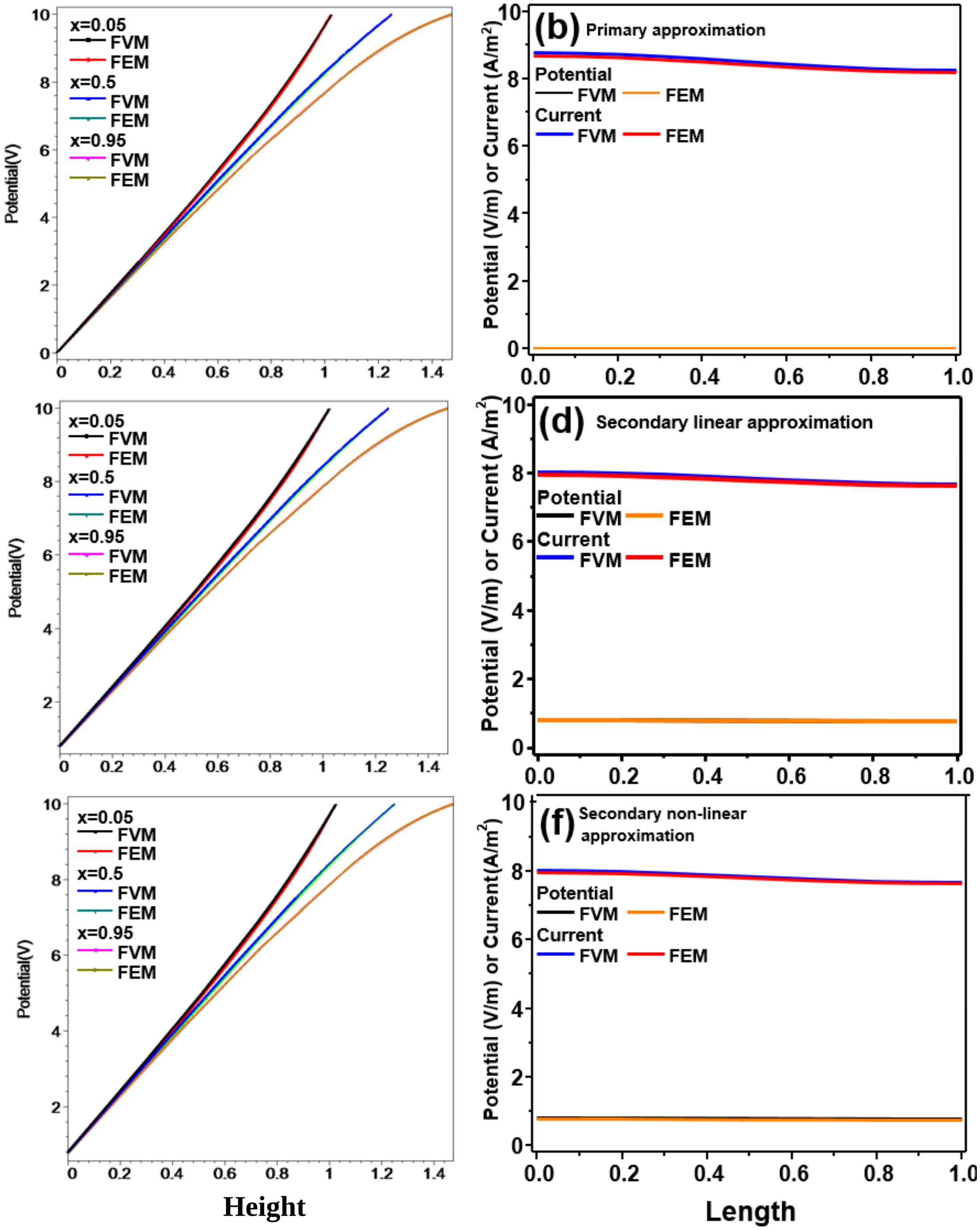

Figure 4.8. Comparison of potential distribution with constant nodes with quadratic profiles. When x=0.05, x=0.5, and x=0.95, (a) Primary current distribution (c) Secondary linear current distribution (e) Secondary non-linear current distribution along with y-axis. When y=0.5, (b) Primary current distribution (d) Secondary linear current distribution, and (d) Secondary non-linear current distribution.

Table 4.3. Comparison of computational time in the Hull cell with constant node and constant node with quadratic profiles

Method	Number of Nodes		Number of DAE	CPU time (s)	RMSE (V)	Software
FVM + constant node	N=3	Primary	3	0.125	0.099	Maple
		Linear	3	0.125	0.104	
		Non-linear	4	0.468	0.104	
	N=5	Primary	5	0.140	0.061	
	N=5	Linear	5	0.125	0.062	
	N=10	Non-linear	6	1.982	0.062	
		Primary	10	0.234	0.041	
	N=10	Linear	10	0.203	0.031	
	N=20	Non-linear	11	0.577	0.031	
		Primary	20	0.811	0.036	
	N=20	Linear	20	0.468	0.015	
FVM + constant node +quadratic profile	N=3	Non-linear	21	1.263	0.015	
		Primary	3	0.094	0.054	Maple
	N=3	Linear	3	0.125	0.052	
FVM + constant node +quadratic profile	N=5	Non-linear	4	0.078	0.059	
		Primary	5	0.172	0.039	
	N=5	Linear	5	0.172	0.038	
	N=10	Non-linear	6	0.094	0.046	
		Primary	10	0.234	0.025	Maple
	N=10	Linear	10	0.234	0.024	
FVM+ variable+ quadratic profile	N=20	Non-linear	11	0.171	0.032	
		Primary	20	0.499	0.013	
	N=20	Linear	20	0.515	0.013	
	N=3	Non-linear	21	0.593	0.021	
		primary			0.046	
	N=10				0.032	
	N=20				0.019	
		linear				
		Primary	N/A	2	N/A	COMSOL
FEM		Linear	N/A	1	N/A	
		Non-linear	N/A	2	N/A	

4.2.3 Thin-layer galvanic cell

Cell schematic, governing equations, boundary conditions are presented as shown in Figure 4.9 [84].

4.2.3.1 Governing equation

The potential distribution of a thin-layer galvanic cell, which is governed by Laplace's equation, is presented as below:

$$\varepsilon^2 \frac{\partial^2 u_a(\mathrm{x,y})}{\partial x^2} + \frac{\partial^2 u_a(\mathrm{x,y})}{\partial y^2} = 0 \tag{4.3.1}$$

$$\varepsilon^2 \frac{\partial^2 u_c(\mathrm{x,y})}{\partial x^2} + \frac{\partial^2 \Phi_c(\mathrm{x,y})}{\partial y^2} = 0 \tag{4.3.2}$$

where $u_a(x,y)$ is the potential in the anode region, $u_c(x,y)$ is the potential in the cathode region, x and y are the length and width of the cell, respectively. Boundary conditions are as follows:

At $y=0$ for 0 $0 \le x \le a$ (Anode boundary condition) :

$$\frac{\partial u_a(\mathrm{x,0})}{\partial y} = J_a \varepsilon^2 u_a(\mathrm{x,0}) \tag{4.3.3}$$

where J_a is the anode polarization.

At $y=0$ for $a \le x \le 1$ (Cathode boundary condition) :

$$\frac{\partial u_c(\mathrm{x,0})}{\partial y} = J_c \varepsilon^2 \left(u_c(\mathrm{x,0}) - 1\right) \tag{4.3.4}$$

where J_c is the cathode polarization.

At $x=0$ and $x=1$ for $0 \le y \le 1$ (Insulating boundary conditions),

$$\frac{\partial u_a(0,\mathrm{y})}{\partial x} = 0 \text{ and } \frac{\partial u_c(1,\mathrm{y})}{\partial x} = 0 \tag{4.3.5}$$

At $y=1$ for $0 \le x \le a$ and $a \le x \le 1$ (Anode boundary condition)

$$\frac{\partial u_a(\mathrm{x,1})}{\partial x} = 0 \text{ and } \frac{\partial u_c(\mathrm{x,1})}{\partial x} = 0 \tag{4.3.6}$$

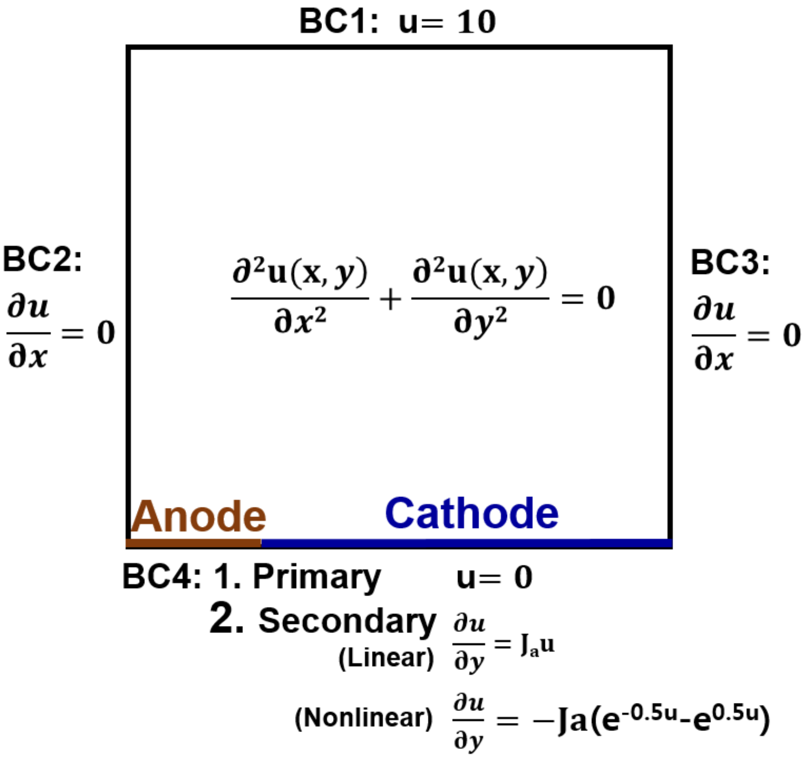

Figure 4.9. The original coplanar thin-layer galvanic cell system

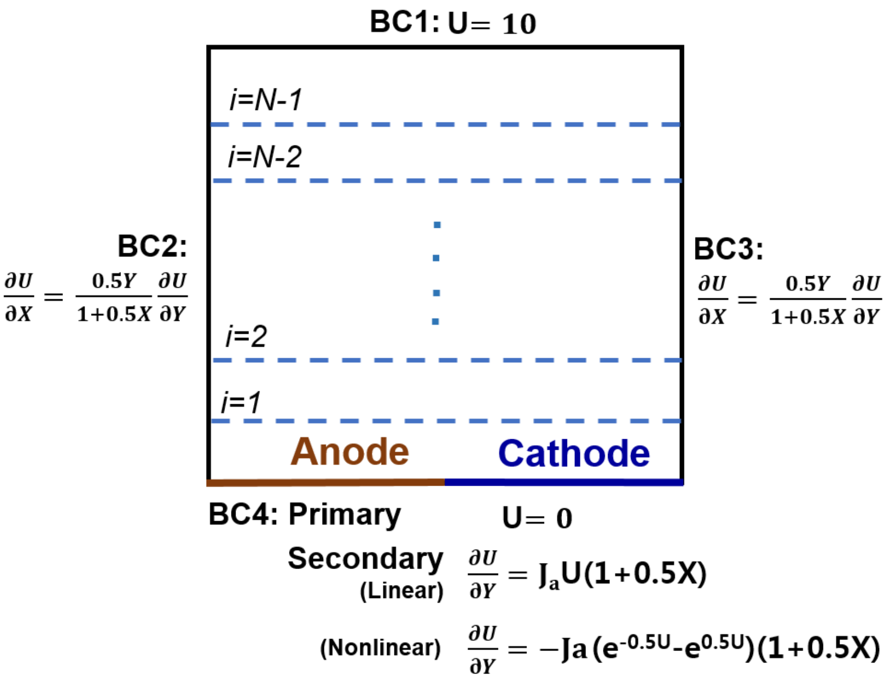

Figure 4.10. The reformulated coplanar thin-layer galvanic cell system.

4.2.3.2 Coordinate transformation

Galvanic cell equations are transformed into a dimensionless scale using the following transformation equations, one each for anode (Equation 4.3.7) and cathode (Equation 4.3.8), respectively:

$$X = \frac{x}{a} \qquad 0 \le X \le a \tag{4.3.7}$$

$$X = \frac{x-a}{1-a} \qquad a \le X \le 1 \tag{4.3.8}$$

$$Y = y \qquad 0 \le Y \le 1 \tag{4.3.9}$$

Based on the above transformation equations, Laplace's equation (4.3.1 and 4.3.2) is transformed into the following equations, one for anode (4.3.10) and (4.3.11):

$$\frac{\varepsilon^2}{a^2}\frac{\partial^2 U_a(\mathrm{X,Y})}{\partial X^2} + \frac{\partial^2 U_a(\mathrm{X,Y})}{\partial Y^2} = 0 \tag{4.3.10}$$

$$\frac{\varepsilon^2}{(1-a)^2}\frac{\partial^2 U_c(\mathrm{X,Y})}{\partial X^2} + \frac{\partial^2 U_c(\mathrm{X,Y})}{\partial Y^2} = 0 \tag{4.3.11}$$

At $Y = 0$ for $0 \le X \le 1$ (Anode boundary condition),

$$\frac{\partial U_a(\mathrm{X,Y})}{\partial Y} = J_a \varepsilon^2 U_a(\mathrm{X,Y}) \tag{4.3.12}$$

At $Y = 0$ for $0 \le X \le 1$ (Cathode boundary),

$$\frac{\partial U_c(\mathrm{X,Y})}{\partial Y} = J_c \varepsilon^2 \left(U_c(\mathrm{X,Y}) - 1\right) \tag{4.3.13}$$

At $X = 0$ and $X = 1$ for $0 \le Y \le 1$ (Insulating boundary conditions),

$$\frac{\partial U_a(\mathrm{X,Y})}{\partial Y} = 0 \text{ and } \frac{\partial U_c(\mathrm{X,Y})}{\partial Y} = 0 \tag{4.3.14}$$

At $Y = 1$ for $0 \le X \le 1$ (Insulating boundary conditions)

$$\frac{\partial U_a(\mathrm{X,Y})}{\partial Y} = 0 \text{ and } \frac{\partial U_c(\mathrm{X,Y})}{\partial Y} = 0 \tag{4.3.15}$$

At the interface of the anode and cathode boundary,

$$\frac{1}{a}\frac{\partial U_a(\mathrm{X},\mathrm{Y})}{\partial X}=\frac{1}{1-a}\frac{\partial U_c(\mathrm{X},\mathrm{Y})}{\partial X} \tag{4.3.16}$$

4.2.3.3 MOL and FVDM

4.2.3.3.1 For i=0

Equations 4.3.17 and 4.3.18 are obtained from boundary conditions of anode and cathode (Equation 4.3.12 and 4.3.13)

At $Y=0$ for $0\leq X\leq 1$ (Anode boundary condition),

$$\frac{\partial U_{a,0}(\mathrm{X})}{\partial Y}=J_a\varepsilon^2 U_{a,0}(\mathrm{X}) \tag{4.3.17}$$

At $Y=0$ for $0\leq X\leq 1$ (Cathode boundary),

$$\frac{\partial U_{c,0}(\mathrm{X})}{\partial Y}=J_c\varepsilon^2\left(U_{c,0}(\mathrm{X})-1\right) \tag{4.3.18}$$

4.2.3.3.2 For i=1

A quadratic profile approximation is implemented in both anode and cathode regions. Equations 4.3.19-4.3.22 are the approximation in an anode region. The coefficients of $e,b,and\,c$ are calculated by solving Equations 4.3.20-4.3.22.

$$U_a(X,Y)=e+bY+cY^2 \tag{4.3.19}$$

$$J_a\varepsilon^2 a=b \tag{4.3.20}$$

$$U_{a,1}(X,Y)=\frac{1}{4}ch_1^2+\frac{1}{2}bh_1+e \tag{4.3.21}$$

$$U_{a,2}(X,Y)=c\left(h_1+\frac{1}{2}h_2\right)^2+b\left(h_1+\frac{1}{2}h_2\right)+e \tag{4.3.22}$$

Equations 4.3.23- 4.3.25 are the approximation in a cathode region. By solving Equations 4.3.23-4.3.25, coefficients of $e,b,and\,c$ are identified.

$$J_c\varepsilon^2(a-1)=b \tag{4.3.23}$$

$$U_{c,1}(X,Y)=\frac{1}{4}ch_1^2+\frac{1}{2}bh_1+e \tag{4.3.24}$$

$$U_{c,2}(X,Y)=c\left(h_1+\frac{1}{2}h_2\right)^2+b\left(h_1+\frac{1}{2}h_2\right)+e \tag{4.3.25}$$

Inserting coefficients in anode and cathode regions into the second order Y-derivative,

$$\frac{d^2U_{a,1}(X,Y)}{dY^2}=-\frac{8\left(2J_a\varepsilon^2U_{a,1}(X)h_1+J_a\varepsilon^2U_{a,1}(X)h_2-J_a\varepsilon^2U_{a,2}(X)h_1+2U_{a,1}(X)-2U_{a,2}(X)\right)}{(2J_a\varepsilon^2h_1^3+3J_a\varepsilon^2h_1^2h_2+J_a\varepsilon^2h_2^2h_1+6h_1^2+8h_1h_2+2h_2^2)} \tag{4.3.26}$$

$$\frac{d^2U_{c,1}(X,Y)}{dY^2}=-\frac{8\left(2J_c\varepsilon^2U_{c,1}(X)h_1+J_c\varepsilon^2U_{c,1}(X)h_2-J_c\varepsilon^2U_{c,2}(X)h_1-J_c\varepsilon^2h_1-J_c\varepsilon^2h_2+2U_{c,1}(X)-2U_{c,2}(X)\right)}{(2J_c\varepsilon^2h_1^3+3J_c\varepsilon^2h_1^2h_2+J_c\varepsilon^2h_2^2h_1+6h_1^2+8h_1h_2+2h_2^2)} \tag{4.3.27}$$

4.2.3.3.3 For i from 2 to N-1

Y-derivatives are discretized according to the following set of equations:

$$\frac{\partial^2U_a(X,Y)}{\partial Y^2}=\frac{U_{a,i+1}(X)-U_{a,i}(X)}{h_i\left(\frac{h_{i+1}}{2}+\frac{h_i}{2}\right)}-\frac{U_{a,i}(X)-U_{a,i-1}(X)}{h_i\left(\frac{h_i}{2}+\frac{h_{i-1}}{2}\right)} \tag{4.3.28}$$

Substituting Equation 4.3.28 to 4.3.10 and 4.3.11,

$$\frac{\varepsilon^2}{a^2}\frac{d^2U_{a,i}(X)}{dX^2}+\frac{U_{a,i+1}(X)-U_{a,i}(X)}{h_i\left(\frac{h_{i+1}}{2}+\frac{h_i}{2}\right)}-\frac{U_{a,i}(X)-U_{a,i-1}(X)}{h_i\left(\frac{h_i}{2}+\frac{h_{i-1}}{2}\right)}=0 \tag{4.3.29}$$

$$\frac{\varepsilon^2}{(1-a)^2}\frac{d^2U_{c,i}(X)}{dX^2}+\frac{U_{c,i+1}(X)-U_{c,i}(X)}{h_i\left(\frac{h_{i+1}}{2}+\frac{h_i}{2}\right)}-\frac{U_{c,i}(X)-U_{c,i-1}(X)}{h_i\left(\frac{h_i}{2}+\frac{h_{i-1}}{2}\right)}=0 \tag{4.3.30}$$

4.2.3.3.4 i=N

To obtain the equations for *y*-derivatives at $i = N$, following equations are solved by using the BCs $\partial u/\partial y = 0$ and $\partial u1/\partial y = 0$ at $y = 1$ boundary (for both anode and cathode regions).

$$b+2c=0 \tag{4.3.31}$$

$$U_N(X,Y)=c\left(1-\frac{1}{2}h_N\right)^2+b\left(1-\frac{1}{2}h_N\right)+e \tag{4.3.32}$$

$$U_{N-1}(X,Y)=c\left(1-h_N-\frac{1}{2}h_{N-1}\right)^2+b\left(1-h_N-\frac{1}{2}h_{N-1}\right)+e \tag{4.3.33}$$

$$\frac{d^2U_N(X,Y)}{dY^2}=-\frac{8\left(U_N(X,Y)-U_{N-1}(X,Y)\right)}{(3h_N^2+4h_Nh_{N-1}+h_{N-1}^2)} \tag{4.3.34}$$

4.2.3.3.5 i=N+1

Equation 3.35 is obtained from insulating boundary conditions (Equation 3.15)

$$\frac{\partial U_{a,1}(\mathrm{X})}{\partial Y}=0 \text{ and } \frac{\partial U_{c,1}(\mathrm{X})}{\partial Y}=0 \tag{4.3.35}$$

4.2.3.4 Results

Dimensionless potential distribution in the thin-layer galvanic cell for ε = 1 x 10^{-3} and for J_a = 10 and J_c = 10 is compared with the solution obtained in COMSOL and is shown in Table 4.4. In case of discontinuous boundary conditions such as the one in thin layer galvanic cell, finite difference discretization methods do not handle the discontinuity well. The method presented in this paper takes care of the discontinuity as it solves for the discretized variables at the first node point, which lies above the boundary and which is continuous. This method could easily be used in the solvers to further increase their efficiency and robustness. The boundary condition of the anode at $Y=0$ is varied depending on approximations for modeling the current distribution on the electrodes of the cell.

Method	Number of Nodes		Number of DAE	CPU time (s)	RSME (V)	Software
FVM + constant node	N=3	Secondary Linear	3	0.109	0.01	Maple
	N=5		5	0.156	0.0039	
	N=10		10	0.203	0.001	
	N=20		20	0.515	0.0003	
FVM + variable	N=3	Secondary Linear	3	0.093	0.009	Maple
	N=5		5	0.140	0.003	
	N=10		10	0.203	0.0008	
	N=20		20	0.483	0.00026	
FEM	N/A	Secondary Linear	N/A	1.5	N/A	COMSOL
			N/A		N/A	
			N/A		N/A	

Table 4.4. Comparison of Computational Time in Coplanar thin-layer galvanic cell with constant node and variable node spacing

Chapter 5. FUTURE WORK

The proposed bottom-up approach is a good starting point, there are a few issues that still need to be addressed.

5.1 FLOW BATTERY

In the static cell system, the capacity fade/ loss was explicitly observed even for a single cycle. For this reason, the static cell setup is not a practical system, but this can be a good starting point for developing flow battery models, including related physics and transport. For example, the proposed static cell model includes both uni- and anti- directional migration effects leading to more accurate prediction compared to current zero-dimensional models adopting only uni-directional migration effects.

5.1.1 Single-cell and multiple-cell models

The physics-based models of VRFBs can be developed based on the proposed static cell models. The developed models can be validated step by step with experimental data from several kinds of chemistries for the single cell/ multiple cells of redox flow batteries. Voltage profiles of those chemistries can be matched with voltage outputs from models including different chemistries. For the multiple-cell validation, a small number of cells can be used initially, and this can be extended to a large stack in parallel and series.

5.2 BATTERY/GRID INTEGRATION

Once the VRFB models are developed and validated, the models can be integrated into the proposed battery/grid framework that enables to maximize the battery performance and usability. Different combinations of different chemistries/types of multiple-cell battery models (e.g., flow batteries + lithium ion batteries) can be implemented for renewable grid applications.

Also, most current approaches today utilize built-in block diagrams (e.g., MATLAB Simulink) and renewable grid structures are based on empirical electrochemical system models. However, the bottom-up approach is an equations-based approach and it might take time to change the trend of current renewable grid simulations. Also, the other grid components models are simplified other than the batteries in the proposed approach. The following studies can be conducted to solve these problems. A better integration method can be identified by sequentially replacing the empirical models of the current renewable grid frame. For example, empirical battery models can be replaced with physics-based battery models by adopting the current publicly available diagram-grid framework, which will require a structural modification of the grid system. When an electrochemical storage system is implemented in an improved renewable grid framework, the replacement of the energy generation system and power conversion model can follow. At each step, a renewable grid system with a physics-based models can be compared to the current approach in terms of accuracy, system utilization, and cost. Also, better integration methods can be identified if needed.

BIBLIOGRAPHY

[1] Doyle, M., Fuller, T. F., and Newman, J., 1993, "Modeling of galvanostatic charge and discharge of the lithium/polymer/insertion cell," Journal of the Electrochemical Society, 140(6), pp. 1526-1533.

[2] Beck, D. A., Carothers, J. M., Subramanian, V. R., and Pfaendtner, J., 2016, "Data science: Accelerating innovation and discovery in chemical engineering," AIChE Journal, 62(5), pp. 1402-1416.

[3] McDowall, J., 2008, "Understanding lithium-ion technology," Proceedings of Battcon.

[4] Dunn, B., Kamath, H., and Tarascon, J.-M., 2011, "Electrical energy storage for the grid: a battery of choices," Science, 334(6058), pp. 928-935.

[5] Beaudin, M., Zareipour, H., Schellenberglabe, A., and Rosehart, W., 2010, "Energy storage for mitigating the variability of renewable electricity sources: An updated review," Energy for Sustainable Development, 14(4), pp. 302-314.

[6] Divya, K., and Ostergaard, J., 2009, "Battery energy storage technology for power systems—An overview," Electric Power Systems Research, 79(4), pp. 511-520.

[7] Lacey, S., 2016, Greentech Media, USA, 2016.
Available: https://www.greentechmedia.com/articles/read/stem-cto-weve-seen-battery-prices-fall-70-in-the-last-18-months.

[8] Ivanova, N., "Lithium-ion costs to fall by up to 50% within five years ", Energy storage update, London, UK, 2015. Available: http://analysis.energystorageupdate.com/lithium-ion-costs-fall-50-within-five-years.

[9] Li, X., 2012, "Fuzzy adaptive Kalman filter for wind power output smoothing with battery energy storage system," IET Renewable Power Generation, 6(5), pp. 340-347.

[10] Li, X., Hui, D., and Lai, X., 2013, "Battery energy storage station (BESS)-based smoothing control of photovoltaic (PV) and wind power generation fluctuations," IEEE Transactions on Sustainable Energy, 4(2), pp. 464-473.

[11] Li, X., Li, Y., Han, X., and Hui, D., 2011, "Application of fuzzy wavelet transform to smooth wind/PV hybrid power system output with battery energy storage system," Energy Procedia, 12, pp. 994-1001.

[12] Naderi, P., 2013, "Distributed generation, using battery/photovoltaic system: modeling and simulation with relative controller design," Journal of Solar Energy Engineering, 135(2), p. 024506.

[13] Botte, G. G., Subramanian, V. R., and White, R. E., 2000, "Mathematical modeling of secondary lithium batteries," Electrochimica Acta, 45(15), pp. 2595-2609.

[14] Tamrakar, V., Gupta, S. C., and Sawle, Y., 2015, "Single-Diode PV Cell Modeling and Study of Characteristics of Single and Two-Diode Equivalent Circuit," Electrical and Electronics Engineering: An International Journal (ELELIJ), 4(3).

[15] Villalva, M. G., Gazoli, J. R., and Ruppert Filho, E., 2009, "Comprehensive approach to modeling and simulation of photovoltaic arrays," IEEE Transactions on Power Electronics, 24(5), pp. 1198-1208.

[16] Femia, N., Petrone, G., Spagnuolo, G., and Vitelli, M., 2005, "Optimization of perturb and observe maximum power point tracking method," IEEE transactions on Power Electronics, 20(4), pp. 963-973.

[17] Zakzouk, N., Abdelsalam, A., Helal, A., and Williams, B., "Modified variable-step incremental conductance maximum power point tracking technique for photovoltaic systems," Proc. Industrial Electronics Society, IECON 2013-39th Annual Conference of the IEEE, Vienna, Austria, IEEE, pp. 1741-1748.
[18] Femia, N., Granozio, D., Petrone, G., Spagnuolo, G., and Vitelli, M., 2007, "Predictive & adaptive MPPT perturb and observe method," IEEE Transactions on Aerospace and Electronic Systems, 43(3), pp. 934-950.
[19] Nedumgatt, J. J., Jayakrishnan, K., Umashankar, S., Vijayakumar, D., and Kothari, D., "Perturb and observe MPPT algorithm for solar PV systems-modeling and simulation," Proc. 2011 Annual IEEE India Conference, IEEE, pp. 1-6.
[20] Piegari, L., and Rizzo, R., 2010, "Adaptive perturb and observe algorithm for photovoltaic maximum power point tracking," IET Renewable Power Generation, 4(4), pp. 317-328.
[21] Sera, D., Mathe, L., Kerekes, T., Spataru, S. V., and Teodorescu, R., 2013, "On the perturb-and-observe and incremental conductance MPPT methods for PV systems," IEEE journal of photovoltaics, 3(3), pp. 1070-1078.
[22] Tan, C. W., Green, T. C., and Hernandez-Aramburo, C. A., "Analysis of perturb and observe maximum power point tracking algorithm for photovoltaic applications," Proc. Power and Energy Conference, 2008. PECon 2008. IEEE 2nd International, Johor Bahru, Malaysia, IEEE, pp. 237-242.
[23] Salas, V., Olias, E., Barrado, A., and Lazaro, A., 2006, "Review of the maximum power point tracking algorithms for stand-alone photovoltaic systems," Solar energy materials and solar cells, 90(11), pp. 1555-1578.
[24] Methekar, R. N., Ramadesigan, V., Pirkle, J. C., and Subramanian, V. R., 2011, "A perturbation approach for consistent initialization of index-1 explicit differential–algebraic equations arising from battery model simulations," Computers & Chemical Engineering, 35(11), pp. 2227-2234.
[25] Tao, H., Kotsopoulos, A., Duarte, J. L., and Hendrix, M. A., 2006, "Family of multiport bidirectional DC-DC converters," IEE Proceedings-Electric Power Applications, 153(3), pp. 451-458.
[26] Islam, M. R., Guo, Y., and Zhu, J., 2014, "Power Converters for Small-to Large-Scale Photovoltaic Power Plants," Power Converters for Medium Voltage Networks, Springer, pp. 17-49.
[27] Northrop, P. W., Ramadesigan, V., De, S., and Subramanian, V. R., 2011, "Coordinate transformation, orthogonal collocation, model reformulation and simulation of electrochemical-thermal behavior of lithium-ion battery stacks," Journal of The Electrochemical Society, 158(12), pp. A1461-A1477.
[28] Lawder, M. T., Ramadesigan, V., Suthar, B., and Subramanian, V. R., 2015, "Extending explicit and linearly implicit ODE solvers for index-1 DAEs," Computers & Chemical Engineering, 82, pp. 283-292.
[29] Chim, C. S., Neelakantan, P., Yoong, H. P., and Teo, K. T. K., "Fuzzy logic based MPPT for photovoltaic modules influenced by solar irradiation and cell temperature," Proc. 2011 UkSim 13th International Conference on Computer Modelling and Simulation, Cambridge, UK, IEEE, pp. 376-381.
[30] Rawat, R., and Chandel, S., 2013, "Hill climbing techniques for tracking maximum power point in solar photovoltaic systems-a review," Int. J. Sustain. Dev. Green Econ.(IJSDGE), 2, pp. 90-95.

[31] Subudhi, B., and Pradhan, R., 2013, "A comparative study on maximum power point tracking techniques for photovoltaic power systems," IEEE Transactions on Sustainable Energy, 4(1), pp. 89-98.

[32] Shampine, L. F., Reichelt, M. W., and Kierzenka, J. A., 1999, "Solving index-1 DAEs in MATLAB and Simulink," SIAM review, 41(3), pp. 538-552.

[33] Santhanagopalan, S., Guo, Q., Ramadass, P., and White, R. E., 2006, "Review of models for predicting the cycling performance of lithium ion batteries," Journal of Power Sources, 156(2), pp. 620-628.

[34] Lawder, M. T., Suthar, B., Northrop, P. W., De, S., Hoff, C. M., Leitermann, O., Crow, M. L., Santhanagopalan, S., and Subramanian, V. R., 2014, "Battery Energy Storage System (BESS) and Battery Management System (BMS) for Grid-Scale Applications," Proceedings of the IEEE, 102(6), pp. 1014-1030.

[35] Pinson, M. B., and Bazant, M. Z., 2013, "Theory of SEI formation in rechargeable batteries: capacity fade, accelerated aging and lifetime prediction," Journal of the Electrochemical Society, 160(2), pp. A243-A250.

[36] Ramadass, P., Haran, B., Gomadam, P. M., White, R., and Popov, B. N., 2004, "Development of first principles capacity fade model for Li-ion cells," Journal of the Electrochemical Society, 151(2), pp. A196-A203.

[37] 2015, Network Optimized Distributed Energy Systems (NODES), U.S Department of Energy (DOE), Available: https://arpa-e.energy.gov/?q=arpa-e-programs/nodes.

[38] 2017, Enabling Extream Real-Time Grid Intergration of Solar Energy (ENERGISE), Department of Energy (DOE), Available: https://energy.gov/eere/sunshot/enabling-extreme-real-time-grid-integration-solar-energy-energise.

[39] Brandl, M., Gall, H., Wenger, M., Lorentz, V., Giegerich, M., Baronti, F., Fantechi, G., Fanucci, L., Roncella, R., and Saletti, R., "Batteries and battery management systems for electric vehicles," Proc. Design, Automation & Test in Europe Conference & Exhibition (DATE), Dresden, Germany, 2012, IEEE, pp. 971-976.

[40] Coley, G., 2013, Beaglebone black system reference manual, Texas Instruments, Dallas. Available: http://elinux.org/Beagleboard:BeagleBoneBlack.

[41] Hindmarsh, A. C., Serban, R., and Collier, A., 2006, User Documentation for ida v2. 6.0, Center for Applied Scientific Computing Lawrence Livermore National Laboratory.

[42] Cho, K. T., Ridgway, P., Weber, A. Z., Haussener, S., Battaglia, V., and Srinivasan, V., 2012, "High performance hydrogen/bromine redox flow battery for grid-scale energy storage," Journal of The Electrochemical Society, 159(11), pp. A1806-A1815.

[43] Shah, A., Tangirala, R., Singh, R., Wills, R., and Walsh, F., 2011, "A dynamic unit cell model for the all-vanadium flow battery," Journal of the Electrochemical society, 158(6), pp. A671-A677.

[44] Boettcher, P. A., Agar, E., Dennison, C., and Kumbur, E. C., 2016, "Modeling of ion crossover in vanadium redox flow batteries: A computationally-efficient lumped parameter approach for extended cycling," Journal of The Electrochemical Society, 163(1), pp. A5244-A5252.

[45] Pugach, M., Kondratenko, M., Briola, S., and Bischi, A., 2018, "Zero dimensional dynamic model of vanadium redox flow battery cell incorporating all modes of vanadium ions crossover," Applied Energy, 226, pp. 560-569.

[46] Knehr, K., Agar, E., Dennison, C., Kalidindi, A., and Kumbur, E., 2012, "A transient vanadium flow battery model incorporating vanadium crossover and water transport through the membrane," Journal of The Electrochemical Society, 159(9), pp. A1446-A1459.

[47] Shah, A., Al-Fetlawi, H., and Walsh, F., 2010, "Dynamic modelling of hydrogen evolution effects in the all-vanadium redox flow battery," Electrochimica Acta, 55(3), pp. 1125-1139.
[48] Al-Fetlawi, H., Shah, A., and Walsh, F., 2010, "Modelling the effects of oxygen evolution in the all-vanadium redox flow battery," Electrochimica Acta, 55(9), pp. 3192-3205.
[49] Tang, A., Bao, J., and Skyllas-Kazacos, M., 2011, "Dynamic modelling of the effects of ion diffusion and side reactions on the capacity loss for vanadium redox flow battery," Journal of Power Sources, 196(24), pp. 10737-10747.
[50] Darling, R. M., Weber, A. Z., Tucker, M. C., and Perry, M. L., 2016, "The influence of electric field on crossover in redox-flow batteries," Journal of The Electrochemical Society, 163(1), pp. A5014-A5022.
[51] Lei, Y., Zhang, B., Bai, B., and Zhao, T. S., 2015, "A transient electrochemical model incorporating the Donnan effect for all-vanadium redox flow batteries," Journal of Power Sources, 299, pp. 202-211.
[52] Gandomi, Y. A., Zawodzinski, T. A., and Mench, M. M., 2014, "Concentrated solution model of transport in all vanadium redox flow battery membrane separator," ECS Transactions, 61(13), pp. 23-32.
[53] Pratt, H. D., Hudak, N. S., Fang, X., and Anderson, T. M., 2013, "A polyoxometalate flow battery," Journal of Power Sources, 236, pp. 259-264.
[54] Wiedemann, E., Heintz, A., and Lichtenthaler, R., 1998, "Transport properties of vanadium ions in cation exchange membranes:: Determination of diffusion coefficients using a dialysis cell," Journal of membrane science, 141(2), pp. 215-221.
[55] Sun, C., Chen, J., Zhang, H., Han, X., and Luo, Q., 2010, "Investigations on transfer of water and vanadium ions across Nafion membrane in an operating vanadium redox flow battery," Journal of Power Sources, 195(3), pp. 890-897.
[56] Li, J., Wang, L., Lyu, C., Wang, H., and Liu, X., 2016, "New method for parameter estimation of an electrochemical-thermal coupling model for LiCoO 2 battery," Journal of Power Sources, 307, pp. 220-230.
[57] Skyllas-Kazacos, M., and Goh, L., 2012, "Modeling of vanadium ion diffusion across the ion exchange membrane in the vanadium redox battery," Journal of membrane science, 399, pp. 43-48.
[58] Aaron, D., Sun, C.-N., Bright, M., Papandrew, A. B., Mench, M. M., and Zawodzinski, T. A., 2013, "In situ kinetics studies in all-vanadium redox flow batteries," ECS Electrochemistry Letters, 2(3), pp. A29-A31.
[59] Miller, M., Bourke, A., Quill, N., Wainright, J., Lynch, R., Buckley, D., and Savinell, R., 2016, "Kinetic study of electrochemical treatment of carbon fiber microelectrodes leading to in situ enhancement of vanadium flow battery efficiency," Journal of The Electrochemical Society, 163(9), pp. A2095-A2102.
[60] Shi, S., Weber, A. Z., and Kusoglu, A., 2016, "Structure/property relationship of Nafion XL composite membranes," Journal of Membrane Science, 516, pp. 123-134.
[61] Motupally, S., Becker, A. J., and Weidner, J. W., 2000, "Diffusion of water in Nafion 115 membranes," Journal of The Electrochemical Society, 147(9), pp. 3171-3177.
[62] Weber, A. Z., Mench, M. M., Meyers, J. P., Ross, P. N., Gostick, J. T., and Liu, Q., 2011, "Redox flow batteries: a review," Journal of Applied Electrochemistry, 41(10), pp. 1137-1164.
[63] Ramadesigan, V., Chen, K., Burns, N. A., Boovaragavan, V., Braatz, R. D., and Subramanian, V. R., 2011, "Parameter estimation and capacity fade analysis of lithium-ion batteries using reformulated models," Journal of The Electrochemical Society, 158(9), pp. A1048-A1054.

[64] Santhanagopalan, S., Guo, Q., and White, R. E., 2007, "Parameter estimation and model discrimination for a lithium-ion cell," Journal of the Electrochemical Society, 154(3), pp. A198-A206.

[65] Brelje, B. J., and Martins, J. R., "Development of a Conceptual Design Model for Aircraft Electric Propulsion with Efficient Gradients," Proc. 2018 AIAA/IEEE Electric Aircraft Technologies Symposium, p. 4979.

[66] Pintér, J. D., Linder, D., and Chin, P., 2006, "Global Optimization Toolbox for Maple: An introduction with illustrative applications," Optimisation Methods and Software, 21(4), pp. 565-582.

[67] Levenspiel, O., 1999, "Chemical reaction engineering," Industrial & engineering chemistry research, 38(11), pp. 4140-4143.

[68] Yang, X.-G., Ye, Q., Cheng, P., and Zhao, T. S., 2015, "Effects of the electric field on ion crossover in vanadium redox flow batteries," Applied Energy, 145, pp. 306-319.

[69] Lei, Y., Zhang, B., Zhang, Z. H., Bai, B. F., and Zhao, T., 2018, "An improved model of ion selective adsorption in membrane and its application in vanadium redox flow batteries," Applied Energy, 215, pp. 591-601.

[70] Verma, P., Maire, P., and Novák, P., 2010, "A review of the features and analyses of the solid electrolyte interphase in Li-ion batteries," Electrochimica Acta, 55(22), pp. 6332-6341.

[71] Lee, S. B., Pratt, H. D., Anderson, T. M., Mitra, K., Chalamala, B. R., and Subramanian, V. R., 2018, "Estimation of Transport and Kinetic Parameters of Vanadium Redox Batteries Using Static Cells," ECS Transactions, 85(5), pp. 43-64.

[72] Li, J., Zou, L., Tian, F., Dong, X., Zou, Z., and Yang, H., 2016, "Parameter identification of lithium-ion batteries model to predict discharge behaviors using heuristic algorithm," Journal of The Electrochemical Society, 163(8), pp. A1646-A1652.

[73] Jokar, A., Rajabloo, B., Désilets, M., and Lacroix, M., 2016, "An Inverse Method for Estimating the Electrochemical Parameters of Lithium-Ion Batteries I. Methodology," Journal of The Electrochemical Society, 163(14), pp. A2876-A2886.

[74] Wei, Z., Tseng, K. J., Wai, N., Lim, T. M., and Skyllas-Kazacos, M., 2016, "Adaptive estimation of state of charge and capacity with online identified battery model for vanadium redox flow battery," Journal of Power Sources, 332, pp. 389-398.

[75] Wei, Z., Lim, T. M., Skyllas-Kazacos, M., Wai, N., and Tseng, K. J., 2016, "Online state of charge and model parameter co-estimation based on a novel multi-timescale estimator for vanadium redox flow battery," Applied Energy, 172, pp. 169-179.

[76] Fares, R. L., Meyers, J. P., and Webber, M. E., 2014, "A dynamic model-based estimate of the value of a vanadium redox flow battery for frequency regulation in Texas," Applied Energy, 113, pp. 189-198.

[77] Petzold, L. R., 1989, "Recent developments in the numerical solution of differential/algebraic systems," Computer Methods in Applied Mechanics and Engineering, 75(1-3), pp. 77-89.

[78] Kraft, D., 1988, "A software package for sequential quadratic programming," Forschungsbericht- Deutsche Forschungs- und Versuchsanstalt fur Luft- und Raumfahrt.

[79] Wendorff, A., Botero, E., and Alonso, J. J., "Comparing Different Off-the-Shelf Optimizers' Performance in Conceptual Aircraft Design," Proc. 17th AIAA/ISSMO Multidisciplinary Analysis and Optimization Conference, p. 3362.

[80] Bock, D. C., Marschilok, A. C., Takeuchi, K. J., and Takeuchi, E. S., 2012, "Batteries used to power implantable biomedical devices," Electrochimica acta, 84, pp. 155-164.

[81] Walczak, K., Chen, Y., Karp, C., Beeman, J. W., Shaner, M., Spurgeon, J., Sharp, I. D., Amashukeli, X., West, W., and Jin, J., 2015, "Modeling, Simulation, and Fabrication of a Fully Integrated, Acid-stable, Scalable Solar-Driven Water-Splitting System," ChemSusChem, 8(3), pp. 544-551.
[82] Subramanian, V. R., and White, R. E., 2000, "A semianalytical method for predicting primary and secondary current density distributions: Linear and nonlinear boundary conditions," Journal of the Electrochemical Society, 147(5), pp. 1636-1644.
[83] Matlosz, M., Creton, C., Clerc, C., and Landolt, D., 1987, "Secondary Current Distribution in a Hull Cell Boundary Element and Finite Element Simulation and Experimental Verification," Journal of the Electrochemical Society, 134(12), pp. 3015-3021.
[84] Morris, R., and Smyrl, W., 1989, "Current and potential distribution in thin electrolyte layer galvanic cells," Journal of The Electrochemical Society, 136(11), pp. 3229-3236.
[85] Nakai, K., Nakano, T., and Hironaka, K., 2003, "Cylindrical lithium-ion battery," Google Patents.
[86] Young, K., Wang, C., Wang, L. Y., and Strunz, K., 2013, "Electric vehicle battery technologies," Electric vehicle integration into modern power networks, Springer, pp. 15-56.
[87] Motors, T., 2014, "Panasonic and Tesla Sign Agreement for the Gigafactory, Available: http://www.chemwinfo.com/private_folder/Uploadfile2014July/Panasonic_and_Tesla_Sign_Agreement_.pdf," Tesla blog.
[88] Errico, V., De Ninno, A., Bertani, F. R., Businaro, L., Bisegna, P., and Caselli, F., 2017, "Mitigating positional dependence in coplanar electrode Coulter-type microfluidic devices," Sensors and Actuators B: Chemical, 247, pp. 580-586.
[89] Popov, K., Grgur, B., and Djokić, S. S., 2007, Fundamental aspects of electrometallurgy, Springer.
[90] Lee, S. B., Kolluri, S., Xu, W., Zhang, J.-G., and Subramanian, V. R., "Electrochemical Modeling, Optimization and Control of Lithium Metal Batteries," Proc. Meeting Abstracts, The Electrochemical Society, pp. 149-149.
[91] Chen, J., Subramaniam, A., Lee, S. B., Geise, N. R., Kasse, R. M., Toney, M. F., and Subramanian, V. R., "Modeling Lithium Growth in Symmetric Cells," Proc. Meeting Abstracts, The Electrochemical Society, pp. 1348-1348.
[92] Wiley, J. D., and Webster, J. G., 1982, "Analysis and control of the current distribution under circular dispersive electrodes," IEEE Transactions on Biomedical Engineering(5), pp. 381-385.
[93] Landau, U., 2009, "Current Distribution in Electrochemical Cells: Analytical and Numerical Modeling," Modern Aspects of Electrochemistry No. 44, Springer, pp. 451-501.
[94] Low, C., Roberts, E., and Walsh, F., 2007, "Numerical simulation of the current, potential and concentration distributions along the cathode of a rotating cylinder Hull cell," Electrochimica Acta, 52(11), pp. 3831-3840.
[95] Teeratananon, M., Pruksathorn, K., Damronglerd, S., Dupuy, F., Vergnes, H., Fenouilletc, B., and Duverneuilc, P., 2004, "Experimental investigation of the current distribution in Mohler cell and Rotating Cylinder Hull cell," Electrochimica Acta, 30, pp. 375-381.
[96] Chmielowiec, B., Cai, T., and Allanore, A., 2016, "Simultaneous Spatial and Temporal Measurements of the Current Distribution in a Miniature Hull Cell," Journal of The Electrochemical Society, 163(5), pp. E142-E146.
[97] Zhang, Z., Zhang, J., Leng, W., and Cao, C., 2001, "Investigation of the secondary current distribution in a hull cell," Journal of the Electrochemical Society, 148(7), pp. C488-C491.

[98] Tang, H., and Gao, Y., 2005, "An impedance microsensor with coplanar electrodes and vertical sensing apertures," IEEE sensors journal, 5(6), pp. 1346-1352.
[99] Lee, S. S., Kim, T. H., Hu, S. J., Cai, W. W., and Abell, J. A., "Joining technologies for automotive lithium-ion battery manufacturing: A review," Proc. ASME 2010 international manufacturing science and engineering conference, American Society of Mechanical Engineers, pp. 541-549.
[100] Newman, J., and Thomas-Alyea, K. E., 2012, Electrochemical systems, John Wiley & Sons.
[101] Zheng, J., Yan, P., Mei, D., Engelhard, M. H., Cartmell, S. S., Polzin, B. J., Wang, C., Zhang, J. G., and Xu, W., 2016, "Highly Stable Operation of Lithium Metal Batteries Enabled by the Formation of a Transient High-Concentration Electrolyte Layer," Advanced Energy Materials, 6(8).
[102] Li, Z., Huang, J., Liaw, B. Y., Metzler, V., and Zhang, J., 2014, "A review of lithium deposition in lithium-ion and lithium metal secondary batteries," Journal of power sources, 254, pp. 168-182.
[103] Lee, S. B., Pathak, C., Ramadesigan, V., Gao, W., and Subramanian, V. R., 2017, "Direct, efficient, and real-time simulation of physics-based battery models for stand-alone pv-battery microgrids," Journal of The Electrochemical Society, 164(11), pp. E3026-E3034.
[104] Carnahan, B., and Luther, H., 1969, "J. 0. Wilkes," Applied Numerical Methods, p. 421.
[105] Schiesser, W., 1991, "The numerical methods of lines," Integration of partial differential equations Academic Press San Diego.
[106] Schiesser, W. E., 2014, Computational mathematics in engineering and applied science: ODEs, DAEs, and PDEs, CRC press.
[107] Schiesser, W., 1994, "Method of lines solution of the Korteweg-de Vries equation," Computers & Mathematics with Applications, 28(10-12), pp. 147-154.
[108] Mallinson, G. D., and de Vahl Davis, G., 1973, "The method of the false transient for the solution of coupled elliptic equations," Journal of Computational Physics, 12(4), pp. 435-461.
[109] Schiesser, W. E., and Silebi, C. A., 1997, Computational transport phenomena: numerical methods for the solution of transport problems, Cambridge University Press.
[110] Cutlip, M. B., and Shacham, M., 1998, "The numerical method of lines for partial differential equations," CACHE News, 47, pp. 18-21.
[111] Constantinides, A., and Mostoufi, N., 1999, Numerical methods for chemical engineers with MATLAB applications, Prentice Hall PTR Upper Saddle River, NJ.
[112] Taylor, R., 1999, "Engineering computing with maple: solution of PDEs via method of lines," CACHE News, 49, pp. 5-8.
[113] Jones, D., South Jr, J., and Klunker, E., 1972, "On the numerical solution of elliptic partial differential equations by the method of lines," Journal of Computational Physics, 9(3), pp. 496-527.
[114] Versteeg, H. K., and Malalasekera, W., 2007, An introduction to computational fluid dynamics: the finite volume method, Pearson education.

APPENDIX A

Note 1. Source codes, executable files, and text files

There are two sets of source codes, executable files, and text files for the Nafion® 115 and the Nafion® XL systems. They are prepared to run on any Windows based PC environment. Each set contains source codes, an executable file, and five text files. All relevant files can be downloaded directly from the Subramanian group's website as a zip file (http://depts.washington.edu/maple/VRBC.html). Once the zip files are downloaded, unzip all the files into the same folder. Below is the detailed instruction.

The Nafion® 115 system. The executable file ('Estimation_Nafion® 115 system.exe') in the zip file can estimate five parameters of the Nafion® 115 system: rate constants at anode and cathode, the cell resistance excluding the membrane resistance, the diffusion coefficient of protons, and the formal potential. The executable file uses one set of CC-CV charging and one set of CC discharging profiles and text files for specifying the experimental and model conditions.

1. Experimental conditions*:* While specifying the experimental conditions, information such as (i) the value of applied current, (ii) the regular time interval for a profile, and (iii) the number of voltage data used for parameter estimation exercise etc. are required. Users can enter their own experimental conditions to the text file called "Experimental conditions.txt". For the parameter estimation exercise carried out here, the following information has been entered. The first row is provided to enter values of applied currents for CC-charging and CC discharging for Nafion® 115 system at one C-rate. The provide text file contains values such as 0.000893 (C/30) for the first row. The second and third rows represent time intervals of CC-charging and CC-discharging at C/30 rate. In the uploaded text file, these time intervals were set as 513.6658291 and 362.4611558 seconds

for the C/30 operation. In the last row, users need to enter the number of the experimental data used for parameter estimation exercise. In this case, this number has been entered as 200.

2. Voltage data: Provide experimental voltage data at your C-rate (e.g., C/30) in the file called "Voltage data.txt". Note that the same number of experimental data was prepared for charging and discharging profiles. The first row represents the number of experimental data. The second and third columns present voltage data for charging and discharging at C/30, respectively. Users can input their experimental data sequentially.
3. Bounds: Provide bounds for estimating parameters in the "Bounds.txt" file. The first row represents the total number of bounds. After that, the lower and upper bounds for each of the five estimating parameters are given in this file as an 5 rows by 2 columns array. The parameter bounds are given in the following sequence: rate constants at anode and cathode, the formal potential, the diffusion coefficient of protons, and the cell resistance excluding the membrane resistance.
4. Initial guess: Provide initial guesses for estimating parameters in the "Guess.txt" file. Five estimating parameters are given in this file as a 5 rows by 1 column array. The initial guesses are given in the following sequence: rate constants at anode and cathode, the formal potential, the diffusion coefficient of protons, and the cell resistance excluding the membrane resistance. This sequence is same as the above sequence for providing the bounds for the parameters.
5. Model condition: Provide mathematical conditions such as the number of Ordinary Differential Equations (ODEs) and Algebraic Equations (AE) and tolerance in the text file

called “daskrinput.txt”. The number of ODE, the number of AE, a relative tolerance, and absolute tolerance are presented sequentially.

6. Double click and run the execution file “Estimation_Nafion® 115 system.exe”. Upon clicking, a command line window will be opened, and the program will calculate the optimal values of parameters. Once finishing the calculation, the command window will be closed. No action required.
7. The optimization results for all the variables can be found in the “Estimated parameters.csv”. The results will be given by the following sequence: rate constants at anode and cathode, the formal potential, the diffusion coefficient of protons, and the cell resistance excluding the membrane.

The Nafion® XL system. The second program (“Other membrane system.exe”) can estimate diffusion coefficients of four vanadium ions and protons for other membranes. The protocol to execute the executable file is similar to the previous step.

1. Identify your experimental conditions. Users can enter their own experimental conditions in the “Experimental conditions.txt” file. In the uploaded text file, the first row represents a value of applied currents for CC-charging for the Nafion® XL system at C/30. The second and third rows represent time intervals of CC-charging and CC-discharging. Here, the time interval was entered as 446.7550251 and 105.1483133 seconds for charging and discharging at C/30. In the fourth row, users need to enter the number of the experimental data. In the original file, the number of 200 experimental voltage data was used. From the fifth to the seventh rows, the information obtained in the Nafion® 115 system was used i.e. the fifth and sixth rows represent rate constants at anode and cathode, the seventh row represents the cell resistance, and the formal potential.

2. Bounds for estimating parameters are entered in the “Bounds.txt” file. The total number of bounds is given in the first row. After that, the bounds are given as a 5 rows by 2 columns array, i.e. the lower and upper bounds are given for the estimating parameters in the following sequence: diffusion coefficients of V^{2+}, V^{3+}, VO^{2+}, and VO_2^+, and protons.
3. Voltage data: Provide experimental voltage data at one C-rate in the file called “Voltage data.txt”. Note that the same number of experimental data was prepared for charging and discharging profiles. The total number of experimental data is given in the first row. After that, the first and second columns present voltage data for charging and discharging at C/30, respectively. Users can input their experimental data sequentially.
4. Initial guess and model conditions: Provide initial guesses for estimating parameters into the “Guess.txt” file. Five estimating parameters are given in this file as a 5 rows by 1 column array. The initial guesses are given in the following sequence: diffusion coefficients of V^{2+}, V^{3+}, VO^{2+}, and VO_2^+, and protons. Also, provide mathematical conditions including the number of ODE and AE and tolerance. The text file called “daskrinput.txt” includes the number of ODE, the number of AE, a relative tolerance, and absolute tolerance sequentially.
5. Double click and run the execuable file “Other membrane systems.exe”. Upon clicking, a command line window is opened, and the program will calculate the optimal values of the parameters. Once finishing the calculation, the command window will be closed. No action required.
6. The optimization results for all the parameters can be found in the “Estimated parameters.csv”. The results will be given by the following sequence: diffusion coefficients of V^{2+}, V^{3+}, VO^{2+}, and VO_2^+, and protons.

Note 2. Experimental data for batch cell and flow battery systems.

Experimental data for batch cell and flow battery systems under different operating conditions are hosted on the Sandia National Laboratory website (https://www.sandia.gov/ess-ssl/data-repository/). Table 1A describes specific information for each experimental data set.

Table 1A. Experimental Data for Flow Battery and Batch Cell Systems

	Operating condition	**Electrolyte**	**Electrode**	**Separator**	**Flow rate**	**Flow Field**
(Experimental data for flow battery systems)						
Experimental Data set 1	CC-charging/ discharging (0.5A)	1.7M $VOSO_4$, 3.3M H_2SO_4	Carbon felt	Nafion® 115	5 ml/min	10cm^2, Serpentine
Experimental Data set 2	CC-charging/ discharging (0.25A)	1.7M $VOSO_4$, 3.3M H_2SO_4	Carbon felt	Nafion® XL	5 ml/min	10cm^2, Serpentine
(Experimental data for batch cell systems)						
Experimental Data set 3	CC-CV charging/ discharging (C/10, C/20, C/30)	0.1M $VOSO_4$, 4M H_2SO_4	Graphite	Nafion® 115	N/A	H-cell
Experimental Data set 4	CC-charging/ discharging (C/20, C/30)	0.1M $VOSO_4$, 4M H_2SO_4	Graphite	Nafion® XL	N/A	H-cell

VITA

Seongbeom Lee is currently a Ph.D. candidate in the department of Chemical Engineering at the University of Washington, Seattle. After joining the Dr. Subramanian group in 2014, he has been working on modeling and simulations of electrochemical battery systems, including both conventional (e.g., lithium-ion battery) and next-generation energy storage systems (e.g., lithium-metal battery) and integrating them into renewable grid systems. Also, he has been working on modeling and simulation of large-scale batteries such as vanadium redox flow batteries which have gained paramount research interests in the renewable grid applications. Seongbeom received a B.E. in Chemical end Biomolecular Engineering, a B.S. in Economics as a double major, and a Master's in Chemistry from Sogang University, Seoul, South Korea.

Seongbeom have authored 6 peer-reviewed publications with several more in revision, awaiting review, or in preparation. Seongbeom ultimately wants to help increase the penetration of renewable grids by performing bottom-up modeling simulation and control of the same. Therefore, his current research centers on the development of computational physics-based model frameworks for renewable grid applications. One of the related publications was among the top 10 most-read articles in the Journal of the Electrochemical Society in March 2017. Seongbeom is a recipient of travel grants from the Electrochemical Society. He has been trained in writing several funded proposals for research topics related to physics-based battery models (JCATI, Battery 500 Consortium, and DOE Energy Storage Systems Program) and extensive collaboration experiences with other research groups (SNL, BNL, and UW-Madison).